

STAR FORMATION AND AGING
AT COSMIC NOON:
the spectral evolution of galaxies from $z=2$

STAR FORMATION AND AGING
AT COSMIC NOON:
the spectral evolution of galaxies
from $z = 2$

Proefschrift

ter verkrijging van
de graad van Doctor aan de Universiteit Leiden,
op gezag van Rector Magnificus prof.mr. C.J.J.M. Stolker,
volgens besluit van het College voor Promoties
te verdedigen op dinsdag 8 september 2015
klokke 10:00 uur

door

Mattia Fumagalli

geboren te Lecco, Italië
in 1986

Promotiecommissie

Promotores: Prof. dr. M. Franx
Prof. dr. P. G. van Dokkum Yale University

Overige leden: Prof. dr. H. J. A. Röttgering
Prof. dr. K. H. Kuijken
Prof. dr. J. Schaye
Prof. dr. M. Kriek University of California at Berkeley
dr. K. I. Caputi Rijksuniversiteit Groningen
dr. I. Labbé

Cover: 3D-HST stacks of spectra of star-forming galaxies pictured as mountain ranges. Peaks fade to the horizon as redshift increases.

Designed by Mattia Fumagalli and Marco Vedoá

To Anna

*Two roads diverged in a wood, and I
I took the one less traveled by
(Robert Frost)*

CONTENTS

1	Introduction	1
1.1	The Birth of Extragalactic Astronomy	1
1.2	The Striking Diversity of Galaxies	1
1.3	Measuring Star Formation through cosmic time	3
1.4	Issues at high redshifts	6
1.5	This Thesis	7
2	Hα Equivalent Widths from the 3D-HST survey	13
2.1	Introduction	14
2.2	Data	15
2.2.1	3D-HST	15
2.2.2	SDSS	15
2.2.3	VVDS	16
2.2.4	High redshift data	16
2.3	The EW(H α) - mass relation	16
2.4	The Evolution of EW(H α) with redshift	18
2.5	The sSFR(H α) - mass relation and its evolution with redshift	18
2.6	Linking the characteristic SFH of galaxies and EW(H α)	21
2.7	Conclusions	22
3	How dead are dead galaxies?	25
3.1	Introduction	26
3.2	Data	26
3.3	Sample selection and motivations of the study	29
3.3.1	Selection of Quiescent Galaxies	29
3.3.2	Spectra and SEDs of the sample	30
3.3.3	SFRs from SED fitting and expectations from gas recycling	31
3.3.4	How much star formation could be hidden?	31
3.4	Measuring Obscured Star-Formation Rates of Quiescent Galaxies	33
3.5	Other possible contributions to L_{IR}	36
3.5.1	AGN	36
3.5.2	Circumstellar dust	36
3.5.3	Cirrus dust	38
3.6	Discussion	38
3.7	Conclusions	40
3.A	Appendix A: Photometry	43
3.B	Appendix B: Field-to-field variation	43

4	Stacked spectra	49
4.1	Introduction	50
4.2	Data	51
4.2.1	The 3D-HST survey	51
4.2.2	Sample Selection	53
4.3	Methods	55
4.3.1	Stacking	55
4.3.2	Model fitting	56
4.4	Quiescent Galaxies	57
4.4.1	Quality of fits	57
4.4.2	Determination of Ages	59
4.5	Star Forming Galaxies	60
4.5.1	Quality of fits	60
4.5.2	Determination of Ages	62
4.6	Discussion	63
4.6.1	Differences among SPSs	63
4.6.2	Evolution of Ages	63
4.6.3	H α in quiescent galaxies	67
4.7	Conclusions	68
5	Decreasing Hα for redder star-forming galaxies: influence of dust and star formation rates	71
5.1	Introduction	72
5.2	Data and Sample Selection	73
5.2.1	The 3D-HST survey	73
5.2.2	Sample selection and the UVJ diagram	74
5.3	EW(H α): trend with color	75
5.3.1	Separating star-forming and quiescent galaxies with the UVJ selection	75
5.3.2	Color dependence of EW(H α) for star-forming galaxies	77
5.4	Specific Star Formation Rates of star-forming galaxies: trend with color	77
5.5	Dust absorption of star-forming galaxies along the UVJ diagram	80
5.5.1	Absorption in H α	80
5.5.2	Absorption of the continuum	83
5.6	Conclusions	87
	Samenvatting	91
	Publications	97
	Curriculum Vitae	103
	Acknowledgments	105

INTRODUCTION

1.1 The Birth of Extragalactic Astronomy

At the beginning of the XX century, our perception of the size and the structure of the Universe dramatically changed. If we had to set a symbolic date for that paradigm shift, we should go back to April the 26th, 1920.

On that day, two influential astronomers of the time, Harlow Shapley and Heber Curtis, debated the nature of spiral galaxies and the size of the Universe in front of a crowded auditorium at the Smithsonian Museum of Natural History, in Washington DC. Shapley argued in favor of the Milky Way, the faint stripe of stars visible in the sky during a dark clear night, as the entirety of the Universe. He believed that spiral nebulae, such as the ones classified by Messier and Herschel in the XVIII century, were part of our own galaxy. Curtis instead thought that Andromeda and the other nebulae were separate galaxies, or *island universes* (as Immanuel Kant had defined them one hundred years before).

Both scholars were backing their claims with different observations available at the time. However, the main support for Shapley's theory, i.e. the observation of the rotation of the Pinwheel Galaxy (which would have implied a distance smaller than the radius of the Milky Way disk) by Adriaan van Maanen, was soon shown to be incorrect. Observations by Edwin Hubble in the next years finally settled the debate. In 1922 Edwin Hubble measured the periods of Cepheids (a type of variable stars) in the outskirts of the Andromeda Nebula. Thanks to the work of Henrietta Swan Leavitt (1912), Cepheid stars were known to have a tight relation between their luminosity and the period of their variability. Hubble's observations showed incontrovertibly that Andromeda was in fact a separate island Universe, far outside the Milky Way.

It was again Hubble, a few years later (1927), who found a rough proportionality between the distance of galaxies and their receding velocity: since then, astronomers started to realize that the Universe was expanding. The observations by Edwin Hubble marked the start of modern observational cosmology; it is not by chance that the most ambitious space telescope orbiting the Earth is named after him.

1.2 The Striking Diversity of Galaxies

Even though the large diversity in morphology of nebulae was identified since the XVIII century, the most common classification scheme for galaxies in use today is

due, again, to Edwin Hubble (1926). Hubble noticed that galaxies could be roughly separated in two classes: elliptical galaxies, consisting of a round or flattened smooth distribution of light, and spiral galaxies, consisting of a flat disc with spiral structures extending from a central concentration of light (known as the bulge).

Hubble referred to elliptical and lenticular galaxies as "early-type", and spirals as "late-types" with no intent of this nomenclature to be an evolutionary path, contrary to popular belief (Hubble, 1927):

The nomenclature, it is emphasized, refers to position in the sequence, and temporal connotations are made at one's peril. The entire classification is purely empirical and without prejudice to theories of evolution.

The definition morphology of galaxies have been made quantitative by Sérsic in the Sixties, who proposed to fit the surface brightness profile of a galaxy (i.e. how the intensity of light varies from the center) with a parametric function of the form:

$$\Sigma(r) = \Sigma_e \times \exp \left(-b_n \left[\left(\frac{r}{r_e} \right)^{1/n} - 1 \right] \right)$$

where r_e is the radius within which the galaxy emits half of his brightness and Σ_e is the surface brightness at r_e . The value of n determines how concentrated the profile is, with particular cases of $n = 1$ corresponding to a disk-like profile, and $n = 4$ corresponding to a bulge-like profile.

Subsequent studies have shown that morphology of present-day galaxies is tightly correlated to other properties such as mass, color, and environment.

In general, elliptical galaxies have redder colors than spirals (Strateva et al., 2001; Blanton et al., 2003; Driver et al., 2006), reflecting the fact that the light of elliptical galaxies tends to be dominated by old stars, while spirals tend to be actively forming new stars. Higher-density environments tend to be dominated by early-type galaxies (Dressler, 1980, Blanton et al., 2005), and the most massive galaxies tend to be early-type as well (Kauffmann et al., 2003b).

In the local Universe, this dichotomy can be interpreted as being primarily an effect of mass (even though further studies such as Franx et al. 2008 hint that velocity dispersion might be a more fundamental parameter to describe this transition). Kauffmann et al. (2003b) have shown that the distinction between evolved early-type, red, quiescent objects, and late-type, blue, star-forming galaxies occurs at $M_* = 3 \times 10^{10} M_\odot$.

A similar bimodality in colors, star-formation rates, and morphology of galaxies has been observed all the way to $z \sim 2$ (e.g. Labbé et al. 2005, Kriek et al. 2006, Szomoru et al. 2012). However, while in the local Universe massive ($M_* > 10^{11} M_\odot$) galaxies constitute a substantially uniform population of red-and-dead objects, at $z \sim 1.5$ a high fraction (60%, compared to 10% in SDSS) of them is found to be star-forming, blue, and disk-like (Figure 1.1, van Dokkum et al. 2011). The fraction of quiescent galaxies increases towards lower redshifts while star-forming galaxies tend to dominate the galaxy counts at progressively lower mass (Brammer et al. 2011, Muzzin et al. 2014). Understanding the origin and the evolution of the galaxy

bimodality, and the process that quenches galaxies are perhaps the most fundamental questions of extragalactic astrophysics.

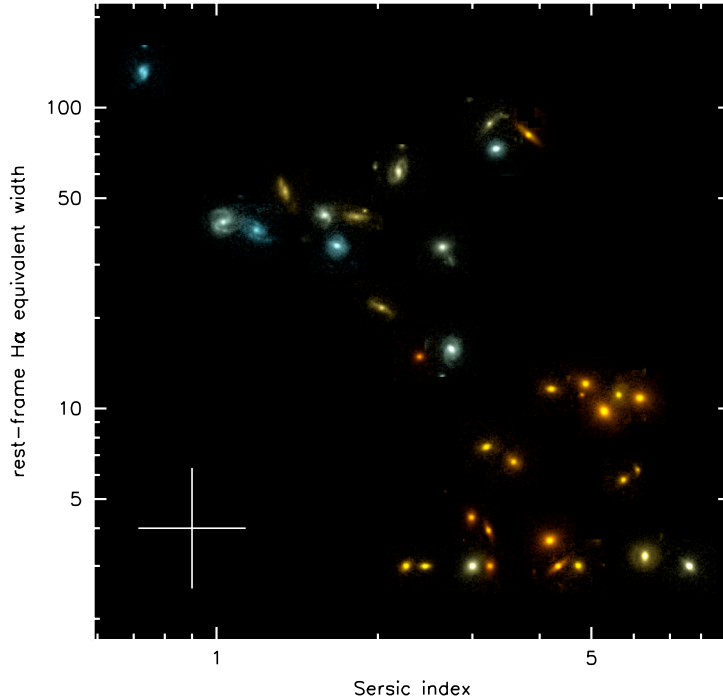


Figure 1.1: The diversity of massive galaxies at $1.0 < z < 1.5$ (from van Dokkum et al. 2011), in a mass selected sample ($\log M_*/M_\odot > 11$) from the 3D-HST survey. The relation between $\text{EW}(\text{H}\alpha)$, morphology (parametrized by the Sersic index) and color of galaxies shows that the high redshift population is made up of a group of quiescent, red, elliptical galaxies with low star-formation rates, complemented by blue, spiral-like, star-forming objects.

1.3 Measuring Star Formation through cosmic time

One of the most fundamental parameter describing a galaxy is the star formation rate (SFR), defined as the solar masses formed as stars per unit time. As the youngest stellar population emit the bulk of their energy in the rest-frame ultraviolet ($\lambda < 3000 \text{ \AA}$), the most direct way to measure SFRs consists in integrating the light of galaxies at those wavelengths. However, since stars form within clouds of gas and dust, the light they emit is at least partially attenuated and therefore any measure of SFR from the UV might be light might be severely underestimated.

One can either correct for the dust absorption, by for instance comparing the observed UV spectrum with the theoretical slope one would expect the spectrum to have (e.g. Meurer et al. 1995, Bouwens et al. 2009), or consider the additional contribution of the light absorbed in the UV and re-emitted at longer wavelengths (Bell et al. 2005, among others). Infrared measurements are however challenging

as well, and SFRs in the infrared are often inferred from observations at a single wavelength, from which the total IR luminosity is extrapolated under assumptions on the overall IR spectral shape.

Since young massive stars produce copious amounts of ionizing photons that ionize the surrounding gas, Hydrogen recombination lines (including the Balmer lines at optical wavelengths) represent the most traditional SFR indicator (Kennicutt 1998). The relation between the ionizing photon rate and the intensity of an hydrogen recombination line is dictated by quantum mechanics (e.g. Osterbrock & Ferland, 2006). Dust absorption affects optical Balmer lines to a lesser extent than UV - light, but dust corrections are still necessary. A commonly used technique consists in estimating the dust absorption in a system by comparing the ratio of the intensities of two emission lines (generally $H\alpha$ and $H\beta$) to that expected by quantum mechanics in the absence of dust.

More indirect SFR indicators are based on radio and X-ray emission, respectively based on the acceleration of cosmic rays in supernovae explosions and the number of high-mass X-ray binaries, both correlated with the presence of young stars. At these wavelengths however, active galactic nuclei often dominate the emission, making SFR measurements more uncertain.

A comprehensive measurement of the SFRs at large lookback times has necessarily to rely on different tracers at different redshifts. Various measurements (among others: Madau et al. 1996; Lilly et al. 1996; Bouwens et al. 2007; Karim et al. 2011; Sobral et al. 2013; Madau & Dickinson 2014) of the star formation rate density (SFRD) at different cosmic times give an indication of the star formation activity of the universe (from $z=8$ to 0). Even though large uncertainties in the determination of the SFRD still exist, the global picture is well established: the SFRD rises from the Big Bang to a peak at $z \sim 2$ ("Cosmic Noon"), and afterwards falls by a factor of approximately 10 to the current value (Figure 1.2). Measuring the time evolution of the SFRD has implications for the reionization of the Universe, the cosmic chemical evolution, the transformation of gas into stars and the buildup of stellar mass.

In order to understand the physical processes driving the evolution of the Universe, one would ideally want to go beyond the global description of the SFRD and trace galaxy evolution on a galaxy-by-galaxy base, by connecting star formation rates with other physical properties of galaxies. In that respect, with the building of large statistical samples (SDSS) it became possible to establish that, for star-forming galaxies, mass and star-formation rates are tightly correlated, with most of the objects having a linear (or slightly sublinear) relation between $\log M^*/M_\odot$ - $\log SFR$, with a relatively small scatter (0.2 dex, Brinchmann et al. 2004).

In the meanwhile, infrared telescopes (IRAS, *Spitzer*) had already led to the identification of a different class of star-forming galaxies, with infrared luminosities and star-formation rates 100 to 1000 times higher than those of the Milky Way (Lonsdale et al. 2006, and references therein). Those rare objects have been dubbed (U)LIRG, i.e. (Ultra)Luminous InfraRed Galaxies, and turned out to be mainly products of merging or interacting galaxies inducing huge bursts of star formation (e.g. Armus, Heckman & Miley, 1987).

Looking back in the past, ULIRG-like star-formation rates appeared to be more

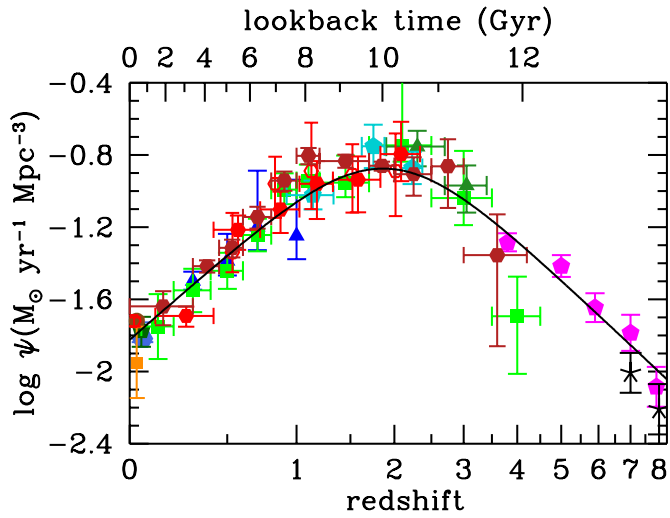


Figure 1.2: Evolution of the cosmic star formation density, from Madau & Dickinson (2014). The star formation rate of the Universe reached a peak around $z \sim 2$ and has declined by a factor of 10 since then. Determinations based on infrared measurements are shown in red, determinations based on UV measurements in blue/green/magenta.

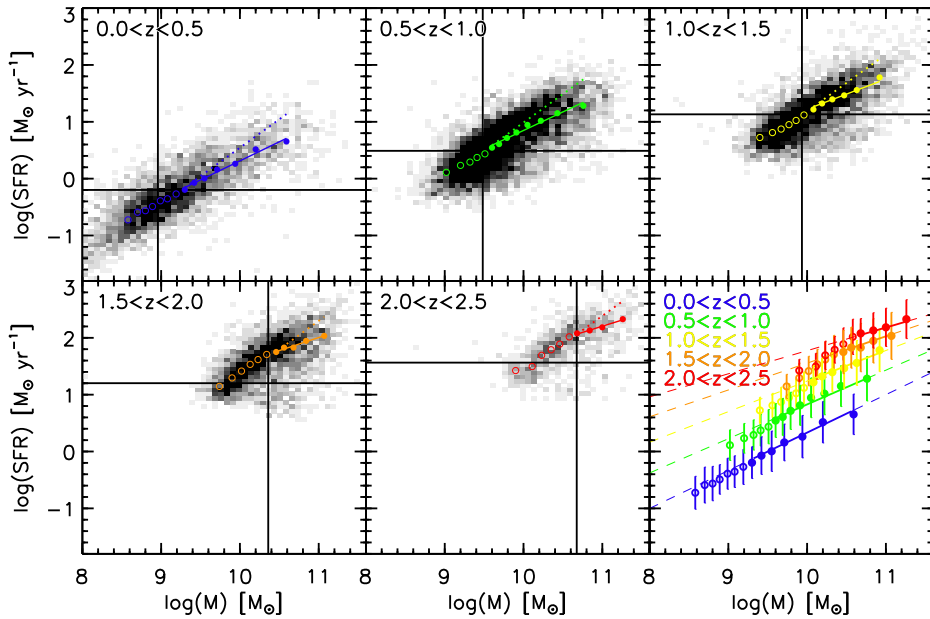


Figure 1.3: From Whitaker et al. 2012, the SFR-mass sequence for star-forming galaxies out to $z = 2.5$. At each redshift, more massive galaxies have higher SFRs than those of lower mass galaxies, with a non-linear slope. The normalization of the sequence increases towards higher redshifts.

prevalent (e.g. Lilly et al. 1996, Cowie et al. 1996). However subsequent studies showed that $z \sim 1$ star-forming galaxies, despite the similar high star-formation rates, had nothing in common with local (U)LIRGS, while instead resembled relaxed disks, with less than 20% of them being interacting systems (Zheng et al. 2004, Bell et al. 2005). Subsequent studies showed that a relation between stellar mass and star-formation rates, similar to that seen in the local Universe, was present for galaxies at high redshift too (Noeske et al. 2007, Elbaz et al. 2011, and others).

Since star-formation is thought to be regulated by the balance between the accretion rate of cold gas onto the galaxy and some feedback process (e.g., Dutton et al. 2010; Bouche et al. 2010), the star-forming main sequence may be a natural consequence of “cold mode accretion” (e.g., Birnboim & Dekel 2003), as the SFR is approximately a steady function of time and yields a relatively tight relationship between SFR and M_* .

The normalization of the star-forming main sequence increases towards higher redshifts (Karim et al 2010, Whitaker et al. 2012, Figure 1.3), with a slope that is generally steeper than that predicted by semi-analytical models of galaxy formation (e.g. Guo et al. 2010). The fact that the main sequence shifts towards lower values as the Universe gets older reflects a gradual decline of the average star-formation in most individual galaxies, as gas gets gradually exhausted, accompanied by an increase in the fraction of quenched galaxies (e.g. Muzzin et al. 2014).

1.4 Issues at high redshifts

Despite the invaluable technological advances of instruments and telescopes in the last twenty years, starting with the building of 8-10m class telescopes and the new generation of space telescopes (such as *Hubble* and *Spitzer*), measurements of high-redshift galaxies are still extremely challenging, and our knowledge of those systems is nowhere near to that we have of local galaxies.

In the first place, galaxies become fainter as their distances increase. Spectroscopy of high-redshift galaxies is therefore prohibitively time-consuming for all but the brightest sources. The most fundamental problem related to the absence of spectroscopy is that the redshift determination is uncertain. High-redshift surveys use multiband-photometry to obtain a spectral energy distribution (SED) of galaxies, and fit those with a set of modeled SEDs in order to derive redshifts and other physical properties of galaxies. Even in extragalactic fields covered by 20-30 different photometric bands spanning from the UV to the NIR photometric redshifts are hardly more precise than $\delta z / (1 + z) = 3\%$ once compared to spectroscopic redshifts of generally bright objects with emission lines (Skelton et al. 2014). Estimation of galaxy masses from photometry are affected by systematic uncertainties of the order of 0.3dex or more (e.g. Muzzin et al. 2009, Dahlen et al. 2013, Pacifici et al. 2014).

A second fundamental problem for observations at high redshift is that their light is strongly redshifted. Light from old stars (representing the bulk of mass in most galaxies) is redshifted into the infrared at redshifts higher than $z \sim 0.5$. This causes problems because of the inefficiency of infrared detectors, and the atmospheric absorption in those bands caused by water vapor. Even in the most ideal places for

infrared ground-based telescopes (dry locations at high altitude), the transparency of the Earth's atmosphere is limited except in a few infrared wavelength windows.

Our knowledge of ages, star-formation rates, and metallicities of galaxies relies often on spectral indicators at rest-frame optical wavelengths (such as D4000, Balmer and metal lines), which are challenging and time-consuming to measure at high redshift when they shift in the infrared. For instance, a well-calibrated standard indicator of the SFR is the already mentioned $H\alpha$ luminosity (Kennicutt, 1998). As a consequence of its shift into the near-IR at redshifts higher than $z \sim 0.5$ (8 billion years ago), studies of the evolution of star-formation rates covering a wide redshift range use diverse SFR indicators (such as UV, IR, [OII], SED fitting), relying on a set of assumptions and inter-calibrations. For each indicator, accessing fluxes correspondent to $SFR < 10 - 20M_{\odot}/\text{yr}$ becomes challenging, if not impossible, for individual sources at $z > 0.5$. The identification of samples of galaxies with low star formation at high redshift is therefore generally based on their rest-frame colors only, by selecting galaxies whose optical and near-IR light is dominated by an old stellar population.

An additional bias induced by ground-based spectroscopy is that samples for spectroscopy are generally optimized for observations in the atmospheric windows, and they consist generally in blue star-forming objects selected on the basis of their rest-frame UV emission (Steidel et al. 2004, and others), while continuum observations are available for limited samples of bright objects (Bezanson et al. 2013, van de Sande et al. 2013). The absence of bias-free and mass-complete samples of measurements of physical properties of galaxies such as ages and metallicities limits our understanding of the assembly history and the evolution of galaxies.

1.5 This Thesis

This thesis addresses several of the issues described in the previous section. In particular, we take advantage of a novel set of observations taken with the Wide Field Camera 3 (WFC3) grism onboard Hubble Space Telescope (HST), in the context of the 3D-HST survey (Figure 1.4, Brammer et al. 2012), in order to investigate the evolution of star-formation rates, emission line contributions and stellar population properties of both star-forming and quiescent galaxies, in mass selected samples at $0.5 < z < 2$. 3D-HST provides rest-frame optical spectra for a sample of ~ 10000 galaxies at $1 < z < 3.5$, the epoch when 60% of all star formation took place, the first galaxies stopped forming stars, and the structural regularity that we see in galaxies today must have emerged. Such a wide-field near-IR spectroscopic survey would be currently infeasible from the ground, since it probes a larger cosmic volumes thanks to the broad range of redshifts covered by the WFC3 grism, and targets every object in the field of view.

In **Chapter 2**, we combine the first available data from the 3D-HST survey (40 % of the entire survey) with those of ground-based surveys at lower redshift in order to evaluate the evolution of $EW(H\alpha)$, the equivalent width of $H\alpha$. Since $EW(H\alpha)$

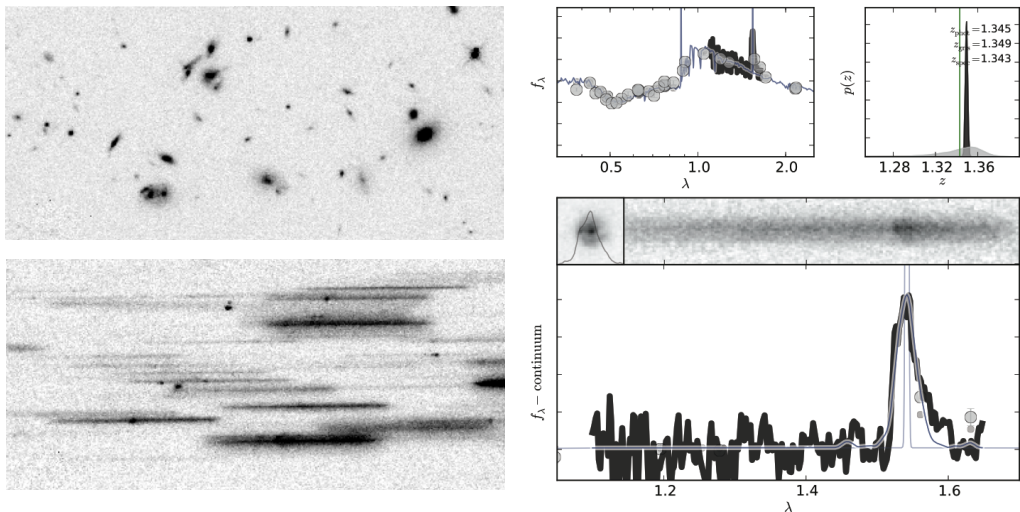


Figure 1.4: The 3D-HST survey provides spectra for all galaxies in a particular field with the WFC3/IR grism. The panels on the left show 50x28 arcsec cutouts of the F140W and G141 observations within the GOODS-South field, with wavelength increasing towards the right on the grism panel. Galaxy spectra are extracted in 2D and 1D (bottom right) and used in combination with the full SED of the objects (top center) in order to determine a redshift measurement which is greatly improved to that from photometry alone: the top-right panel shows the probability distribution of the redshift determined from the photometry alone (grey region), and that determined with the addition of grism data (black region), compared to a spectroscopic redshift (vertical line). Image from Brammer et al. (2012).

is defined as the ratio of the $H\alpha$ luminosity to the underlying stellar luminosity, it represents a measure of the current to past star formation, and it is therefore a model-independent, directly observed proxy for the specific star formation rate ($s\text{SFR}=\text{SFR}/M$). We find that at each redshift $\text{EW}(H\alpha)$ goes down with mass, and that at fixed mass the $\text{EW}(H\alpha)$ grows towards higher redshifts as $\text{EW}(H\alpha) = (1+z)^{1.8}$. This evolution is independent of stellar mass, and it is steeper than that predicted by models of galaxy evolution. We moreover predict the evolution of $\text{EW}(H\alpha)$ at higher redshift, finding that the contribution of emission lines to the total light of galaxies continues to increase at $z = 4 - 8$, with important consequences for spectroscopy and photometry of sources that will be accessed with James Webb Space Telescope.

In **Chapter 3** we investigate the SFRs of galaxies selected as quiescent on the basis of their optical and near-IR spectral energy distributions, which indicate an old stellar population. Spectral energy distribution fits for optically selected quiescent galaxies indicate SFRs even lower than those expected from gas recycling, assuming that the mass loss from evolved stars refuels star formation. However, optical and near-IR SED fitting can miss star formation if it is hidden behind high dust obscuration, and its ionizing radiation is reemitted in the mid-infrared. We therefore select spectroscopically confirmed quiescent galaxies in the 3D-HST survey, and measure

their dust-obscured SFRs with stacks of mid-infrared fluxes from *Spitzer*-24 μm , in five redshift bins centered on $z = 0.5, 0.9, 1.2, 1.7, 2.2$. We show that, at each redshift, SFRs of quiescent galaxies are 20-40 times lower than those of star-forming galaxies at the same redshift, indicating that quenching is very efficient even in the young Universe where typical SFRs on the main sequence reach hundreds of solar masses per year. The true SFRs of quiescent galaxies might be even lower than that, as we show that mid-infrared fluxes can be due also to processes uncorrelated with present star formation, such as dust heating by old stellar populations and circumstellar dust.

Chapter 4 focuses on the spectra of star-forming and quiescent galaxies from $z=0.5$ to $z=2$ in more detail, in order to determine their stellar ages. We stack spectra of quiescent and star-forming galaxies (selected on the basis of a rest-frame color-color technique), and fit them with commonly used stellar population synthesis models. We find that stellar population models fit the observations well at wavelengths lower than 6500 \AA , while they show systematic differences from the observed spectra at redder wavelengths. We show that quiescent galaxies have little emission line contribution, and those are consistent with SFR measurements from mid-infrared. The ages of quiescent galaxies implied by the models differ according to the model in use, but on average quiescent galaxies are young, i.e. younger than half of the age of the Universe at each redshift. For star-forming galaxies the inferred ages depend strongly on the assumed stellar population model and star-formation history.

In **Chapter 5** we take advantage of the full 3D-HST data to analyze how the $\text{EW}(\text{H}\alpha)$ depends on galaxy properties and in particular on the optical/near-IR spectral energy distribution shape of the galaxy, in the redshift range where $\text{H}\alpha$ can be observed with the HST/WFC3 grism ($0.7 < z < 1.5$). We demonstrate that galaxies with strong and weak $\text{H}\alpha$ are well separated in a rest-frame color-color diagram. For star-forming galaxies, we investigate how $\text{H}\alpha$ varies as a function of the rest-frame colors of the galaxy and how it relates to the specific star formation rate, measured from the ultraviolet and mid-infrared emission. At a fixed mass, red star-forming galaxies have lower $\text{EW}(\text{H}\alpha)$ than blue star-forming galaxies. We also show that, at fixed mass, the median specific star formation rates of galaxies decreases towards redder U-V colors, and that the dust absorption increases towards redder colors. We show that the overall variation of $\text{EW}(\text{H}\alpha)$ as a function of color can be explained by the combined effect of lower specific star formation rate and higher dust absorption for galaxies with redder colors.

Bibliography

Armus, L., Heckman, T., & Miley, G. 1987, *AJ*, 94, 831

Bell, E. F., Papovich, C., Wolf, C., et al. 2005, *ApJ*, 625, 23

- Bezanson, R., van Dokkum, P., van de Sande, J., Franx, M., & Kriek, M. 2013, *ApJL*, 764, L8
- Birnboim, Y., & Dekel, A. 2003, *MNRAS*, 345, 349
- Blanton, M. R., Hogg, D. W., Bahcall, N. A., et al. 2003, *ApJ*, 594, 186
- Blanton, M. R., Eisenstein, D., Hogg, D. W., Schlegel, D. J., & Brinkmann, J. 2005, *ApJ*, 629, 143
- Bouché, N., Dekel, A., Genzel, R., et al. 2010, *ApJ*, 718, 1001
- Bouwens, R. J., Illingworth, G. D., Franx, M., & Ford, H. 2007, *ApJ*, 670, 928
- Bouwens, R. J., Illingworth, G. D., Franx, M., et al. 2009, *ApJ*, 705, 936
- Brammer, G. B., Whitaker, K. E., van Dokkum, P. G., et al. 2011, *ApJ*, 739, 24
- Brinchmann, J., Charlot, S., White, S. D. M., et al. 2004, *MNRAS*, 351, 1151
- Cowie, L. L., Songaila, A., Hu, E. M., & Cohen, J. G. 1996, *AJ*, 112, 839
- Dahlen, T., Mobasher, B., Faber, S. M., et al. 2013, *ApJ*, 775, 93
- Dressler, A. 1980, *ApJ*, 236, 351
- Driver, S. P., Allen, P. D., Graham, A. W., et al. 2006, *MNRAS*, 368, 414
- Dutton, A. A., van den Bosch, F. C., & Dekel, A. 2010, *MNRAS*, 405, 1690
- Elbaz, D., Dickinson, M., Hwang, H. S., et al. 2011, *A&A*, 533, A119
- Franx, M., van Dokkum, P. G., Schreiber, N. M. F., et al. 2008, *ApJ*, 688, 770
- Hubble, E. P. 1926, *ApJ*, 64, 321
- Hubble, E. P. 1927, *The Observatory*, 50, 276
- Karim, A., Schinnerer, E., Martínez-Sansigre, A., et al. 2011, *ApJ*, 730, 61
- Kennicutt, R. C., Jr. 1998, *ApJ*, 498, 541
- Kriek, M., van Dokkum, P. G., Franx, M., et al. 2006, *ApJ*, 645, 44
- Kauffmann, G., Heckman, T. M., White, S. D. M., et al. 2003, *MNRAS*, 341, 54
- Labbé, I., Huang, J., Franx, M., et al. 2005, *ApJL*, 624, L81
- Lilly, S. J., Le Fevre, O., Hammer, F., & Crampton, D. 1996, *ApJL*, 460, L1
- Lonsdale, C. J., Farrah, D., & Smith, H. E. 2006, *Astrophysics Update* 2, 285
- Madau, P., Ferguson, H. C., Dickinson, M. E., et al. 1996, *MNRAS*, 283, 1388
- Madau, P., & Dickinson, M. 2014, *ARA&A*, 52, 415

- Meurer, G. R., Heckman, T. M., Leitherer, C., et al. 1995, *AJ*, 110, 2665
- Muzzin, A., van Dokkum, P., Franx, M., et al. 2009, *ApJL*, 706, L188
- Muzzin, A., van der Burg, R. F. J., McGee, S. L., et al. 2014, *ApJ*, 796, 65
- Noeske, K. G., Weiner, B. J., Faber, S. M., et al. 2007, *ApJL*, 660, L43
- Pacifici, C., da Cunha, E., Charlot, S., et al. 2015, *MNRAS*, 447, 786
- Skelton, R. E., Whitaker, K. E., Momcheva, I. G., et al. 2014, *ApJS*, 214, 24
- Sobral, D., Smail, I., Best, P. N., et al. 2013, *MNRAS*, 428, 1128
- Steidel, C. C., Shapley, A. E., Pettini, M., et al. 2004, *ApJ*, 604, 534
- Strateva, I., Ivezić, Ž., Knapp, G. R., et al. 2001, *AJ*, 122, 1861
- Szomoru, D., Franx, M., Bouwens, R. J., et al. 2011, *ApJL*, 735, L22
- van de Sande, J., Kriek, M., Franx, M., et al. 2013, *ApJ*, 771, 85
- van Dokkum, P. G., Brammer, G., Fumagalli, M., et al. 2011, *ApJL*, 743, L15
- Zheng, X. Z., Hammer, F., Flores, H., Assémat, F., & Pelat, D. 2004, *A&A*, 421, 847

2

H α EQUIVALENT WIDTHS FROM THE 3D-HST SURVEY: EVOLUTION WITH REDSHIFT AND DEPENDENCE ON STELLAR MASS

We investigate the evolution of the H α equivalent width, $EW(H\alpha)$, with redshift and its dependence on stellar mass, using the first data from the 3D-HST survey, a large spectroscopic Treasury program with the HST-WFC3. Combining our H α measurements of 854 galaxies at $0.8 < z < 1.5$ with those of ground based surveys at lower and higher redshift, we can consistently determine the evolution of the $EW(H\alpha)$ distribution from $z=0$ to $z=2.2$. We find that at all masses the characteristic $EW(H\alpha)$ is decreasing towards the present epoch, and that at each redshift the $EW(H\alpha)$ is lower for high-mass galaxies. We find $EW(H\alpha) \sim (1+z)^{1.8}$ with little mass dependence. Qualitatively, this measurement is a model-independent confirmation of the evolution of star forming galaxies with redshift. A quantitative conversion of $EW(H\alpha)$ to sSFR (specific star-formation rate) is model dependent, because of differential reddening corrections between the continuum and the Balmer lines. The observed $EW(H\alpha)$ can be reproduced with the characteristic evolutionary history for galaxies, whose star formation rises with cosmic time to $z \sim 2.5$ and then decreases to $z = 0$. This implies that $EW(H\alpha)$ rises to 400 \AA at $z = 8$. The sSFR evolves faster than $EW(H\alpha)$, as the mass-to-light ratio also evolves with redshift. We find that the sSFR evolves as $(1+z)^{3.2}$, nearly independent of mass, consistent with previous reddening insensitive estimates. We confirm previous results that the observed slope of the sSFR- z relation is steeper than the one predicted by models, but models and observations agree in finding little mass dependence.

Mattia Fumagalli; Shannon G. Patel; Marijn Franx; Gabriel Brammer; et al.
The Astrophysical Journal Letters, Volume 757, Issue 2, L22, 2012

2.1 Introduction

Several studies have combined different star formation indicators in order to study the evolution of star-forming galaxies (SFGs) with redshift. At a given redshift low mass galaxies typically form more stars per unit mass (i.e., specific star-formation rate, sSFR) than more massive galaxies (Juneau et al. 2005, Zheng et al. 2007, Damen et al. 2009). In addition the sSFR of galaxies with the same mass increases at higher redshift. However, semi-analytical models and observations are at odds with regards to the rate of decline of the sSFR towards low-redshift (Damen et al. 2009, Guo et al. 2010).

One of the main observational caveats is that most of the studies covering a wide redshift range use diverse SFR indicators (such as UV, IR, [OII], $H\alpha$, SED fitting). This is a consequence of the fact that it is difficult to use the same indicator over a wide range of redshifts. One therefore has to rely on various conversion factors, often intercalibrated at $z = 0$ and re-applied at higher redshift.

A well-calibrated standard indicator of the SFR is the $H\alpha$ luminosity (Kennicutt, 1998). However, $H\alpha$ is shifted into the infrared at $z > 0.5$, and it is difficult to measure due to the limitations of ground-based near-IR spectroscopy. Comparing measures of $H\alpha$ at different redshifts has therefore been a challenge. Most of the $H\alpha$ studies at high redshift are based on narrow-band photometry (e.g. the HiZELS survey, Geach et al. 2008).

The 3D-HST survey (Brammer et al., 2012) provides a large sample of rest-frame optical spectra with the WFC3 grism, which includes the $H\alpha$ emission in the redshift range $0.8 < z < 1.5$. Taking advantage of the first data from the survey (45% of the final survey products) we investigate for the first time the star formation history (SFH) of the Universe with $H\alpha$ spectroscopy, using a consistent SFR indicator over a wide redshift range.

We evaluate the dependence of the $H\alpha$ Equivalent Width, $EW(H\alpha)$, on stellar mass (M_*) and redshift (up to $z \sim 2$), comparing the 3D-HST data with other surveys in mass selected samples with $M_* > 10^{10} M_\odot$. Since $EW(H\alpha)$ is defined as the ratio of the $H\alpha$ luminosity to the underlying stellar continuum, it represents a measure of the current to past average star formation. It is therefore a model independent, directly observed proxy for sSFR.

We also derive SFRs from the $H\alpha$ fluxes. We evaluate the mean sSFR in stellar mass bins and study its evolution with redshift. The slope of the sSFR- z relation in different mass bins indicates how fast the star formation is quenched in galaxies of various masses. Finally, we compare our findings to other studies (both observations and models), discussing the physical implications and reasons for any disagreements.

2.2 Data

2.2.1 3D-HST

We select the sample from the first available 3D-HST data. They include 25 pointings in the COSMOS field, 6 in GOODS-South, 12 in AEGIS, 28 in GOODS-North¹. Spectra have been extracted with the aXe code (Kummel et al., 2009). Redshifts have been measured via the combined photometric and spectroscopic information using a modified version of the EAZY code (Brammer, van Dokkum, Coppi, 2008), as shown in Brammer et al. (2012). Stellar masses were determined using the FAST code by Kriek et al. (2009), using Bruzual & Charlot (2003) models and assuming a Chabrier (2003) IMF. The FAST fitting procedure relies on photometry from the NMBS catalogue (Whitaker et al. 2011) for the COSMOS and AEGIS fields, the MODS catalogue for the GOODS-N (Kajisawa et al. 2009) and the FIREWORKS catalogue for GOODS-S (Wuyts et al. 2008).

The mass completeness limit is $\log(M_*/M_\odot) > 10$ at $z=1.5$ (Wake et al. 2011, Kajisawa et al. 2010). We select objects with $0.8 < z < 1.5$; this resulted in a sample of 2121 galaxies with $\log(M_*/M_\odot) > 10$.

In slitless spectroscopy, spectra can be contaminated by overlapping spectra of neighboring galaxies. The aXe package provides a quantitative estimate of the contamination as a function of wavelength, which can be subtracted from the spectra. We conservatively use spectra where the average contribution of contaminants is lower than 10% and for which more than 75% of the spectrum falls on the detector. After this selection we have 854 objects in the redshift range $0.8 < z < 1.5$ (40% of the objects). The final sample is not biased with respect to the mass relative to the parent sample.

Line fluxes and EWs were measured as follows.² We fit the 1D spectra with a gaussian profile plus a linear continuum in the region where $H\alpha$ is expected to lie. We subtract the continuum from the fit and measure the residual flux within 3σ from the line center of the gaussian. Errors are evaluated including the contribution from the error on the continuum. We distinguish between detections and non-detections of $H\alpha$ with a S/N threshold of 3. The typical 3σ detection limit corresponds to $SFR = 2.8M_\odot \text{ yr}^{-1}$ at $z=1.5$ (Equation 2.2).

Due to the low resolution of the WFC3 grism, the $H\alpha$ and [NII] lines are blended. In this work $EW(H\alpha)$ therefore includes the contribution from [NII]. For the other datasets, which have higher spectral resolution, we combine $H\alpha$ and [NII] for consistency with 3D-HST.

2.2.2 SDSS

We retrieve masses and $EW(H\alpha)$ for the SDSS galaxies from the MPA-JHU catalogue of the SDSS-DR7. Masses are computed based on fits to the photometry, following Kauffmann et al. (2003) and Salim et al. (2007). At redshift $0.03 < z < 0.06$, for masses higher than $M_* = 10^{10}M_\odot$, the SDSS sample is spectroscopically complete

¹From program GO-11600 (PI: B. Weiner)

²Through the entire paper the quoted EWs are rest-frame values.

in stellar mass (Jarle Brinchmann, private communication). We consider as detections only measurements greater than 3\AA , as the ones with $EW < 3\text{\AA}$ are affected by uncertainties in the stellar continuum subtraction (Jarle Brinchmann, private communication).

In the redshift range $0.03 < z < 0.06$, the spectroscopic fiber of SDSS does not cover the entirety of most galaxies. As a consequence sSFR are evaluated with emission line fluxes and masses from the fiber alone.

2.2.3 VVDS

The VIMOS VLT Deep Survey (VVDS, Le Fèvre et al. 2005) is a wide optical selected survey of distant galaxies. $H\alpha$ is covered by the VIMOS spectrograph at $0.0 < z < 0.4$.

Lamareille et al. (2009) released a catalog of 20,000 galaxies with line measurements, complete down to $M_* = 10^{9.5}M_\odot$ at $z = 0.5$. Masses are retrieved from the VVDS catalog; they have been computed through a Bayesian approach based on photometry (equivalent to Kauffmann et al. 2003 and Tremonti et al. 2004), and are relative to a Chabrier IMF. We select a sample with redshift $0.2 < z < 0.4$ and $M_* > 10^{10.0}M_\odot$ containing 741 objects, of which 477 (64 %) have an $H\alpha$ measurement with $S/N > 3$. The percentage of $H\alpha$ detected objects drops to 32% at masses $M_* > 10^{11.0}M_\odot$.

2.2.4 High redshift data

Erb et al. (2006) published $EW(H\alpha)$ for galaxies selected with the BX criterion (Steidel et al. 2004), targeting SFGs at redshift $2.0 < z < 2.5$. We evaluate the completeness of the sample as follows. From the FIREWORKS catalogue (Wuyts et al. 2008) we reconstruct the BX selection and evaluate the fraction of objects with spectroscopically confirmed redshift $2.0 < z < 2.5$ that fall in the BX selection. Percentages are 44%, 32% and 27% for mass limited samples with $\log(M_*/M_\odot) = 10.0-10.5$, $\log(M_*/M_\odot) = 10.5-11$, $\log(M_*/M_\odot) > 11.0$.

2.3 The $EW(H\alpha)$ - mass relation

We first study how $EW(H\alpha)$ depends on stellar mass in each available data set. The 3D-HST sample has been divided in two redshift bins, $0.8 < z < 1.1$ and $1.1 < z < 1.5$. The results are shown in Figure 2.1. At each redshift, highest mass galaxies have lower $EW(H\alpha)$. Note however, that there is a large scatter in the relation. We quantify the trend in the following way: we determine the average $EW(H\alpha)$ in three 0.5 dex wide mass bins ($10.0 < \log(M_*/M_\odot) < 10.5$, $10.5 < \log(M_*/M_\odot) < 11$, $\log(M_*/M_\odot) > 11.0$) and evaluated its error through bootstrapping the sample. The mean $EW(H\alpha)$ in a given mass bin is obtained in two ways: (1) using only detected, highly SFGs (blue lines in Figure 2.1) and (2) using all galaxies but assigning $EW(H\alpha)=0$ to the objects detected in $H\alpha$ with $S/N < 3$ (red lines in Figure 2.1). For the $z = 2.2$ data,

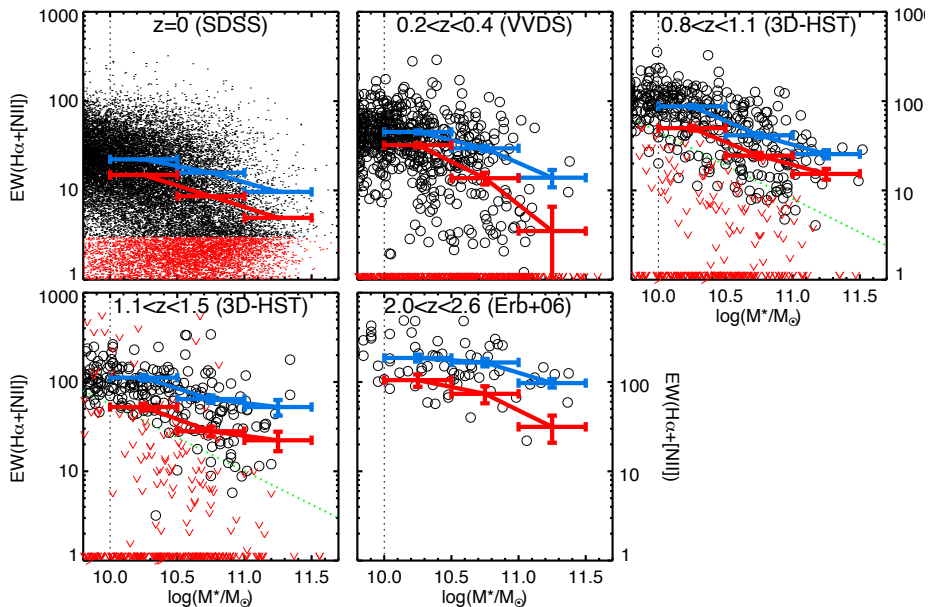


Figure 2.1: $EW(H\alpha)$ against mass, for different redshift samples. Vertical lines represent the limiting mass of the analysis. Black symbols are objects with $H\alpha$ detection with $S/N > 3$ and red arrows represent upper limits. The green diagonal lines represent the detection limit of the 3D-HST data. Blue solid lines represent the mean $EW(H\alpha)$ of detected SFGs, in 0.5 dex mass bins. Red solid lines represent the mean $EW(H\alpha)$ of all galaxies, assuming $EW(H\alpha)=0$ for non-detected objects. Errors of the means are computed with a bootstrap approach. At each redshift higher mass galaxies have lower $EW(H\alpha)$ than less massive objects.

we use the FIREWORKS catalog to establish the fraction of galaxies excluded by the BX selection and therefore give an estimation of $EW(H\alpha)$ for all galaxies.

Using either method we find that an $EW(H\alpha)$ -mass relation is in place at each redshift, not just for strongly star forming objects but also for the entire galaxy population. Galaxies in the lowest mass bin ($10.0 < \log(M_*/M_\odot) < 10.5$) have on average an $EW(H\alpha)$ which is 5 times higher than galaxies in the highest mass bin ($\log(M_*/M_\odot) > 11.0$).

We discuss the evolution of the $EW(H\alpha)$ -mass relation with redshift in the next section of the Letter. However, it is immediately evident from Figure 2.1 that the 3D-HST survey targets galaxies with $EW(H\alpha)$ typical of an intermediate regime between what is seen at $z=0$ and what is seen at higher redshift. In other words the $EW(H\alpha)$ -mass relation seems to rigidly shift towards higher $EW(H\alpha)$ at higher redshifts.

A considerable fraction of detected galaxies in 3D-HST have $EW(H\alpha) > 30\text{\AA}$, while in SDSS similar objects are extremely rare: 3.8%, 1.4% and 0.4% for increasing mass samples. This study can be seen as an extension of the findings of van Dokkum et al. (2011), who reported that massive galaxies at $z > 1$ show a wider range of $EW(H\alpha)$ compared to galaxies in the local Universe. Following this trend with redshift, in the $z > 2$ bin we find typical $EW(H\alpha)$ of 150\AA for SFGs. Such high

values of $EW(H\alpha)$ represent just 11% of the 3D-HST sample (14.6%, 8.1% and 4.7% respectively for increasing mass bins).

2.4 The Evolution of $EW(H\alpha)$ with redshift

The evolution of $EW(H\alpha)$ with redshift can be seen as an observational (i.e. model-independent) proxy for the sSFR- z relation. Figure 2.2 (top panels) shows the redshift evolution of the average $EW(H\alpha)$ in different mass bins for the detected SFGs (top left panel) and for all galaxies (top right panel). A substantial increase of the $EW(H\alpha)$ is seen at higher redshifts in both samples. We therefore infer that evolution of the SFR is not a byproduct of selection effects from different SFR indicators. At $0.8 < z < 1.5$, a galaxy has on average an $EW(H\alpha)$ that is 3-4 times higher than that of an object of comparable mass in the local universe. For each mass bin we parametrize the redshift evolution of the $EW(H\alpha)$ as follows:

$$EW(H\alpha)(z) \sim A \times (1+z)^p \quad (2.1)$$

The coefficient p has an average value of 1.8, with little dependence on mass (best fit values are listed in Table 2.1). As can be deduced from Table 2.1 there may be a weak mass dependence such that the relations steepen with mass; however, the difference between the slopes at the lowest and highest mass bin is not statistically significant.

This indicates that the decrease of $EW(H\alpha)$ happens at the same rate for all galaxies irrespectively of their masses. As seen in the right panel of Figure 2.2, the addition of non-SFGs amounts to a negative vertical shift in the $EW(H\alpha)$ but not to a change in the slope of the relation.

An uncertainty is the effect of dust on the $EW(H\alpha)$. Without more measurements we cannot state what effect dust has, and in literature there is disagreement on the relative extinction suffered by the nebular emission lines and the underlying stellar continuum (Calzetti et al. 2000, Erb et al. 2006, Wuyts et al. 2011). However, the data motivated model described in Section 6 suggests that dust has a mild effect on the $EW(H\alpha)$.

2.5 The sSFR($H\alpha$) - mass relation and its evolution with redshift

The $EW(H\alpha)$ has the advantage that it is a direct observable, but it is more difficult to interpret than a more physical quantity like the specific star formation rate. The latter can only be derived with a proper extinction correction for $H\alpha$. We lack this information, as we do not have a proper Balmer decrement measurement. In the following we briefly explore the specific star formation rate (sSFR) evolution implied by assuming no extinction and later discuss the effect of a dust correction to the measured slopes of the sSFR- z relation.

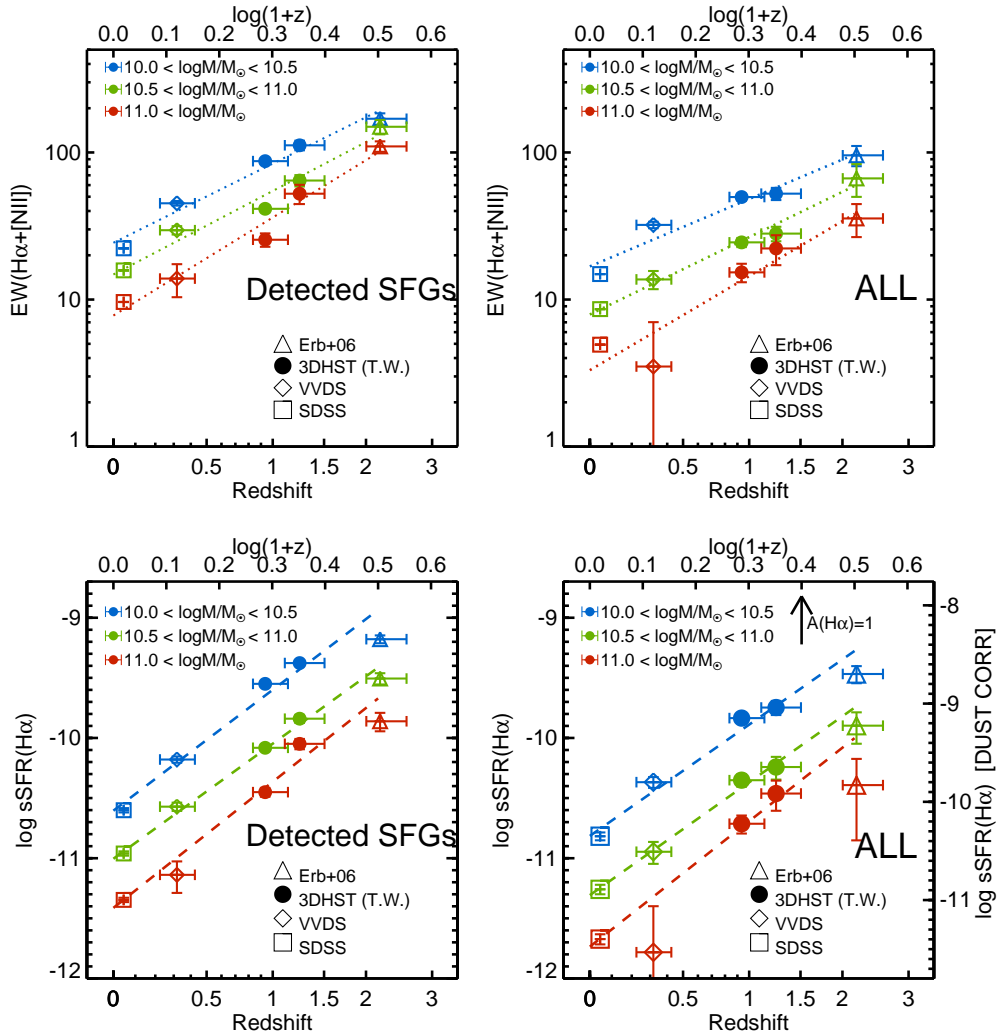


Figure 2.2: Evolution of $EW(H\alpha)$ (top) and $sSFR(H\alpha)$ (bottom) with redshift, in different mass bins, for SFGs (left) and all objects (right). Errors on the average EWs have been evaluating through bootstrapping. Dotted lines are the best fit power laws $EW(z) \sim (1+z)^p$. At fixed mass the average $EW(H\alpha)$ and $sSFR(H\alpha)$ increase with redshift, with a power law of $EW(H\alpha) \sim (1+z)^{1.8}$ and $sSFR(H\alpha) \sim (1+z)^{3.3}$ with little mass dependence. The effect of a luminosity dependent dust correction (Garn et al. 2010) correction is shown by the right axis. The effect of $A(H\alpha)=1$ is shown by the black arrow.

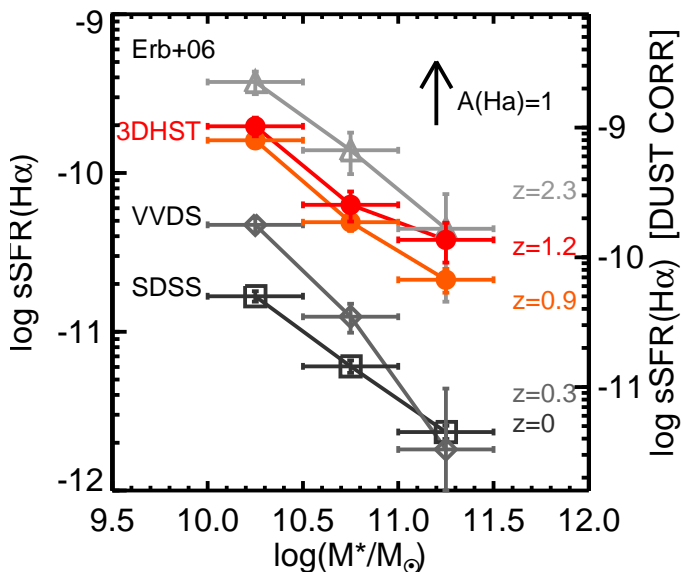


Figure 2.3: Mean values of $sSFR(H\alpha)$ in 0.5 dex mass bins at various redshift for SDSS, VVDS, 3D-HST and from Erb et al. (2006). At each redshift more massive galaxies have less $sSFR(H\alpha)$ than less massive ones. The effect of a luminosity dependent dust correction (Garn et al. 2010) correction is shown by the right axis. The effect of $A(H\alpha)=1$ is shown by the black arrow.

The SFR is derived from the $H\alpha$ flux³ using Kennicutt (1998):

$$SFR(H\alpha)[M_{\odot}yr^{-1}] = 7.9 \times 10^{-42} \times L(H\alpha)[erg/s] \times 10^{-0.24} \quad (2.2)$$

where the $10^{-0.24}$ factor accounts for a conversion to the Chabrier IMF, from Salpeter (as in Muzzin et al. 2010).

Figure 2.3 shows the mean value of $sSFR(H\alpha)$ in different stellar mass bins, at different redshifts. In each redshift bin higher mass galaxies have lower $sSFR(H\alpha)$.

In Figure 2.2 (bottom panels) we show the redshift evolution of the average $sSFR(H\alpha)$ in different mass bins for detected SFGs (bottom left panel) and for all galaxies (bottom right panel). A typical galaxy at $z=1.5$ has as $sSFR(H\alpha)$ 15-20 times higher than a galaxy of the same mass at $z=0$. In each mass bin we fit the evolution of the $sSFR$ in redshift with a power law:

$$sSFR(z) \sim B_M \times (1+z)^n \quad (2.3)$$

obtaining a value of $n = 3.2 \pm 0.1$. As can be deduced from Table 2.1 there may be a weak mass dependence such that the relations steepen with mass; however, the slopes at the lowest and highest mass bin are not statistically different.

³We assume a $[NII]/(H\alpha+[NII])$ ratio of 0.25 for the 3D-HST sources.

Table 2.1: Slopes of EW-z and sSFR-z Relation

$\log(M_*/M_\odot)$	EW(det)	EW(all)	sSFR(det)	sSFR(all)
10.0-10.5	1.79 ± 0.18	1.52 ± 0.21	3.32 ± 0.08	3.06 ± 0.13
10.5-11.0	1.89 ± 0.20	1.75 ± 0.13	3.18 ± 0.09	3.11 ± 0.18
11.0-11.5	2.21 ± 0.22	2.12 ± 0.43	3.50 ± 0.12	3.45 ± 0.26

The sSFR-z relation is steeper than the EW-z relation, because of the additional evolution of the M/L ratio:

$$EW/sSFR \sim L(H\alpha)/L_R \times M_*/(K * L(H\alpha)) \sim M/L_R \quad (2.4)$$

where K is the conversion factor in Equation 2.2 and L_R is the R-band luminosity.

Implementing a luminosity dependent dust correction for $H\alpha$ (Garn et al. 2010, shown with the right axis in Figure 2.2, bottom right) would increase the value of n to 3.7 ± 0.1 . However, several studies (Sobral et al. 2012, Dominguez et al. 2012, Momcheva et al., submitted) have indicated that a better indicator for the $H\alpha$ extinction at different redshifts is the stellar mass, and that the $H\alpha$ extinction depends strongly on mass but little on redshift (at constant mass). The Garn & Best 2010 relation gives median $A(H\alpha)$ of 1, 1.5 and 1.7 mag for the increasing mass bins in this study. A mass-dependent dust correction impacts the normalization of the sSFR but not the slope n .

Our implied evolution of the sSFR compares well to results from literature. For example, Damen et al. (2009) found $n = 4 \pm 1$ based on UV + IR inferred sSFRs, and Karim et al. (2011) found $n = 3.50 \pm 0.02$ for SFGs and $n = 4.29 \pm 0.03$ for all galaxies, based on stacked radio imaging.

All results indicate an evolution which is steeper with redshift than semianalytical models (Guo & White 2008, Guo et al. 2011), who find slopes close to $n=2.5$. All studies find that the slope does not depend on the stellar mass out so $z=2$. In short, our results are consistent with previous determinations.

2.6 Linking the characteristic SFH of galaxies and $EW(H\alpha)$

We compare the observed evolution of $EW(H\alpha)$ to what might be expected from other observations. We construct the typical SFH of a galaxy with mass $\sim 10^{11} M_\odot$ at $z=0$. As a starting point, we assume that the cumulative number density remains constant with redshift (similar to van Dokkum et al. 2010, Papovich et al. 2011, Patel et al. 2012). We use the mass functions of Marchesini et al. (2009) and Papovich et al. (2011), and we show the resulting mass evolution in Figure 2.4c. We determine the SFR at these masses from Damen et al. (2009), Papovich et al. (2011) and Smit et al. (2012), and we fit a simple curve to these values (indicated by the curve in Figure 2.4a). This evolutionary history reproduces the mass evolution well (Figure 2.4c).

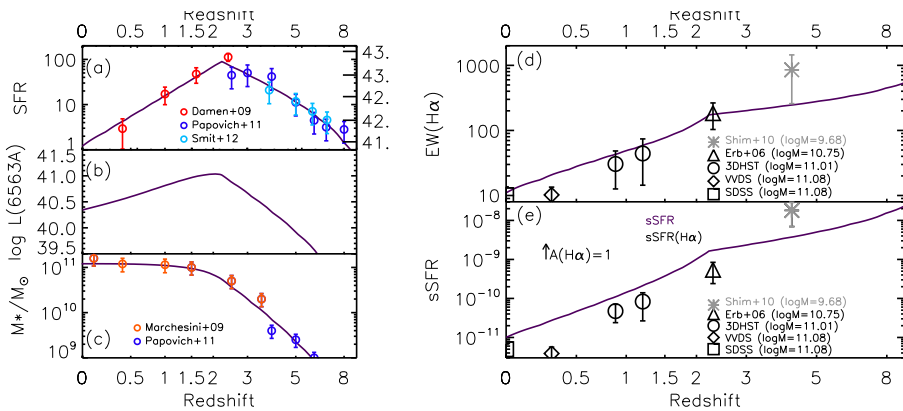


Figure 2.4: Comparison of observed $EW(H\alpha)$ with predictions from a simple observational supported model, at different redshifts. (a) Input SFH, and $H\alpha$ Luminosity (b) Luminosities at 6563 Å, from the Bruzual & Charlot 2003 code. (c) Mass growth. (d) Evolution of $EW(H\alpha)$ with redshift. (e) Evolution of sSFR with redshift. Data points are mean $EW(H\alpha)/sSFR(H\alpha)$ of observed galaxies with mass in a 0.3 dex bin around the typical mass of the model at a given redshift.

Next we calculate the implied $EW(H\alpha)$: $L(H\alpha)$ is derived using Equation 2.2, and Bruzual & Charlot 2003 models are used to calculate the stellar continuum, assuming solar metallicity (Figure 2.4b). The predicted $EW(H\alpha)$ rises monotonically to high redshift, reaching 400\AA at $z=8$ (Figure 2.4d). The predicted $EW(H\alpha)$ corresponds surprisingly well to the observed $EW(H\alpha)$. Even the $z=4$ detections by Shim et al. (2011) based on broadband IRAC photometry are consistent within the errors. Apparently, our simple method produces a robust prediction of the evolution of $EW(H\alpha)$. We note that the implied sSFR (Figure 2.4e) is higher than expected from straight measurement of $L(H\alpha)$, consistently with significant dust extinction. One magnitude of extinction for $H\alpha$ is needed to reconcile this discrepancy.

It is remarkable that our prediction worked well for $EW(H\alpha)$: the average evolution of galaxies was derived from the evolution of the mass function and SFR, which carry significant (systematic) uncertainties when derived from observations; whereas the $EW(H\alpha)$ is a direct observable.

2.7 Conclusions

We have used the 3D-HST survey to measure the evolution of the $EW(H\alpha)$ from $z=0$ to $z=2$. We show that the $EW(H\alpha)$ evolves strongly with redshift, at a constant mass, like $(1+z)^{1.8}$. The evolution is independent of stellar mass. The equivalent width goes down with mass (at constant redshift). The increase with redshift demonstrates the strong evolution of star forming galaxies, using a consistent and completely model independent indicator. We explore briefly the implied sSFR evolution, ignoring dust extinction. We find that the evolution with redshift is strong ($sSFR \sim (1+z)^{3.2}$). This stronger evolution is expected as the mass-to-light ratio

of galaxies evolves with time, and this enters the correction from EW to sSFR. The increase with redshift is faster than predicted by semi-analytical models (e.g., Guo & White 2008), consistent with earlier results.

We construct the characteristic SFH of a $10^{11}M_{\odot}$ galaxy. This simple history reproduces the observed evolution of the EW(H α) to $z=2.5$, and even to $z=4$. It implies that the EW(H α) continues to increase to higher redshifts, up to 400 \AA at $z=8$. This has a significant impact for the photometry and spectroscopy of these high redshift sources.

The study can be expanded in the future when the entire 3D-HST survey will be available, doubling the sample and including the ACS grism. In addition to increased statistics, the ACS grism will allow evaluation of the Balmer decrement and therefore a precise dust corrected evaluation of SFR. Moreover, a statistically significant H α sample at $z \sim 1$ will be central to understand the composition, the scatter and the physical origin of the so called ‘star-forming-main sequence’.

We thank the referee for providing valuable comments, and Jarle Brinchmann, David Sobral and Simone Weinmann for useful discussions. We acknowledge funding from ERC grant HIGHZ no. 227749.

Bibliography

- Brammer, G. B., van Dokkum, P. G., & Coppi, P. 2008, *ApJ*, 686, 1503
- Brammer, G., van Dokkum, P., Franx, M., et al. 2012, arXiv:1204.2829
- Bruzual, G., & Charlot, S. 2003, *MNRAS*, 344, 1000
- Calzetti, D., Armus, L., Bohlin, R. C., et al. 2000, *ApJ*, 533, 682
- Chabrier, G. 2003, *ApJL*, 586, L133
- Damen, M., Förster Schreiber, N. M., Franx, M., et al. 2009, *ApJ*, 705, 617
- Damen, M., Labbé, I., van Dokkum, P. G., et al. 2011, *ApJ*, 727, 1
- Domínguez, A., Siana, B., Henry, A. L., et al. 2012, arXiv:1206.1867
- Erb, D. K., Steidel, C. C., Shapley, A. E., et al. 2006, *ApJ*, 647, 128
- Garn, T., & Best, P. N. 2010, *MNRAS*, 409, 421
- Garn, T., Sobral, D., Best, P. N., et al. 2010, *MNRAS*, 402, 2017
- Geach, J. E., Smail, I., Best, P. N., et al. 2008, *MNRAS*, 388, 1473
- Guo, Q., & White, S. D. M. 2008, *MNRAS*, 384, 2
- Guo, Q., White, S., Li, C., & Boylan-Kolchin, M. 2010, *MNRAS*, 404, 1111

- Guo, Q., White, S., Boylan-Kolchin, M., et al. 2011, *MNRAS*, 413, 101
- Juneau, S., Glazebrook, K., Crampton, D., et al. 2005, *ApJL*, 619, L135
- Kajisawa, M., Ichikawa, T., Tanaka, I., et al. 2009, *ApJ*, 702, 1393
- Kajisawa, M., Ichikawa, T., Yamada, T., et al. 2010, *ApJ*, 723, 129
- Karim, A., Schinnerer, E., Martínez-Sansigre, A., et al. 2011, *ApJ*, 730, 61
- Kauffmann, G., Heckman, T. M., White, S. D. M., et al. 2003, *MNRAS*, 341, 33
- Kennicutt, R. C., Jr. 1998, *ApJ*, 498, 541
- Kriek, M., van Dokkum, P. G., Labbé, I., et al. 2009, *ApJ*, 700, 221
- Kümmel, M., Walsh, J. R., Pirzkal, N., Kuntschner, H., & Pasquali, A. 2009, *PASP*, 121, 59
- Lamareille, F., Brinchmann, J., Contini, T., et al. 2009, *A&A*, 495, 53
- Le Fèvre, O., Vettolani, G., Garilli, B., et al. 2005, *A&A*, 439, 845
- Marchesini, D., van Dokkum, P. G., Förster Schreiber, N. M., et al. 2009, *ApJ*, 701, 1765
- Momcheva, I., Lee, J. C., Ly, C., et al. 2012, arXiv:1207.5479
- Muzzin, A., van Dokkum, P., Kriek, M., et al. 2010, *ApJ*, 725, 742
- Papovich, C., Finkelstein, S. L., Ferguson, H. C., Lotz, J. M., & Giavalisco, M. 2011, *MNRAS*, 412, 1123
- Patel, S. G., van Dokkum, P. G., Franx, M., et al. 2012, arXiv:1208.0341
- Salim, S., Rich, R. M., Charlot, S., et al. 2007, *ApJS*, 173, 267
- Shim, H., Chary, R.-R., Dickinson, M., et al. 2011, *ApJ*, 738, 69
- Smit, R., Bouwens, R. J., Franx, M., et al. 2012, arXiv:1204.3626
- Sobral, D., Best, P. N., Matsuda, Y., et al. 2012, *MNRAS*, 420, 1926
- Steidel, C. C., Shapley, A. E., Pettini, M., et al. 2004, *ApJ*, 604, 534
- Tremonti, C. A., Heckman, T. M., Kauffmann, G., et al. 2004, *ApJ*, 613, 898
- van Dokkum, P. G., Whitaker, K. E., Brammer, G., et al. 2010, *ApJ*, 709, 1018
- van Dokkum, P. G., Brammer, G., Fumagalli, M., et al. 2011, *ApJL*, 743, L15
- Wake, D. A., Whitaker, K. E., Labbé, I., et al. 2011, *ApJ*, 728, 46
- Whitaker, K. E., Labbé, I., van Dokkum, P. G., et al. 2011, *ApJ*, 735, 86
- Wuyts, S., Labbé, I., Schreiber, N. M. F., et al. 2008, *ApJ*, 682, 985
- Wuyts, S., Förster Schreiber, N. M., Lutz, D., et al. 2011, *ApJ*, 738, 106
- Zheng, X. Z., Bell, E. F., Papovich, C., et al. 2007, *ApJL*, 661, L41

HOW DEAD ARE DEAD GALAXIES? MID-INFRARED FLUXES OF QUIESCENT GALAXIES AT REDSHIFT $0.3 < z < 2.5$: IMPLICATIONS FOR STAR-FORMATION RATES AND DUST HEATING

We investigate star-formation rates (SFR) of quiescent galaxies at high redshift ($0.3 < z < 2.5$) using 3D-HST WFC3 grism spectroscopy and *Spitzer* mid-infrared data. We select quiescent galaxies on the basis of the widely used UVJ color-color criteria. Spectral energy distribution (SED) fitting (rest-frame optical and near-IR) indicates very low star-formation rates for quiescent galaxies ($\text{sSFR} \sim 10^{-12} \text{yr}^{-1}$). However, SED fitting can miss star formation if it is hidden behind high dust obscuration and ionizing radiation is re-emitted in the mid-infrared. It is therefore fundamental to measure the dust-obscured SFRs with a mid-IR indicator. We stack the MIPS- $24\mu\text{m}$ images of quiescent objects in five redshift bins centered on $z = 0.5, 0.9, 1.2, 1.7, 2.2$ and perform aperture photometry. Including direct $24\mu\text{m}$ detections, we find $\text{sSFR} \sim 10^{-11.9} \times (1+z)^4 \text{yr}^{-1}$. These values are higher than those indicated by SED fitting, but at each redshift they are 20-40 times lower than those of typical star-forming galaxies. The true SFRs of quiescent galaxies might be even lower, as we show that the mid-IR fluxes can be due to processes unrelated to ongoing star formation, such as cirrus dust heated by old stellar populations and circumstellar dust. Our measurements show that star-formation quenching is very efficient at every redshift. The measured SFR values are at $z > 1.5$ marginally consistent with the ones expected from gas recycling (assuming that mass loss from evolved stars refuels star formation) and well below that at lower redshifts.

Mattia Fumagalli; Ivo Labbé; Shannon G. Patel; Marijn Franx; et al.
The Astrophysical Journal, Volume 796, Issue 1, article id. 35, 11 pp., 2014

3.1 Introduction

A bimodal distribution in galaxy properties (star-formation rate, size, morphology) has been observed in the local Universe (e.g. Kauffmann et al. 2003). This bimodality is made of blue, predominantly late-type galaxies, whose emission is dominated by young stellar populations and experiencing significant level of star formation, complemented by red, early-type (elliptical or S0) galaxies dominated by an old stellar population with little or absent star formation.

The bimodality has been observed all the way to $z \sim 2$ (Labbé et al. 2005, Kriek et al. 2006, Ilbert et al. 2010, Brammer et al. 2011, Whitaker et al. 2013).

Specific star-formation rates (sSFR) from spectral energy distribution (SED) fitting and equivalent widths from emission lines indicate for quiescent galaxies very low values ($\log_{10}\text{sSFR} \cdot \text{yr} < -12$) even at high redshift (Ciambur et al. 2013, Kriek et al. 2006, Whitaker et al. 2013), suggesting that these galaxies really are dead.

These levels of star formation are much lower than expected. Even if the galaxy would have stopped accreting new gas from the intergalactic medium, some gas should always become available again for star formation due to gas recycled from evolved stages of stellar evolution (e.g. Leitner & Kravtsov, 2010). If the low levels of star formation are confirmed, it could have important implications for gas recycling and the effectiveness of quenching at high redshift. Alternatively, it is possible that amounts of star formation have been overlooked in previous studies because of heavy obscuration by dust.

To address this question, in this paper we determine the obscured SFRs of quiescent galaxies up to redshift $z \sim 2.5$ using their $24\mu\text{m}$ emission. In Section 2, we discuss the data. In Section 3, we describe the selection of QGs, and compare their SFRs from optical and near-infrared (IR) SED fitting to the values expected from the recycling of gas from mass loss. We additionally evaluate how much obscured star formation might be hidden in our selection: this proves the need of looking at a mid-IR indicator for SFR. In Section 4, we stack $24\mu\text{m}$ thumbnails of QGs in order to measure their obscured SFR. We evaluate possible contributions to the mid-IR fluxes of QGs in Section 5. We discuss our findings in Section 6 and summarize them in Section 7. Through the paper we assume a standard cosmology with $H_0 = 70\text{km s}^{-1} \text{Mpc}^{-1}$, $\Omega_M = 0.30$, and $\Omega_\Lambda = 0.70$ (Komatsu et al. 2011).

3.2 Data

The 3D-HST Survey (van Dokkum et al. 2011; Brammer et al. 2012) is a 600 arcmin^2 survey using the Hubble Space Telescope (HST) to obtain complete, unbiased low-resolution near-IR spectra for thousands of galaxies. (Cycles 18 and 19, PI: van Dokkum).

It targets five fields (COSMOS, GOODS-S, GOODS-N¹, AEGIS, UDS) where a wealth of ancillary multi-wavelength data are available (U band to $24\mu\text{m}$); they are crucial for interpreting spectra that often contain a single emission line, if any. The

¹GOODS-N has been taken as part of program GO-11600 (PI: B. Weiner) and integrated into 3D-HST

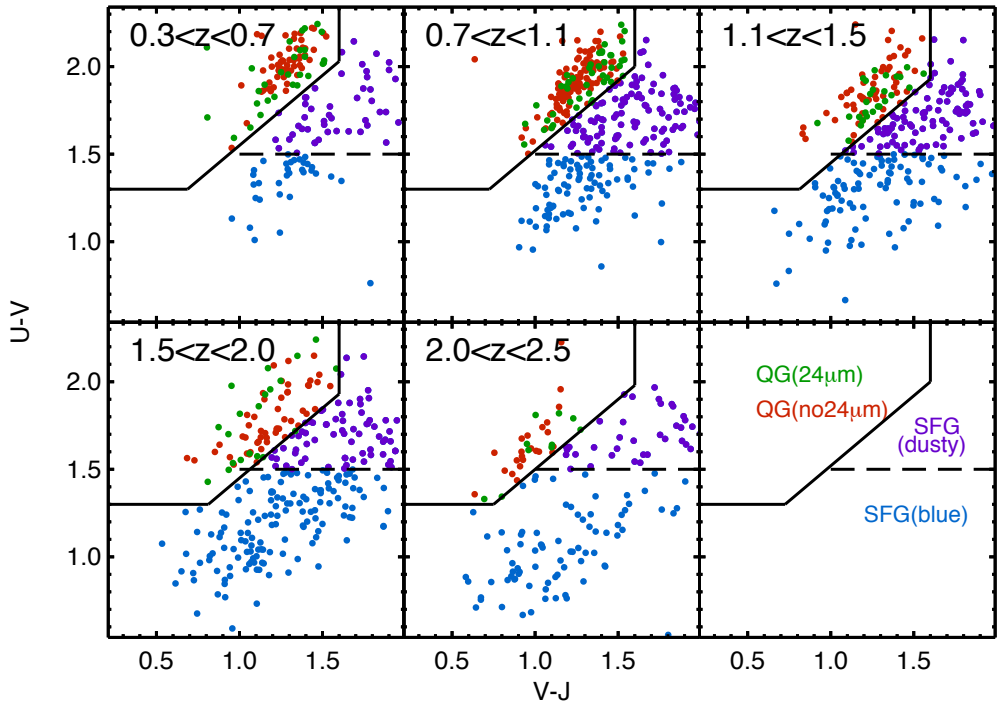


Figure 3.1: UVJ selection in different redshift bins, for mass-selected samples ($\log_{10}(M_*/M_\odot) > 10.3$). The Whitaker et al. (2012) boundary divides (solid black line) quiescent and star-forming galaxies. SFGs are subdivided into dusty ($U - V > 1.5$, purple dots) and unobscured ($U - V < 1.5$, blue dots). QGs are color coded according to the presence of a $24\mu\text{m}$ detection. We notice that $24\mu\text{m}$ -detected galaxies do not preferentially lie in a particular locus of the UVJ diagram.

3D-HST photometric catalogue is described in detail in Skelton et al. (2014). It contains ~ 170000 sources, detected on a noise-equalized combination of the F125W, F140W and F160W images. The completeness of 3D-HST as a function of magnitude is evaluated by comparing the number of detections in the catalog to those in a deeper image of GOODS-S: the two of them deviate at magnitudes fainter than $F160 = 25$ mag.

The WFC3 grism spectra have been extracted with a custom pipeline, described in Momcheva et al. (2014, in prep). Redshifts have been measured via the combined photometric and spectroscopic information using a modified version of the EAZY code (Brammer et al. 2008). The precision of redshifts is proven to be $\sigma(\frac{dz}{1+z}) = 0.3\%$ (Brammer et al. 2012, Momcheva et al. 2013).

Accurate redshifts allow the derivation of accurate rest-frame fluxes: we interpolate rest-frame filters from the observed SED with the Inter-rest code (Taylor et al., 2009), based on the algorithm by Rudnick et al (2003). Stellar masses have been determined using the FAST code by Kriek et al. (2009), using Bruzual & Charlot (2003) models, and assuming exponentially declining star-formation histories (with

e-folding times $\log_{10}(\tau/yr)$ ranging from 10^7 to 10^{11} yr), solar metallicity and a Chabrier (2003) IMF. The 3D-HST catalogs are evaluated to be 90% complete in stellar mass down to $\log_{10}(M_*/M_\odot) > 9.4$ at $z < 2.5$ (Tal et al. 2014).

In this paper we restrict the analysis to the GOODS-N and GOODS-S fields, for which very deep *Spitzer*-MIPS ($S_{24\mu m} = 10\mu Jy$, 3σ) data are available (Dickinson et al., 2003), necessary for inferring low levels of SF. The MIPS $24\mu m$ beam has a FWHM of 6 arcsec, therefore confusion and blending effects are unavoidable in deep observations at this resolution. We perform photometry using a source-fitting algorithm (Labbé et al. 2006, Wuyts et al. 2007) that takes advantage of the higher resolution information contained in the F160W images, as described in the Appendix. This method produces a model PSF for the image with the broader native PSF (MIPS- $24\mu m$ in our case), which is then used to estimate the flux distribution of each source identified in the detection image (F160W) segmentation map output by SExtractor. For each individual object, the flux from neighboring sources (closer than 10 arcsec) is fitted and subtracted, allowing for a reliable aperture flux measurement of individual objects.

Total IR luminosities ($L_{IR} = L(8 - 1000\mu m)$) were derived from the observed $24\mu m$ fluxes, on the basis of a single template that is the average of Dale & Helou (2002) templates with $1 < \alpha < 2.5$, following Wuyts et al. (2008; see also Franx et al. 2008, Muzzin et al. 2010), and in good agreement with recent *Herschel*/PACS measurements by Wuyts et al. (2011). SFRs are determined from the IR emission as in Bell et al. (2005) for a Chabrier IMF: $SFR(IR) = 0.98 \times 10^{-10} L_{IR}(L_\odot)$.² This quantity accounts properly just for obscured SF.

We derive SFRs without using data at wavelengths longer than $24\mu m$ because photometry from the PACS and SPIRE instruments on *Herschel* in the GOODS fields is not as deep as that from MIPS- $24\mu m$. We evaluate the potential for detecting low SFRs with the *Herschel* instruments, by using the PACS and SPIRE detection limits (Elbaz et al. 2011) to SFRs: we extrapolate total IR luminosities from monochromatic fluxes, and convert them to SFR as described above. We find that at $z = 1$ the PACS- $100\mu m$ and $160\mu m$ photometry is able to detect SFRs higher than $\sim 2M_\odot/yr$ (1σ), and SPIRE-250 higher than $\sim 5M_\odot/yr$ (1σ), while at the same redshift MIPS- $24\mu m$ is one order of magnitude deeper ($\sim 0.3M_\odot/yr$). The same conclusion holds true at $z = 2$, with detection limits for MIPS- $24\mu m$, PACS- $100\mu m$, PACS- $160\mu m$ and SPIRE- $250\mu m$ being respectively $\sim 2M_\odot/yr$, $\sim 20M_\odot/yr$, $\sim 10M_\odot/yr$, $\sim 20M_\odot/yr$ (all 1σ limits).

On the 3D-HST GOODS fields extremely deep X-ray data are also available, 4Ms in CDF-South (see Xue et al. 2011), and 2Ms in CDF-North (see Alexander et al. 2003), that we use for identifying bright AGNs.

² The Bell et al.(2005) relation properly applies to starbursts of continuous star formation, with recent star-formation timescale of $\sim 10^8$ yr and solar metallicity.

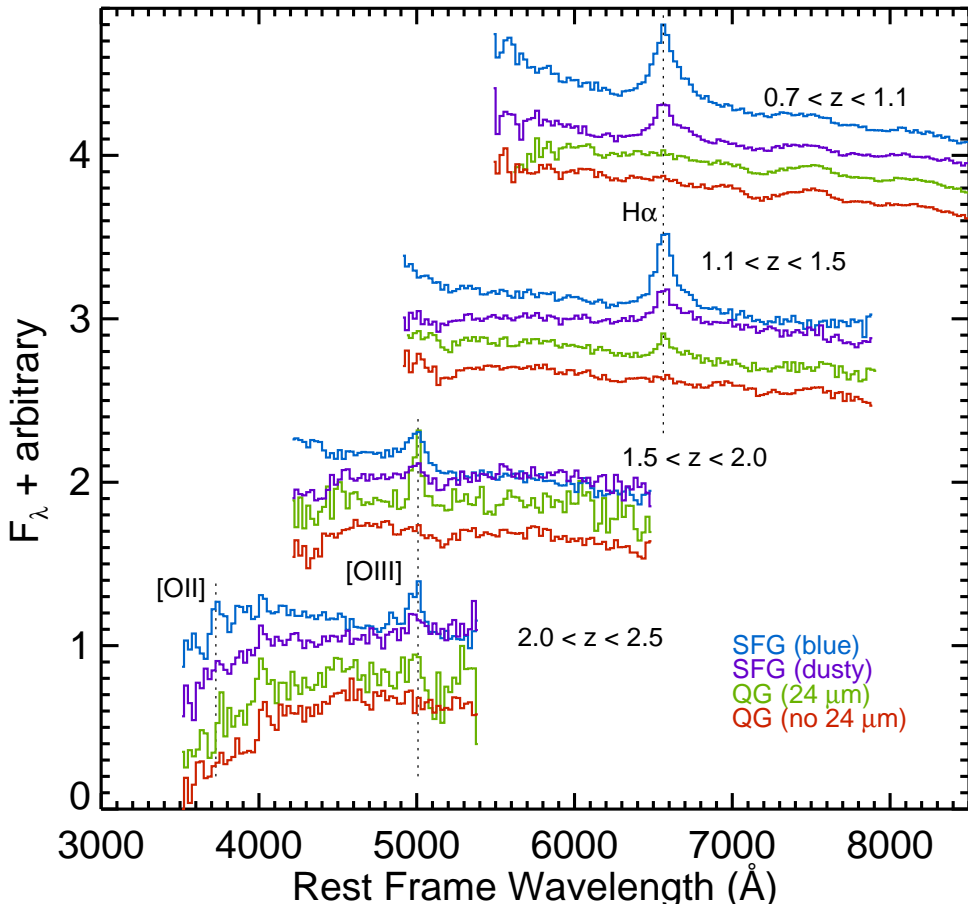


Figure 3.2: Stacked 3D-HST spectra for mass-selected ($\log_{10}(M_*/M_\odot) > 10.3$) galaxies in different redshift bins. In each redshift bin, blue means blue SFGs ($U - V < 1.5$), purple dust-reddened SFGs ($U - V > 1.5$), green QGs with a $24\mu\text{m}$ detection, red QGs without a $24\mu\text{m}$ detection. Vertical dashed lines show the position of $\text{H}\alpha$, [OIII] and [OII].

3.3 Sample selection and motivations of the study

3.3.1 Selection of Quiescent Galaxies

In order to select quiescent galaxies (QGs) we use a color-color technique (Figure 3.1), specifically rest-frame $U - V$ versus rest-frame $V - J$ (hereafter: UVJ diagram). This technique has been widely used to distinguish QGs from SFGs, including the heavily reddened SFGs (Labbé et al. 2005; Wuyts et al. 2007; Williams et al. 2009; Brammer et al. 2009; Whitaker et al. 2010; Patel et al. 2012; Bell et al. 2012; Gobat et al. 2013). QGs are identified using the criteria $(U - V) > 0.8 \times (V - J) + 0.7$, $U - V > 1.3$ and $V - J < 1.5$, as in Whitaker et al. (2012)³. Effectively, this

³We test the stability of the selection by shifting the box by ± 0.05 magnitude, which does not affect the analysis.

selection targets galaxies whose optical and near-IR light is dominated by an old stellar population. We select galaxies more massive than $\log_{10}(M_*/M_\odot) > 10.3$ and divide the sample in five redshift bins, centered on $z = 0.5, 0.9, 1.2, 1.7, 2.2$. The sample is mass complete at $> 97.5\%$ level even at the highest redshift ($z < 2.5$) we consider (Tal et al. 2014). At each redshift the QG sample consists of at least 60 galaxies (Table 3.1).

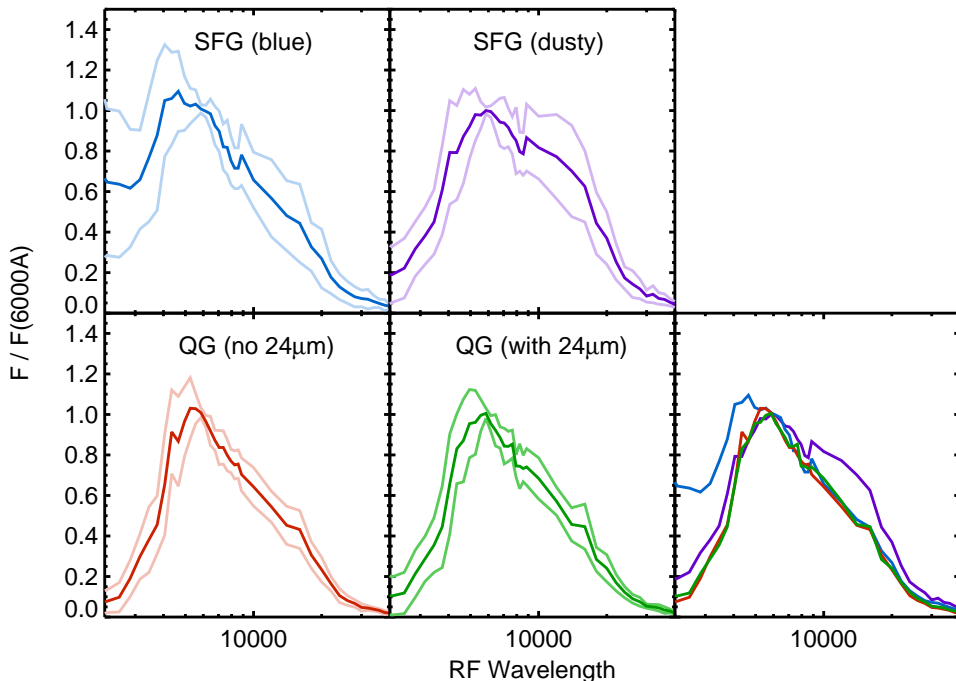


Figure 3.3: Composite SEDs for mass-selected samples ($\log_{10}(M_*/M_\odot) > 10.3$) of star-forming galaxies (divided into blue and dusty) and quiescent galaxies (divided according to the presence of a $24\mu\text{m}$ detection) at redshift $0.3 < z < 2.5$. Light lines indicate the scatter in the stacks. In the bottom-right panel we overplot the four composite SEDs, showing that quiescent galaxies with and without $24\mu\text{m}$ detection have very similar optical and near-IR SED shapes, while star-forming galaxies and dusty star-forming galaxies are clearly distinguishable.

3.3.2 Spectra and SEDs of the sample

In Figure 3.2 we show stacked optical spectra of QGs and SFGs from 3DHST in mass-selected samples ($\log_{10}(M_*/M_\odot) > 10.3$). SFGs are subdivided into blue SFGs ($U - V < 1.5$) and dust-reddened SFGs ($U - V > 1.5$).

QGs are subdivided according to the presence of a MIPS $24\mu\text{m}$ detection. As noted by other authors (e.g. Brammer et al. 2009, Barro et al. 2013), approximately 25% of the optically-selected QGs have a $24\mu\text{m}$ detection, which is in apparent contrast with the red optical colors and the SEDs. We also notice that $24\mu\text{m}$ -detected

QGs do not lie preferentially in any locus of the UVJ diagram (green dots in Figure 3.1).

The spectra in Figure 3.2 clearly show that the UVJ selection is efficient in dividing the two populations; the SFG selection includes the heavily dust-reddened SFGs, that despite red $U - V$ colors, show spectral features ($H\alpha$, D4000) characteristic of SFGs. It is also noteworthy to see that QGs with $24\mu\text{m}$ detections have some $H\alpha$ and [OIII] (cfr. Whitaker et al. 2013), that indicate the presence of low level star formation and/or nuclear activity.

Figure 3.3 shows composite SEDs (following the methodology of Kriek et al. 2011) for SFGs (divided into blue and dusty) and QGs (divided according to the presence of a $24\mu\text{m}$ detection). The SED shapes of star-forming galaxies, dusty star-forming galaxies and quiescent galaxies are clearly different. The rest-frame optical and near-IR SEDs of QGs with and without $24\mu\text{m}$ detection are instead very similar.

3.3.3 SFRs from SED fitting and expectations from gas recycling

We first analyze the sSFR from the SED fits to the UV-optical and near-IR photometry (see Section 2). The values are shown against redshift for the quiescent galaxies in Figure 3.4 (gray dots and black line). The median value is $\text{sSFR} = 1.7 \times 10^{-12} \text{yr}^{-1}$, and the correlation with redshift is weak. These values compare well with those of Ciambur et al (2013), who used a similar method. No significant difference in the SED-derived SFRs is seen if we split the quiescent population between galaxies with and without a $24\mu\text{m}$ detection.

The low sSFRs can be compared to the stellar mass loss from evolved stellar populations (Parriott & Bregmann, 2008; Leitner & Kravtsov, 2010). Green dots in Figure 3.4 represent for the QG sample the sSFR expected from stellar mass loss, assuming that 100% of the gas expelled from old stars is recycled into star formation. Mass loss is computed directly from M_{gas} of the BC03 models at the best fit age of the galaxy, given the best fit τ model (see Section 2, Data). The expected sSFR from gas recycling is $2 - 4 \times 10^{-11} \text{yr}^{-1}$, with a weak redshift dependence. It overpredicts the sSFR from optical and near-IR SED fitting by more than one order of magnitude.

The discrepancy between the two values at each redshift tells us that one of the following options must hold true:

- a mechanism able to prevent the cooling of gas expelled from old stars and therefore the fueling of new star formation exists, *or*
- SFRs from optical and near-IR best fitting are underestimated (and a lot of star formation shows up in the mid-IR).

In the rest of the paper we test the latter possibility measuring SFRs in the mid-IR, in order to prove the former.

3.3.4 How much star formation could be hidden?

We evaluate how much star formation a galaxy can hide (with high dust obscuration), while still retaining red optical-NIR colors. We stack the rest-frame SEDs of

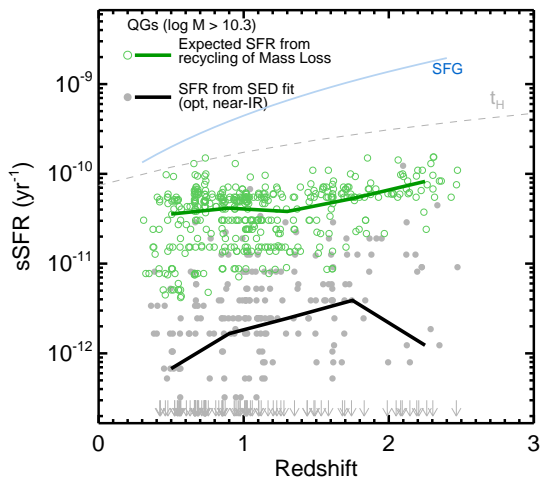


Figure 3.4: sSFR in different redshift bins (gray filled dots) and expected sSFR from recycling of gas from the mass loss of evolved stars (green open dots), as determined from FAST best fits to the SEDs of quiescent galaxies. Solid lines represent mean values in different redshift bins. The mass loss is computed from M_{gas} in BC03 models. It overpredicts the SFR by a factor of 20 at each redshift. sSFRs of star-forming galaxies on the main sequence (cyan) and the Hubble time (dashed gray) are shown as references.

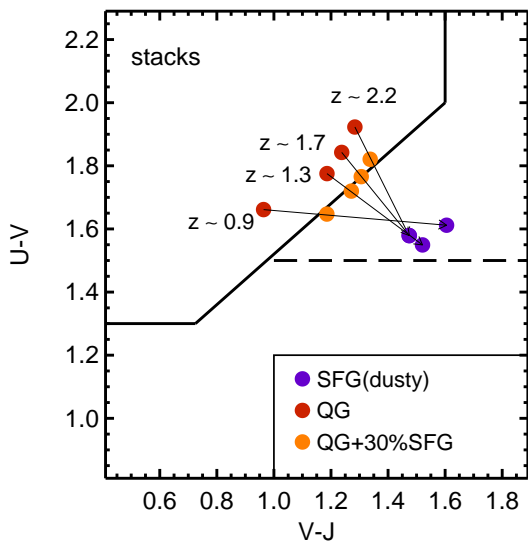


Figure 3.5: The UVJ position of stacks of QGs (red) and dusty SFGs (purple) at different redshifts is shown. Black arrows show the tracks obtained summing a variable fraction (normalized at 6000 \AA , F_{SFG}) of the dusty SFGs SEDs to the QGs SEDs. Orange dots show composite SEDs on the UVJ boundary, corresponding to $F_{SFG} = 30 \%$.

QGs and dusty SFGs in different redshift bins; to each QG SED we add a variable fraction (F_{SFG} , normalized in light at 6000\AA) of the dusty SFG SED. Figure 3.5 shows the position in the UVJ diagram of the QGs stacks (red), the dusty SFGs stacks (purple) and the SED with $F_{\text{SFG}} = 30\%$ (orange), on the UVJ separation border. Adding a 30% dusty SFG SED to our typical QG SED would keep such a galaxy as quiescent under our selection criteria despite the non-negligible contribution of obscured star formation. Since the SFR of the average SFG evolves with redshift, $F_{\text{SFG}} = 30\%$ corresponds to $\text{sSFR} \sim 8 \times 10^{-11} \text{yr}^{-1}$ at $z = 0.5$ and $\text{sSFR} \sim 3 \times 10^{-10} \text{yr}^{-1}$ at $z = 2.2$. This shows that with high dust content, a red (optical and near-IR) galaxy can hide a significant amount of SF. It is therefore necessary to measure SFR from MIR indicators in order to evaluate the SFRs of QGs. There is also a potential for entirely obscured populations with $A_V \gg 5$, which are known to exist at the centers of local dusty star-bursting galaxies (e.g. Arp 220, Sturm et al. 1996).

3.4 Measuring Obscured Star-Formation Rates of Quiescent Galaxies

In this Section we discuss the SFRs determined from the IR emission with the methodology described in Section 2. In Figure 3.6 we plot the relation between stellar mass and SFR for galaxies in the mass-selected sample. As already noticed by various authors using a variety of SFR indicators (e.g. Noeske et al. 2007, Damen et al. 2009, Whitaker et al. 2012), SFRs and masses of SFGs are correlated (light-blue dots), with a scatter of approximately 0.3 dex. The vast majority of the QGs lies in this plane below the ‘star-forming main sequence’. Most of the QGs are undetected in the MIPS $24\mu\text{m}$ image at 3σ (red dots), while some of them (approximately 25 %, Table 3.1) have a $24\mu\text{m}$ detection (green dots), placing them in the Mass-SFR plane between SFGs and the detection limit.

In order to measure the SFRs for QGs, we stack $24\mu\text{m}$ thumbnails. We emphasize that in this step we stack *cleaned* images ($20''$ wide), where neighboring sources identified in the high resolution $F160W$ band have been subtracted with the technique described in the Appendix.

Summing original $24\mu\text{m}$ thumbnails would lead to a stack with a very poorly constrained background, raised by the presence of neighboring objects. Since the goal of this paper is to measure very low SFRs with accuracy, it is fundamental to perform photometry on a stacked image with small uncertainty on the background (as shown in Figure 3.7).

We perform an average-stacking⁴ in different redshift bins, for two samples: all QGs and only non- $24\mu\text{m}$ -detected QGs. Photometry on the stack is performed within an aperture of 6 arcsec diameter, similar to the size of the $24\mu\text{m}$ FWHM. To measure the total $24\mu\text{m}$ flux, we create a MIPS growth curve from several bright, isolated, and unsaturated point sources within each field. These square postage stamps are 20 arcsec wide, and we derive an aperture correction of a factor of 2.57 from $r = 3$ arcsec to $r = 10$ arcsec. To convert to total flux, we include an additional

⁴Using instead median stacks does not modify the conclusions of the paper.

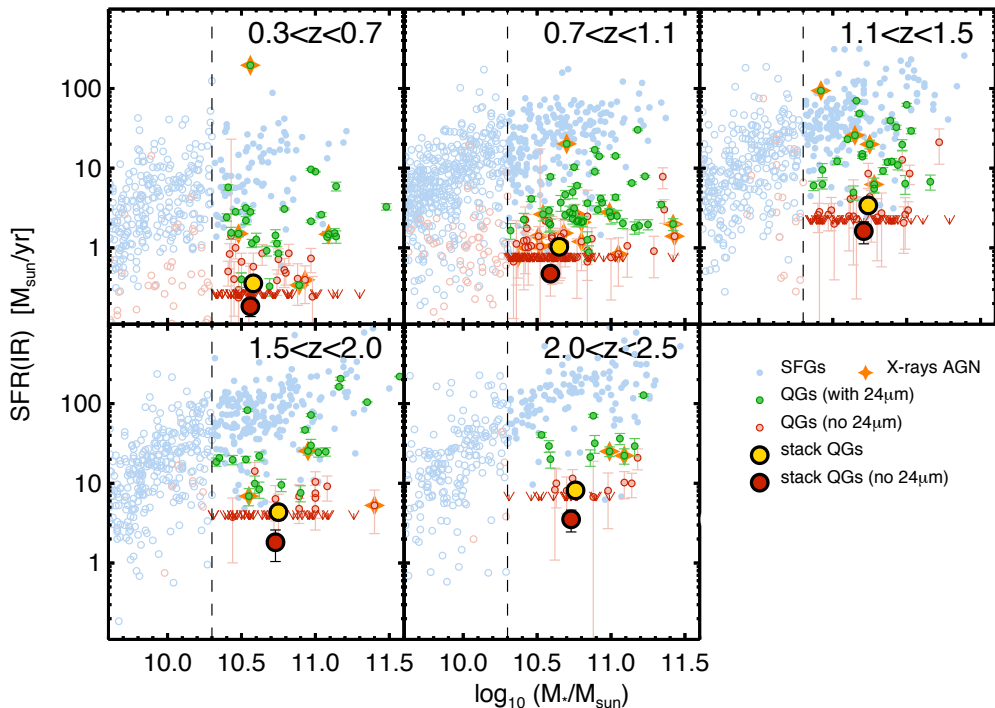


Figure 3.6: Mass-SFR(IR) diagram for galaxies in the 5 redshift bins analyzed in the paper. SFRs are computed assuming that all of the $24\mu\text{m}$ flux is due to reprocessed UV photons from HII regions. Filled symbols denote galaxies with $\log(M_*/M_\odot) > 10.3$. Galaxies are divided in quiescent (QGs) and star-forming (SFGs) according to the box defined in Whitaker et al. (2012): light-blue dots represent SFGs, green dots QGs detected at $24\mu\text{m}$ ($S/N > 3$), red dots QGs not detected at $24\mu\text{m}$. Sources with $S/N < 1$ are shown as arrows at the 1σ level. Orange stars represent X-ray detected QGs in the CDF-S 4Ms catalog and CDF-N 2Ms catalog. The large red dots show the SFRs obtained stacking thumbnails of individually undetected QGs (red), and all QGs (yellow), in mass-selected samples of $\log_{10}(M_*/M_\odot) > 10.3$. Errors on the stacks are computed through bootstrapping of the sample.

aperture correction for the 22% of the flux that falls outside 10 arcsec, derived from the MIPS handbook.⁵

We obtain mostly clear detections with signal-to-noise of 3–5, and fluxes $F_{24\mu\text{m}} = 2 - 5 \mu\text{Jy}$, corresponding to $\text{SFR} \sim 0.5\text{--}5 M_\odot/\text{yr}$. We summarize the measured stacked fluxes in Table 3.1. Errors on the stacks are measured through bootstrapping of the sources. Errors on the stacks are measured through bootstrapping, as follows. Each sample of QGs is resampled 1000 times. We stack the individual $24\mu\text{m}$ images of galaxies belonging to each resampling and perform photometry on the new stacked images. The dispersion of the flux values in the resampled stacks

⁵Since the calibration for MIPS refers to an object with $T = 10000\text{K}$, we color-correct fluxes by dividing them by a factor of 0.967 (MIPS Handbook, Table 4.17). This way flux densities correspond to those of sources with a flat spectrum.

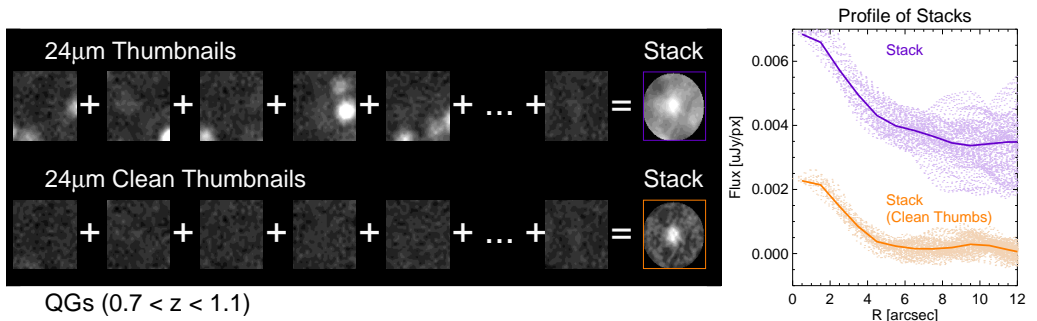


Figure 3.7: Stacking procedure for quiescent galaxies. Left: we show on the top row a random sample of $24\mu\text{m}$ postage stamps ($20''$ wide) from the QGs sample at redshift $0.7 < z < 1.1$ and the resulting stack. The same postage stamps after the neighboring sources have been subtracted (with the PSF-matching technique described in Section 2) are shown in the bottom row, along with the resulting mean stack. Right: Profile of the mean stacks (lines) and individual pixel values (dots) at their distance from the center. The ‘normal’ stack has a high, poorly constrained, background level (artificially raised by neighboring sources).

gives the uncertainty on the flux measurement.

In Figure 3.6 we overplot with large yellow dots the SFR obtained from all QGs (big yellow dots) and non- $24\mu\text{m}$ -detected galaxies (big red dots), representative of the deadest fraction of the galaxy population (this definition of ‘quiescent galaxy’ is the same as in Bell et al. 2012).

Despite the different sample selection (all QGs or just QGs not detected at $24\mu\text{m}$), it is evident that at each redshift the average QGs has a SFR which is at least $\sim 20 - 40$ times lower than the ones on the ‘star-forming sequence’.

In Figure 3.8 (left panel) we show the redshift evolution of SFRs of SFGs and QGs. We plot sSFR since it is more mildly dependent on stellar mass than SFR itself. As noted by previous studies (e.g. Damen et al. 2010, Whitaker et al. 2012, Karim et al. 2012, Fumagalli et al. 2012), the evolution of sSFR in redshift for star-forming galaxies is well fit by a power law $(1+z)^n$ where $n \sim 3 - 4$. At each redshift QGs have a sSFR at least 20 times lower than SFGs. The evolution with redshift of sSFR of QGs seems to resemble the evolution of SFGs. At redshift $z \sim 2$, QGs form 10 times more stars than at redshift $z \sim 0.5$.

In Figure 3.9 we show for our samples the ratio of the average SFR of QGs to the average SFR of SFGs at the same redshift. For quiescent galaxies undetected at $24\mu\text{m}$, the mean value of the ratio is $\langle \text{SFR}_{\text{QG}} \rangle / \langle \text{SFR}_{\text{SFG}} \rangle = 1 / (45 \pm 11)$ while for the entire sample it is $\langle \text{SFR}_{\text{QG}} \rangle / \langle \text{SFR}_{\text{SFG}} \rangle = 1 / (22 \pm 7)$. This confirms that at each redshift quenching of star formation is very efficient.

For QGs the SFRs inferred from the IR emission are generally an order of magnitude larger than those inferred from stellar population modeling (black dashed line in Figure 3.8, left panel). At the highest redshifts they are similar to the values predicted by the recycling of mass loss (green dashed line in Figure 3.8, left panel), while at redshift lower than 1.5 they are significantly lower than those.

3.5 Other possible contributions to L_{IR}

Strictly should be that the IR-inferred SFRs for QGs are upper limits, because of contributions of AGNs, AGB stars and dust heating from old stellar populations to the IR fluxes. We treat each of these components separately in the following Subsections and compare their contributions to L_{IR} with the observed stacked values of L_{IR} in the Discussion Section.

3.5.1 AGN

We evaluate the possible contribution of AGNs by stacking X-ray thumbnails (from the CDF-S 4Ms and CDF-N 2Ms) of the QGs in different redshift bins. Mullaney et al. 2011 demonstrates (Equation 4) the existence of a linear relation between the X-ray luminosity L_{X} and L_{IR} for a sample of local AGNs. After subtracting individually-detected X-ray point sources (marked with orange stars in Figure 3.6), we obtain marginal detections ($2 - 3\sigma$) ranging from $L_{\text{X}} \sim 3.8 \times 10^{40} \text{erg/s}$ ⁶ in the lowest redshift bin to $L_{\text{X}} \sim 2.0 \times 10^{41} \text{erg/s}$ in the highest redshift bin. Converting the obtained X-ray luminosities to IR luminosities with the Mullaney relation, we obtain the gray line in Figure 3.8 (right panel). It lies three orders of magnitude below the observed L_{IR}/M_{\star} ⁷. Olsen et al. (2013) suggest that at redshift $z \sim 2$ most QGs host a low-luminosity AGN, comparing SFR inferred from IR and X-ray. They find, for QG at $1.5 < z < 2.5$ of the same mass of that of our sample, a mean luminosity of $L_{\text{X}} < 2.5 \times 10^{41}$, consistent with our study. Even though most of QGs host a (low-luminosity) AGN, we find that those weak AGN can not account for the MIR emission of the galaxies. Other studies (Donley et al. 2008; Kartaltepe et al. 2010) have also already pointed out that systems with $24\mu\text{m}$ flux dominated by AGNs are not the dominant population at low L_{IR} , such as QGs.

3.5.2 Circumstellar dust

AGB stars are known to evolve embedded in a circumstellar dusty envelope (e.g. Bressan et al. 1998, Lancon & Mouhcine 2002, Piovan et al. 2003). They are the dominant source of the rest-frame K -band luminosity between 0.1 and 1.5 Gyr of age (Kelson & Holden 2010) and significantly contribute to MIR emission, but their dust contribution is not included in classical optical-near infrared SED fitting (Bruzual & Charlot 2003, Maraston 2005). We evaluate the contribution to L_{IR} with the new Charlot & Bruzual 2010 model (CB2010) of an SSP with solar metallicity (private communication). Given galaxy ages from the FAST best fits (see Section 2, and Whitaker et al. 2013, in press), for each galaxy in our QG sample we estimate the observed $24\mu\text{m}$ flux from the CB2010 model and convert it to L_{IR} with the same relation of Wuyts et al.(2008) (Figure 3.8, right panel, orange line).

⁶X-ray luminosities are evaluated assuming a power law spectrum with $\Gamma = 1.8$

⁷A high fraction of Compton-thick AGNs in the sample would originate a higher IR luminosity inferred from X-ray stacks. The percentage of Compton-thick AGNs is however poorly constrained at high redshift (e.g. Akylas et al. 2012).

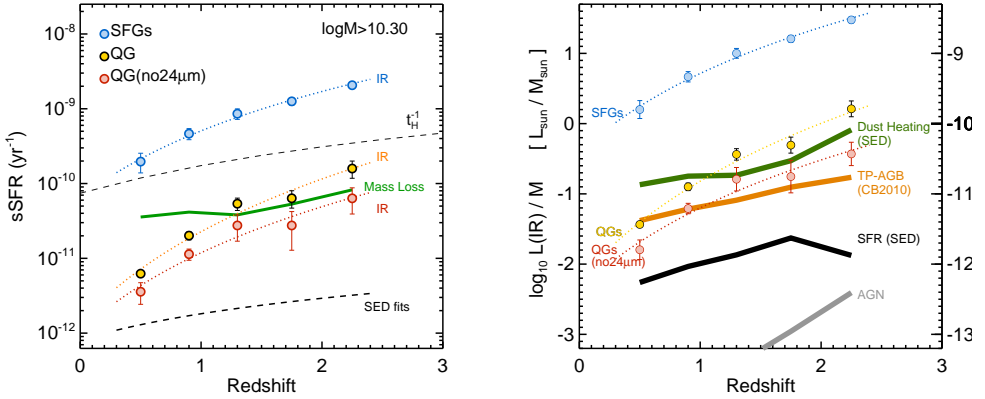


Figure 3.8: Left: Evolution of $sSFR(IR)$ with redshift in a $\log_{10}(M_{\star}/M_{\odot}) > 10.3$ mass-selected sample. light-blue dots indicate mean values for SFGs, while yellow and red points are stacked values of non- $24\mu m$ -detected QGs (red), and all QGs (yellow). At any redshift the average QG has a $sSFR$ 20 times lower than the star-forming sequence. The evolution of $sSFR$ of QGs resembles the one of SFGs. As in Figure 3.4, we indicate with a black line the $sSFR$ from SED fitting and with a green line the expected $sSFR$ from mass loss. At high redshift, the $sSFR(IR)$ of QGs is comparable to the mass-loss. Right: Comparison of observed and modeled L_{IR}/M_{\star} . Values from the stacks of quiescent galaxies are represented by dotted yellow and red lines. SFGs mean values (light-blue) are put as a reference. Expected contributions to L_{IR} for the QG samples from models described in Section 3.5 are drawn with solid lines (gray: AGN, orange: circumstellar dust, black: SFR from best fits, green: cirrus dust heating). Circumstellar dust and cirrus dust can account for most of the observed L_{IR} .

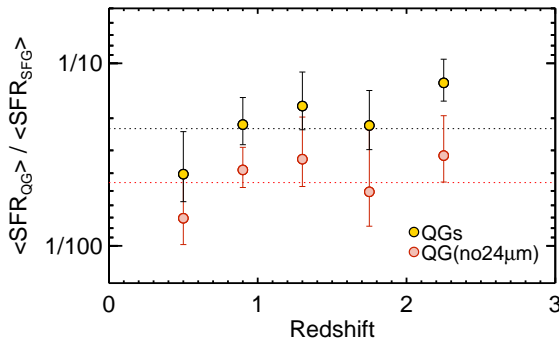


Figure 3.9: Ratio of the average SFR of QGs to the average SFR of SFGs at the same redshift. Red dots represent QGs which are individually undetected at $24\mu m$, while yellow dots represent all QGs. For the two samples, the average ratio is respectively $1/(45 \pm 11)$ and $1/(22 \pm 7)$. These ratios are possibly even lower because for QGs IR inferred SFRs can be significantly contaminated by other sources of dust heating (Section 5).

3.5.3 Cirrus dust

Another possible contribution to L_{IR} is dust heating from old stellar populations. Salim et al. (2009) concludes that, for a sample of $24\mu\text{m}$ -detected galaxies in the DEEP2 survey ($0.2 < z < 1.0$), the bulk of IR emission in red ($NUV - r$) galaxies comes from the heating of diffuse cirrus dust by old stellar populations, rather than by dust heating in star-forming regions. We test if this holds true for the galaxies in our sample as follows. Given the stellar population parameters from the FAST best-fit to the SEDs (age, τ , A_V), we evaluate the luminosity absorbed at $\lambda < 1\mu\text{m}$ by integrating the difference between the unattenuated and the attenuated synthetic SED, and assume it is re-emitted in the IR (see Charlot & Fall 2000, Da Cunha et al. 2008).

We then compare the model L_{IR} predicted by the attenuated SED with the best fit SFR. If L_{IR} originates in dust associated with star-forming regions, we expect the ratio L_{IR}/SFR to be $\sim 9.8 \times 10^9 L_{\odot}/M_{\odot}$ (Bell et al., 2005). Figure 3.10 shows that SFGs (blue) are consistent with this prediction. On the other hand, for QGs (red points) L_{IR} is systematically higher than the expectations from dust heating in star-forming regions. This indicates that in QGs a significant contribution to L_{IR} comes from dust heated by old stellar populations. Inferring SFR from L_{IR} (and therefore from $24\mu\text{m}$ fluxes) overestimates the real SFR of QGs. For each galaxy in the QG sample we estimate the expected L_{IR} luminosity from circumstellar dust, and compute the mean value in different redshift bins (Figure 3.8, right panel, green line).

3.6 Discussion

As we have seen above, various processes other than star formation can contribute to the observed mid-IR flux. We next discuss the impact on the derived SFRs. Moreover, we put constraints on the mass growth of QGs implied by the measured SFRs and on their size growth implied by the stellar mass loss.

In Figure 3.8 (right panel) we show the approximate evolution of L_{IR}/M_{\star} , for data (dashed lines) and models (thick solid lines). We saw earlier that observations of L_{IR} are based on the extrapolation of the single band $24\mu\text{m}$ to $L(\text{IR})$ assuming a template for dust heating by star-forming regions (Section 2). Model predictions estimate that the AGN contribution (gray line) to the L_{IR} is negligible for our sample, while the model expectation for L_{IR} from cirrus dust (green) and circumstellar dust (orange) is comparable to the observed values from stacking. We note that qualitatively both of them decrease towards lower redshift, respectively because of higher A_V and younger stellar ages at higher redshifts (which leads to more absorbed optical light re-emitted in the IR in the younger Universe) and because of the aging of galaxies (which leads to lower contribution of AGB stars in the SED).

If SFRs from SED fitting are correct, their contribution to L_{IR} (black line in Figure 3.8, right panel) would be 1 dex lower than the observed L_{IR} , while dust heated by old stellar population can account for the most of the observed luminosities.

All the measured values from $24\mu\text{m}$ stacks must therefore be considered as upper

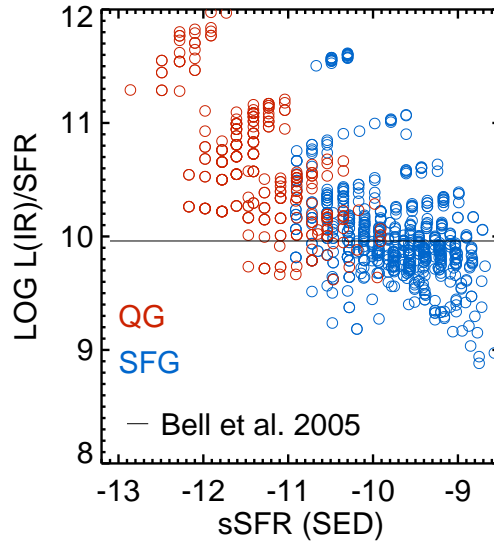


Figure 3.10: Model predictions of L_{IR}/SFR , for QGs (red) and SFGs (blue). L_{IR} is reconstructed assuming that the light absorbed by dust at UV-optical wavelengths is re-emitted in the IR (Section 3.5). For SFGs the ratio is comparable to the Bell et al. (2005) relation (black line), while for QGs L_{IR} are systematically higher than the expectations from SFR, meaning that for QGs most of dust heating comes from old stellar populations.

limits to the SFR. At each redshift, the mean QG has a SFR at least ~ 20 -40 times lower than that of a SFG at the same redshift. These SFRs are significantly higher than estimates based on optical and near-IR model fits (see Section 3 and Ciambur, Kauffman & Wuyts 2013).

In order to evaluate the growth of a QG via star formation we integrate the $\text{sSFR}(\text{IR})$ - z trend of Figure 3.8 (left). This leads to estimate that the *maximum* growth of a QG via star formation is 20% from redshift 2 to 0. Some authors (e.g. van Dokkum et al. 2010, Patel et al. 2012) have inferred that a present-day $10^{11.2} M_{\odot}$ galaxy has to grow 60% of its mass from redshift $z \sim 1.75$ to $z \sim 0$. We show that star formation can not be responsible for the entire stellar growth of QGs, while other mechanisms must be in place, such as minor merging (see, among others, Hopkins 2009). The limit we compute on the mass increase via star formation is more stringent than that computed by Pérez-González et al. (2008), who estimates that massive spheroid-like galaxies may have doubled (at the most) their stellar mass from redshift 2 to 0.

The SFRs expected from stellar mass loss are probably much higher than the real SFRs of QGs, meaning that star formation from mass loss is inefficient. If mass loss from evolved stars is not converted into stars and gas is expelled from the galaxy, an interesting consequence is that the potential of the system becomes shallower and the system expands (Zhao et al. 2002, Murray et al. 2010). In brief (following Damjanov et al., 2009), if a system loses a fraction $\delta M/M$ of its mass in a time

longer than a dynamical timescale, it will expand its radius by a factor of $\delta R/R \sim (1 - \delta M/M)^{-1}$. The modeled mass losses for galaxies in our sample (Figure 3.4) integrated over the redshift range 0 to 2 give $\delta M/M \approx 0.4$, which leads to $\delta R/R \approx 0.6$. The observed size growth of quiescent galaxies from redshift 2 to 0 amounts to a factor of 2-3 (e.g. Williams et al. 2010, Newman et al. 2012, Whitaker et al. 2012), therefore mass loss can not be its unique cause but only one of the concurrent ones (see also Damjanov et al., 2009). We note that the assumed mass loss depends on the absolute ages of galaxies at each redshift, which are very uncertain.

A possible caveat in the study comes from the fact that the 24 μ m-to-L(IR) conversion relies on a single infrared template (Wuyts et al. 2008), while the underlying SED for high-redshift quiescent galaxies is unknown. As explained in Section 2 (Data), measuring the low fluxes of quiescent galaxies at Herschel wavelengths is extremely challenging. Available observationally motivated far-IR SEDs of galaxies at high redshift are based on bright Herschel sources (e.g. Elbaz et al. 2011, Magdis et al. 2014) and refer to galaxies on or above the star-forming main sequence. We evaluate the possible bias introduced by our synthetic template by comparing the L(IR) integrated under the Elbaz et al. 2011 SED for main-sequence galaxies to that inferred from a simulated 24 μ m observation of that SED, at different redshifts. We obtain that at $z > 1.5$ the inferred L(IR) is a factor of 2 higher than the integrated L(IR), while at $z < 1.5$ the bias is lower than 50%.

The possibility that galaxies below the main-sequence have different infrared SED shapes must however be taken into account (see also Utomo et al. 2014, Hayward et al. 2014). We compute the systematic uncertainty on L(IR) arising from the unknown underlying SED as follows. We compare the 24 μ m-to-LIR conversion of Wuyts et al. 2008, obtained by averaging a vast array of infrared templates from Dale & Helou 2002, with those obtained by using each single Dale & Helou 2002 template for different values of the ionization parameter α . The dispersion on the values is 0.3 dex, which we consider the systematic uncertainty on the conversion. We conclude that the possible biases and uncertainties induced by inferring L(IR) from a single band and a single template amount to a factor of 2, and do not affect the conclusions of the paper.

3.7 Conclusions

We select quiescent galaxies at redshift $0.3 < z < 2.5$ in the 3D-HST survey from their rest-frame optical and near-IR colors. Fitting their UV to near-IR photometry with stellar population models, we find very low star-formation rates (sSFR $\sim 10^{-12}\text{yr}^{-1}$). These values are much lower than the stellar mass loss rates predicted by the same models. This suggests that the star formation is either missed because it is dust obscured, or that the gas from stellar mass loss is expelled from the galaxy or prevented from refueling star formation.

We put upper limits on the obscured star-formation rate of quiescent galaxies by stacking 24 μ m images. Including direct 24 μ m detections, we find that $\text{sSFR}(\text{IR}) \leq 10^{-11.9} \times (1+z)^4 \text{yr}^{-1}$. At each redshift the sSFR of quiescent galaxies is ~ 20 -40 times lower than the typical value on the main sequence of star-forming galaxies.

SFRs of quiescent galaxies are possibly even lower than this, because the IR luminosity can also be due to other sources, such as the presence of AGB dust enshrouded stars and dust heating from older stellar populations. Stacks of longer wavelength data (such as from *Herschel*) are necessary for constraining the dust temperature and therefore distinguishing between the different contributions to L_{IR} , however a large sample may be necessary to achieve adequate S/N (e.g. Viero et al. 2013). We show nevertheless that dust heating from old stellar populations can account for most of the observed L_{IR} .

The observed SFR(IR) are therefore upper limits to the real SFR, which are possibly one order of magnitude lower. This means that there must be a mechanism that not only shuts down star formation, but also keeps the galaxy dead for a long period of time, preventing the ejected gas from cooling and forming new stars. If gas from mass-loss is expelled from galaxies, we predict that it is responsible for a growth in stellar radii of 60% from redshift 2 to 0.

We acknowledge funding from ERC grant HIGHZ no. 227749. This work is based on observations taken by the 3D-HST Treasury Program (GO 12177 and 12328) with the NASA/ESA HST, which is operated by the Association of Universities for Research in Astronomy, Inc., under NASA contract NAS5-26555.

Table 3.1: Properties of Stacks

Redshift	N_{QG}	$F(24\mu\text{m})_{\text{QG}}$	$\text{SFR}(\text{IR})_{\text{QG}}$	$N_{\text{QG,no24}\mu\text{m}}$	$F(24\mu\text{m})_{\text{QG,no24}\mu\text{m}}$	$\text{SFR}(\text{IR})_{\text{QG,no24}\mu\text{m}}$
0.3 - 0.7	97	$7.7 \pm 0.5 \mu\text{Jy}$	$0.4 \pm 0.1 M_{\odot}/\text{yr}$	67	$3.9 \pm 1.3 \mu\text{Jy}$	$0.2 \pm 0.1 M_{\odot}/\text{yr}$
0.7 - 1.1	154	$6.6 \pm 0.7 \mu\text{Jy}$	$1.2 \pm 0.1 M_{\odot}/\text{yr}$	108	$4.1 \pm 0.7 \mu\text{Jy}$	$0.5 \pm 0.1 M_{\odot}/\text{yr}$
1.1 - 1.5	84	$9.3 \pm 1.8 \mu\text{Jy}$	$3.7 \pm 0.7 M_{\odot}/\text{yr}$	58	$4.4 \pm 1.8 \mu\text{Jy}$	$1.8 \pm 0.6 M_{\odot}/\text{yr}$
1.5 - 2.0	72	$6.8 \pm 1.8 \mu\text{Jy}$	$4.6 \pm 1.3 M_{\odot}/\text{yr}$	51	$3.0 \pm 1.6 \mu\text{Jy}$	$2.0 \pm 1.0 M_{\odot}/\text{yr}$
2.0 - 2.5	35	$5.7 \pm 1.8 \mu\text{Jy}$	$8.8 \pm 2.2 M_{\odot}/\text{yr}$	25	$3.2 \pm 1.3 \mu\text{Jy}$	$3.8 \pm 1.5 M_{\odot}/\text{yr}$

For different redshift bins: number of galaxies in the quiescent sample (QG) and quiescent sample without 24 μm detection (QG,no24 μm), along with their stacked 24m fluxes, and the implied SFR from IR emission.

3.A Appendix A: Photometry

The MIPS-24 μ m beam has a FWHM of 6 arcsec, therefore confusion and blending effects are unavoidable in deep observations at this resolution. We use a source-fitting algorithm designed to extract photometry from IRAC and MIPS images (see, e.g., Labbé et al. 2006; Wuyts et al. 2007). The information on position and extent of the sources based on the higher resolution *F160W* segmentation map is used to model the lower resolution MIPS-24 μ m images. Local convolution kernels are constructed using bright, isolated, and unsaturated sources in the *F160W* and MIPS-24 μ m, derived by fitting a series of Gaussian-weighted Hermite functions to the Fourier transform of the sources. Each source is extracted separately from the *F160W* image and, under the assumption of negligible morphological K-corrections, convolved to the MIPS-24 μ m resolution using the local kernel coefficients. All sources in each MIPS-24 μ m image are fit simultaneously, with the flux left as the only free parameter. The modeled light of neighboring sources (closer than 10 arcsec) is subtracted, thereby leaving a "clean" MIPS-24 μ m image to perform aperture photometry and stacking of faint sources. The technique is illustrated in Figure A1 and A2, respectively for a bright and a faint source.

3.B Appendix B: Field-to-field variation

The paper is built on data from the GOODS-North and GOODS-South fields. The two fields feature a similar large number of optical-near-IR observations included in the 3D-HST photometric catalog, and data quality in the 3D-HST fields is uniform (see Skelton et al., 2014). The depths of MIPS-24 μ m data are similar in the two fields (Dickinson et al. 2003). We show in Figure B1 the main result of the paper - the evolution of sSFRs of QGs - once the data are stacked separately in the two fields. Differences and errors are consistent with lower statistics.

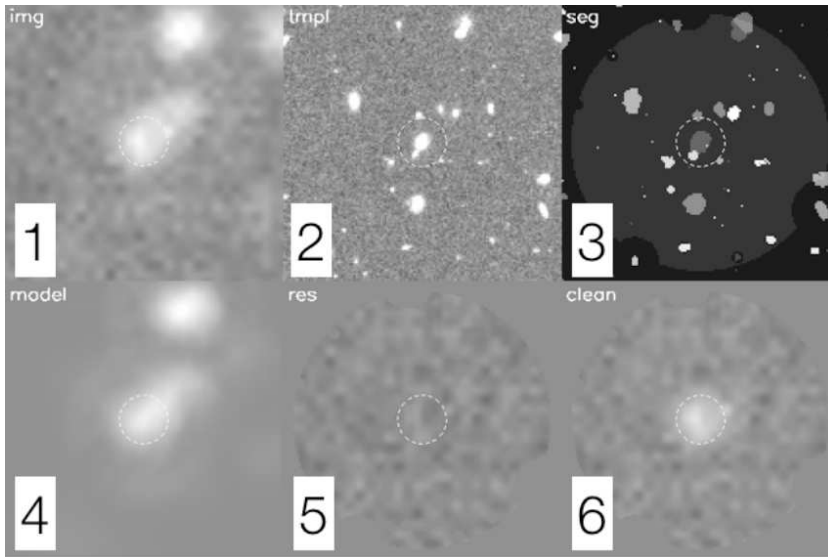


Figure B1: The process of modeling and deblending $24\mu\text{m}$ fluxes for objects identified in the F160W detection image. Panel 1 shows the original $24\mu\text{m}$ cutout for an object in the catalog. Panel 2 and 3 show the matching F160W detection image and segmentation map from SExtractor. The bottom row shows the modeled $24\mu\text{m}$ flux for all objects in the region (Panel 4), the residual image with all modeled fluxes removed (Panel 5), and the flux for the central object alone (Panel 6).

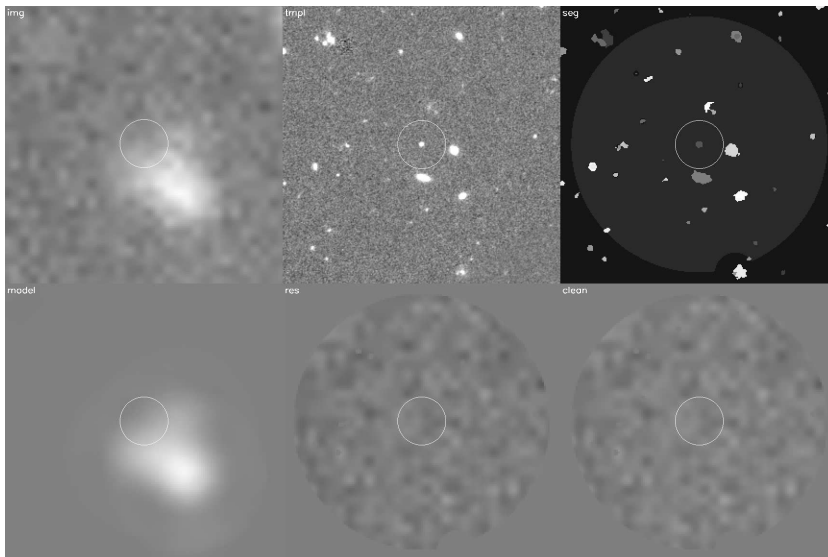


Figure B2: Same as Figure A1, but for a faint object in the catalog.

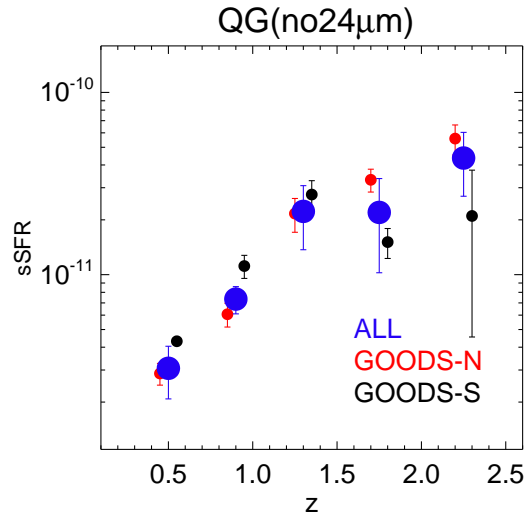


Figure B3: Evolution of sSFR of QGs without an individual 24 μ m detection, for different fields and in the entire sample. Red/black dots are stacked values from GOODS-North/GOODS-South, and large blue dots are values from the combined sample. Errors are computed bootstrapping the sample. Mean redshifts have been shifted of ± 0.05 for clarity. Differences and errors are consistent with lower statistics.

Bibliography

- Akylas, A., Georgakakis, A., Georgantopoulos, I., Brightman, M., & Nandra, K. 2012, *A&A*, 546, A98
- Alexander, D. M., Bauer, F. E., Brandt, W. N., et al. 2003, *AJ*, 126, 539
- Barro, G., Faber, S. M., Pérez-González, P. G., et al. 2013, *ApJ*, 765, 104
- Bell, E. F., Papovich, C., Wolf, C., et al. 2005, *ApJ*, 625, 23
- Bell, E. F., van der Wel, A., Papovich, C., et al. 2012, *ApJ*, 753, 167
- Brammer, G. B., van Dokkum, P. G., & Coppi, P. 2008, *ApJ*, 686, 1503
- Brammer, G. B., Whitaker, K. E., van Dokkum, P. G., et al. 2009, *ApJL*, 706, L173
- Brammer, G. B., Whitaker, K. E., van Dokkum, P. G., et al. 2011, *ApJ*, 739, 24
- Brammer, G., van Dokkum, P., Franx, M., et al. 2012, arXiv:1204.2829
- Parriott, J. R., & Bregman, J. N. 2008, *ApJ*, 681, 1215
- Bressan, A., Granato, G. L., & Silva, L. 1998, *A&A*, 332, 135
- Bruzual, G., & Charlot, S. 2003, *MNRAS*, 344, 1000
- Chabrier, G. 2003, *ApJL*, 586, L133

- Charlot, S., & Fall, S. M. 2000, *ApJ*, 539, 718
- Ciambur, B. C., Kauffmann, G., & Wuyts, S. 2013, *MNRAS*, 432, 2488
- da Cunha, E., Charlot, S., & Elbaz, D. 2008, *MNRAS*, 388, 1595
- Damen, M., Labbé, I., van Dokkum, P. G., et al. 2011, *ApJ*, 727, 1
- Damjanov, I., McCarthy, P. J., Abraham, R. G., et al. 2009, *ApJ*, 695, 101
- Dickinson, M., & GOODS Team 2004, Bulletin of the American Astronomical Society, 36, #163.01
- Donley, J. L., Rieke, G. H., Pérez-González, P. G., & Barro, G. 2008, *ApJ*, 687, 111
- Elbaz, D., Dickinson, M., Hwang, H. S., et al. 2011, *A&A*, 533, A119
- Franx, M., van Dokkum, P. G., Schreiber, N. M. F., et al. 2008, *ApJ*, 688, 770
- Fumagalli, M., Patel, S. G., Franx, M., et al. 2012, *ApJL*, 757, L22
- Gobat, R., Strazzullo, V., Daddi, E., et al. 2013, arXiv:1305.3576
- Hopkins, P. F., Bundy, K., Murray, N., et al. 2009, *MNRAS*, 398, 898
- Ilbert, O., Salvato, M., Le Floch, E., et al. 2010, *ApJ*, 709, 644
- Karim, A., Schinnerer, E., Martínez-Sansigre, A., et al. 2011, *ApJ*, 730, 61
- Kartaltepe, J. S., Sanders, D. B., Le Floch, E., et al. 2010, *ApJ*, 709, 572
- Kauffmann, G., Heckman, T. M., White, S. D. M., et al. 2003, *MNRAS*, 341, 54
- Kelson, D. D., & Holden, B. P. 2010, *ApJL*, 713, L28
- Kennicutt, R. C., Jr. 1998, *ApJ*, 498, 541
- Komatsu, E., Smith, K. M., Dunkley, J., et al. 2011, *ApJS*, 192, 18
- Kriek, M., van Dokkum, P. G., Franx, M., et al. 2006, *ApJL*, 649, L71
- Kriek, M., van Dokkum, P. G., Labbé, I., et al. 2009, *ApJ*, 700, 221
- Kriek, M., van Dokkum, P. G., Whitaker, K. E., et al. 2011, *ApJ*, 743, 168
- Labbé, I., Huang, J., Franx, M., et al. 2005, *ApJL*, 624, L81
- Labbé, I., Bouwens, R., Illingworth, G. D., & Franx, M. 2006, *ApJL*, 649, L67
- Lançon, A., & Mouhcine, M. 2002, *A&A*, 393, 167
- Leitner, S. N., & Kravtsov, A. V. 2011, *ApJ*, 734, 48
- Maraston, C. 2005, *MNRAS*, 362, 799
- Mullaney, J. R., Alexander, D. M., Goulding, A. D., & Hickox, R. C. 2011, *MNRAS*, 414, 1082

- Muzzin, A., van Dokkum, P., Kriek, M., et al. 2010, *ApJ*, 725, 742
- Murray, N., Quataert, E., & Thompson, T. A. 2010, *ApJ*, 709, 191
- Newman, A. B., Ellis, R. S., Bundy, K., & Treu, T. 2012, *ApJ*, 746, 162
- Noeske, K. G., Weiner, B. J., Faber, S. M., et al. 2007, *ApJL*, 660, L43
- Olsen, K. P., Rasmussen, J., Toft, S., & Zirm, A. W. 2013, *ApJ*, 764, 4
- Patel, S. G., Holden, B. P., Kelson, D. D., et al. 2012, *ApJL*, 748, L27
- Pérez-González, P. G., Trujillo, I., Barro, G., et al. 2008, *ApJ*, 687, 50
- Piovan, L., Tantaló, R., & Chiosi, C. 2003, *A&A*, 408, 559
- Rudnick, G., Rix, H.-W., Franx, M., et al. 2003, *ApJ*, 599, 847
- Salim, S., Dickinson, M., Michael Rich, R., et al. 2009, *ApJ*, 700, 161
- Skelton, R. E., Whitaker, K. E., Momcheva, I. G., et al. 2014, arXiv:1403.3689
- Sturm, E., Lutz, D., Genzel, R., et al. 1996, *A&A*, 315, L133
- Taylor, E. N., Franx, M., van Dokkum, P. G., et al. 2009, *ApJS*, 183, 295
- van Dokkum, P. G., Whitaker, K. E., Brammer, G., et al. 2010, *ApJ*, 709, 1018
- Viero, M. P., Moncelsi, L., Quadri, R. F., et al. 2013, arXiv:1304.0446
- Xue, Y. Q., Luo, B., Brandt, W. N., et al. 2011, *ApJS*, 195, 10
- Whitaker, K. E., van Dokkum, P. G., Brammer, G., et al. 2010, *ApJ*, 719, 1715
- Whitaker, K. E., van Dokkum, P. G., Brammer, G., & Franx, M. 2012, *ApJL*, 754, L29
- Whitaker, K. E., van Dokkum, P. G., Brammer, G., et al. 2013, *ApJL*, 770, L39
- Williams, R. J., Quadri, R. F., Franx, M., van Dokkum, P., & Labbé, I. 2009, *ApJ*, 691, 1879
- Wuyts, S., Labbé, I., Franx, M., et al. 2007, *ApJ*, 655, 51
- Wuyts, S., Labbé, I., Schreiber, N. M. F., et al. 2008, *ApJ*, 682, 985
- Wuyts, S., Förster Schreiber, N. M., Lutz, D., et al. 2011, *ApJ*, 738, 106

4

AGES OF MASSIVE GALAXIES AT $0.5 < z < 2.0$ FROM 3D-HST REST-FRAME OPTICAL SPECTROSCOPY

We present low-resolution near-infrared stacked spectra from the 3D-HST survey up to $z = 2.0$ and fit them with commonly used stellar population synthesis models (BC03, FSPS10 and CKC14). The accuracy of the grism redshifts, in combination with stacking techniques, allows the unambiguous detection of many emission and absorption features, and thus a first systematic exploration of the rest-frame optical spectra of galaxies up to $z = 2$. For a quantitative analysis, we select massive galaxies ($\log(M_*/M_\odot) > 10.8$), we divide them into quiescent and star-forming via a rest-frame color-color technique, and we median-stack the samples in 3 redshift bins between $z = 0.5$ and $z = 2.0$. We find that stellar population models fit the observations well at wavelengths below 6500\AA rest-frame, but show systematic residuals at redder wavelengths. The CKC14 model generally provides the best fits (evaluated with a χ^2 statistics) for quiescent galaxies, while BC03 performs the best for star-forming galaxies. The stellar ages of quiescent galaxies implied by the models vary from 4 Gyr at $z \sim 0.75$ to 1.5 Gyr at $z \sim 1.75$. On average the stellar ages are half the age of the Universe at these redshifts. We show that the inferred evolution of ages of quiescent galaxies is in agreement with fundamental plane measurements, assuming an 8 Gyr age for local galaxies. For star-forming galaxies the inferred ages depend strongly on the stellar population model and the shape of the assumed star-formation history. We finally notice that our low-resolution data is not able to constrain the metallicity of galaxies.

Mattia Fumagalli; Marijn Franx; Pieter van Dokkum; Katherine Whitaker; et al.
Submitted to the Astrophysical Journal

4.1 Introduction

In recent years, multi-wavelength surveys at high redshift have revealed a significant evolution of galaxies from redshift $z \sim 2$ to the present epoch. The emerging picture is based on a few key observations. First, the star formation rates (SFRs) of galaxies have declined by a factor of 10 in the last 10 billion years. Different observational techniques agree that this trend is largely independent of mass (Damen et al. 2009, Karim et al. 2011, Fumagalli et al. 2012). This decline is accompanied by the evolution of the mass function, that once split into star-forming and quiescent population reveals a differential behavior for the two categories: while the number of massive star-forming galaxies remains constant or even declines, the number density of massive quiescent galaxies grows by 0.5-1.0 dex from $z \sim 2$ (Muzzin et al. 2013, Ilbert et al. 2013). An immediate consequence is that the quiescent fraction at the massive end becomes increasingly larger at lower redshifts (Bell et al. 2007; Bundy et al. 2006, Brammer et al. 2011). While at lower redshift massive galaxies ($\log(M_*/M_\odot) > 11$) are dominated by a homogenous group of quiescent, red, early-type objects (Djorgovski & Davis 1987; Blanton et al. 2003; Kauffmann et al. 2003a), at redshift $z \sim 1$ the population shows a large diversity of colors, structural parameters and SFRs (Abraham et al. 2004, van Dokkum et al., 2011).

An additional insight into the assembly history of galaxies is given by their stellar population parameters, namely their age and metallicity. In the local universe the light-weighted ages and metallicities (both stellar and gaseous) have been shown to correlate tightly with mass (e.g. Tremonti et al. 2004, Gallazzi et al. 2006). While chemical properties of gas in star-forming objects have been traced up to $z \sim 3$ by emission line studies of Lyman break galaxies (e.g. Erb et al. 2006, Moustakas et al. 2011), studies of stellar population parameters at high redshift have been proven challenging, since they require deep spectroscopy in order to trace the rest-frame continuum. Recent works by Gallazzi et al. 2014 and Choi et al. 2014 push stellar population analysis to redshifts of $z \sim 0.7$, where the absorption lines commonly used for metallicity and age determinations (Balmer lines, Mg, Na, etc) fall at the edge of optical spectrographs. At higher redshifts, the optical rest-frame shifts to the infrared, where observations from the ground are notoriously challenging. Determinations of stellar population parameters at $z > 1.5$ are limited to a few bright galaxies (Kriek et al. 2009, van de Sande et al. 2012, Onodera et al. 2012, Bezanson et al. 2013, Onodera et al. 2014, Mendel et al. 2015) or composite spectra (Whitaker et al. 2013)

In this paper we present observations of galaxies at $0.5 < z < 2.0$ obtained with the low-resolution Wide Field Camera 3 (WFC3) grism onboard Hubble Space Telescope (HST). These spectra cover the observed wavelengths $11000 < \text{\AA} < 16000$, which correspond to the optical rest-frame for the targeted redshift range. We divide galaxies into quiescent and star-forming, stack their spectra in mass selected samples, and fit them with models from commonly used stellar population synthesis (SPS) codes.

The goal of the paper is two-fold. In the first place we test the accuracy of SPS models at the observed redshifts and wavelengths. Second, we determine constraints

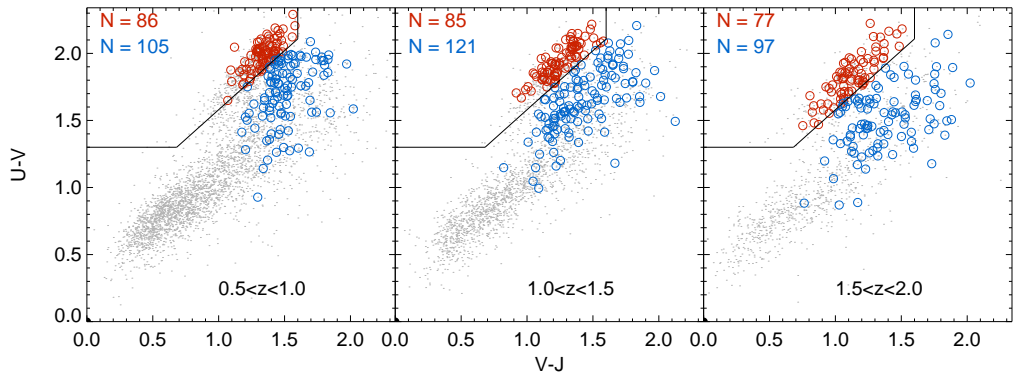


Figure 4.1: The selection of quiescent (red) and star-forming (blue) galaxies more massive than $\log(M_*/M_\odot) > 10.8$ in the UVJ diagram. Grey dots represent all galaxies from 3D-HST in the same redshift bin, including those with a significantly lower mass.

on the stellar ages of galaxies in mass-selected samples, at previously unexplored redshifts.

We note that we apply and test the models in a relatively new regime, both in terms of redshifts and in terms of spectral resolution. Most model tests have been done either at very low spectral resolution (i.e., broad-band and medium-band imaging, with R up to ~ 8), or at moderate to high spectral resolution ($R > \sim 5000$). Here we apply the models to spectra with $R = 50 - 100$, intermediate between imaging and typical ground-based spectroscopy.

4.2 Data

4.2.1 The 3D-HST survey

The 3D-HST program (van Dokkum et al. 2011; Brammer et al. 2012) is a 625 arcmin² survey using HST to obtain low-resolution near-IR spectra for a complete and unbiased sample of thousands of galaxies. (Cycles 18 and 19, PI: van Dokkum). It observes the AEGIS, COSMOS, GOODS-S and UDS fields with the HST/WFC3 G141 grism over 248 orbits, and it incorporates similar, publicly-available data, in the GOODS-N field (GO:11600; PI:Weiner). These fields coincide with the area covered by CANDELS (Grogin et al. 2011; Koekemoer et al. 2011) and have a wealth of publicly available imaging data (U band to $24\mu\text{m}$). The 3D-HST photometric catalogue is described in Skelton et al. (2014), and it constitutes a fundamental step in interpreting the spectra that often contain only a single emission line, if any, by providing a photometric redshift prior to the redshift fitting.

The WFC3 grism spectra have been extracted with a custom pipeline, described in Momcheva et al. (2015, in prep). Redshifts have been measured via the combined photometric and spectroscopic information using a modified version of the EAZY code (Brammer et al. 2008). The precision of redshifts is shown to be $\sigma(\frac{dz}{1+z}) = 0.3\%$

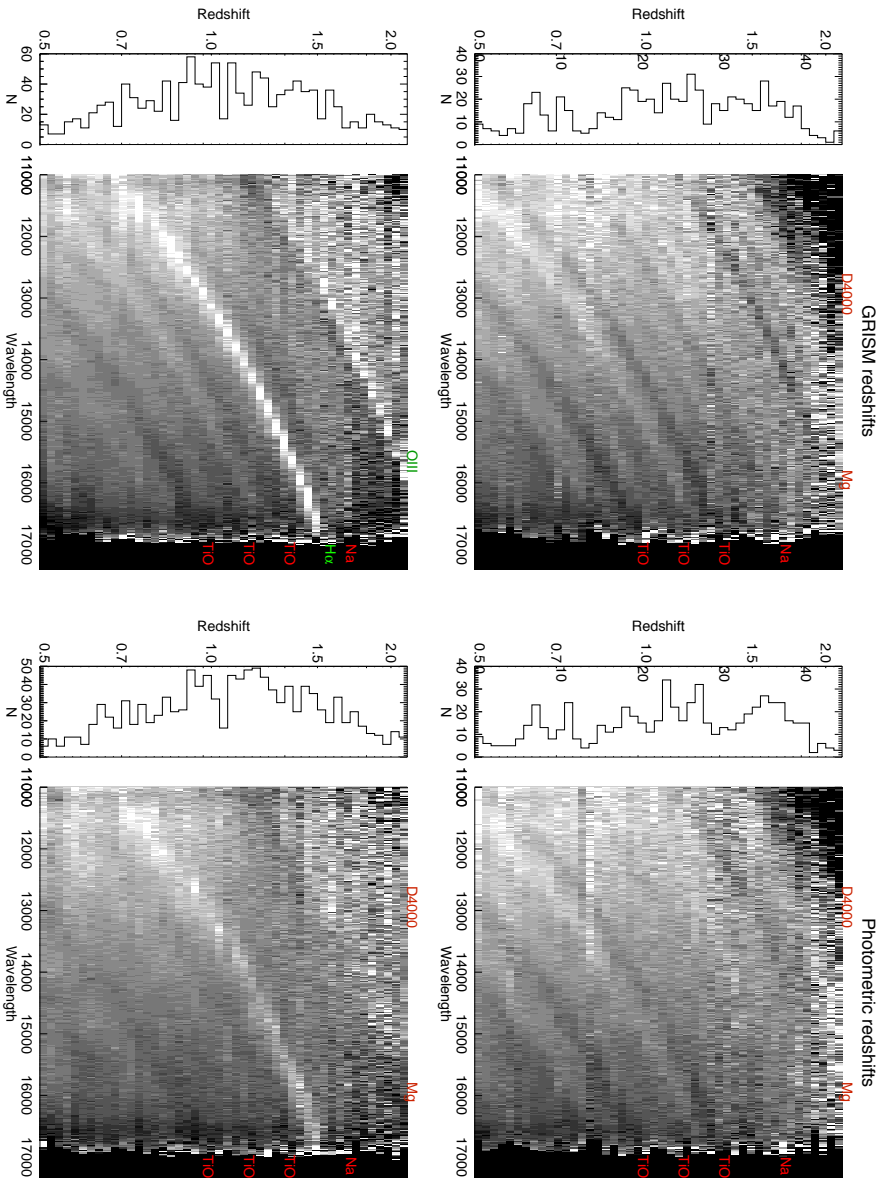


Figure 4.2: Observed spectra of massive ($\log(M_*/M_\odot) > 10.8$) galaxies sorted by redshift, and divided into quiescent (top) and star-forming (bottom). Galaxies are stacked in a narrow, approximately logarithmic redshift spacing. In the left column grism redshifts are used, while in the right column we take advantage of photometric redshifts only: this demonstrates the quality of grism redshifts and the necessity of high precision in redshift evaluation for stacking galaxies together. The most prominent features in emission and absorption are marked respectively in green and red. No significant emission line is seen in the quiescent sample.

(Brammer et al. 2012, Momcheva et al. 2015 in prep; see Kriek et al. 2015 for a comparison based on the new MOSFIRE redshifts from the MOSDEF survey).

Stellar masses have been determined using the FAST code by Kriek et al. (2009), using Bruzual & Charlot (2003) models, and assuming exponentially declining SFHs, solar metallicity, a Chabrier (2003) IMF, and a Calzetti (2000) dust law.

4.2.2 Sample Selection

We separate quiescent galaxies from star-forming galaxies using a color-color technique, specifically rest-frame U-V versus rest-frame V-J (hereafter: UVJ diagram). It has been noted in the past that selecting QGs and SFGs based on a single color is not reliable, because heavily reddened SFGs can be as red as QGs (among others: Williams et al. 2009). Adding information from a second color (V-J) makes it possible to empirically distinguish between galaxies that are red in U-V because of an old stellar population featuring strong Balmer/D4000 breaks (which are relatively blue in V-J) from galaxies that are instead red in U-V because of dust (and therefore are red in V-J too).

The UVJ diagram has been widely used in a variety of high redshift studies (e.g., Wuyts et al. 2007; Williams et al. 2009; Bell et al. 2012; Gobat et al. 2013), it has been shown to correspond closely to the traditional morphological classes of early-type and late-type galaxies up to at least $z \sim 1$ (Patel et al. 2012) and is able to select dead galaxies with low mid-infrared fluxes (Fumagalli et al. 2014).

Effectively, QGs are identified with the criteria $(U - V) > 0.8 \times (V - J) + 0.7$, $U - V > 1.3$ and $V - J < 1.5$ (as in Whitaker et al. 2014). The separating lines are chosen with the main criteria being that they lie roughly between the two modes of the population seen in Figure 4.1.

We select galaxies more massive than $\log(M_*/M_\odot) > 10.8$. In order to achieve a sample of high-quality spectra, we exclude spectra contaminated by neighboring objects for more than 10% of their total flux, with a wavelength coverage lower than 80% of the full regime of 1.1 to 1.7 μm , and with a fraction of bad pixels higher than 10%. All of these quantities are listed in the 3D-HST catalogs. The final sample contains 572 galaxies between redshift 0.5 and 2.0. Figure 4.1 shows the selection of massive galaxies, divided into SFGs and QGs, in three redshift bins, superposed on the entire population of galaxies from 3D-HST at the same redshift.

Figure 4.2 (left) shows all the spectra in the sample in observed wavelength sorted by redshift and divided into QGs (top) and SFGs (bottom). Spectra are stacked in 50 redshift bins with a roughly exponential spacing. We show the number of galaxies in each bin in the histograms on the right. We see emission and absorption lines being shifted in the wavelength direction, and entering and exiting the observed range at different redshifts. For instance, the $H\alpha$ line enters the wavelength range of the WFC3 grism at $z \sim 0.7$ and exits at $z \sim 1.5$.

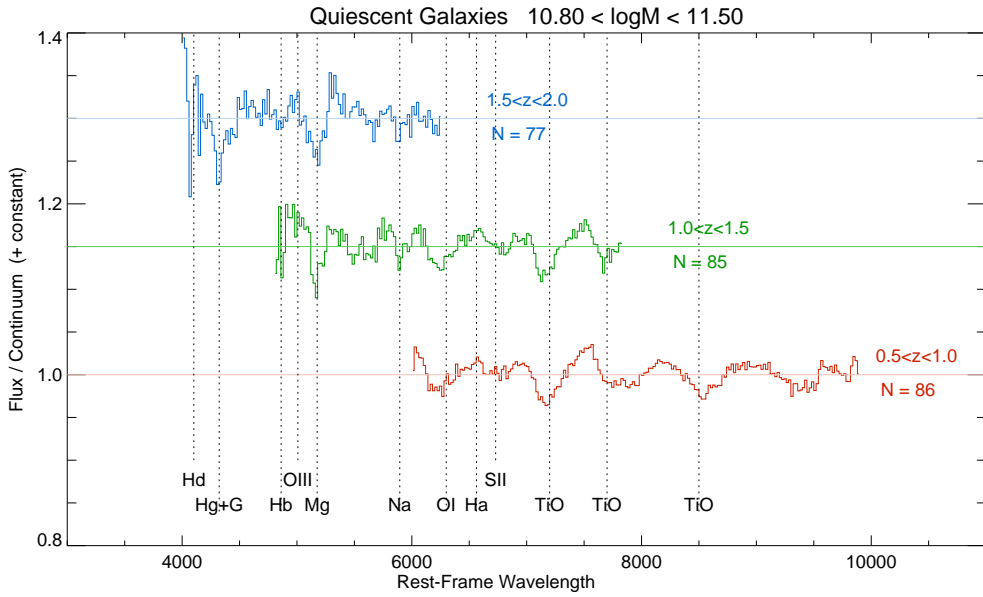


Figure 4.3: Rest-frame stacks of quiescent galaxies with $\log(M_*/M_\odot) > 10.8$, in three redshift bins. The stacks are continuum-subtracted. Many absorption bands are visible, while no obvious emission lines are seen.

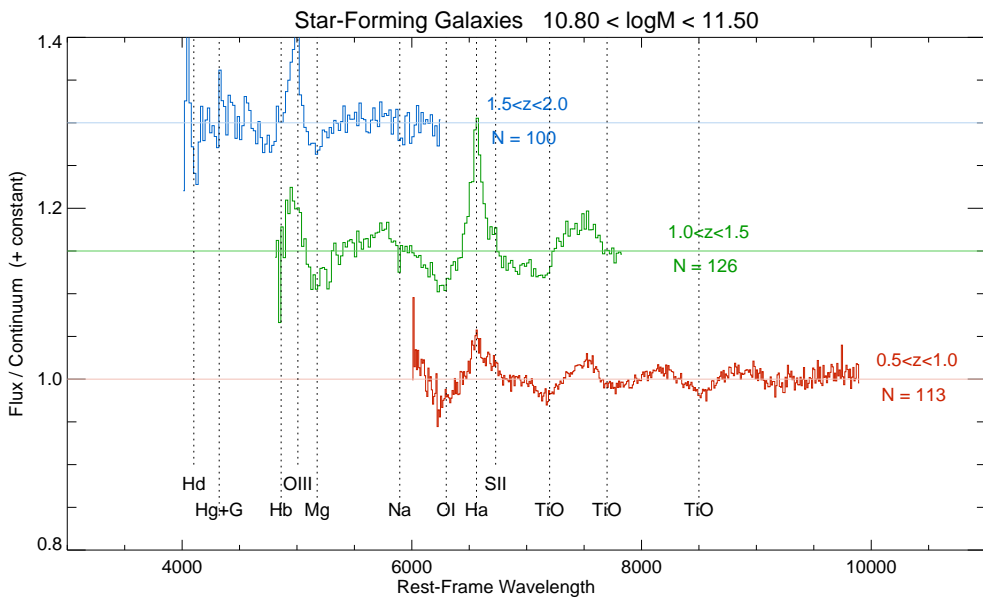


Figure 4.4: Rest-frame stacks of star-forming galaxies with $\log(M_*/M_\odot) > 10.8$, in three redshift bins. The stacks are continuum-subtracted. Both emission and absorption lines are visible.

We notice that the subdivision into SFGs and QGs corresponds well to a selection on the presence of emission lines. In the QGs sample (Figure 4.2, left) there are no obvious emission lines visible, while at different redshifts we observe deep absorption bands (CaII, Mg, Na, TiO). The SFGs sample (Figure 4.2, right) features strong emission lines, such as the already mentioned $H\alpha$, and $H\beta$ and [OIII] at higher redshift. Significantly, some absorption bands are detectable also in the SFG sample.

This experiment proves the quality of 3D-HST grism redshifts. As a comparison, we show in the right column of Figure 4.2 the effect of lower quality redshifts on the stacking procedure, by using photometric redshifts instead of grism redshifts. Even though the photometric redshifts provided in the 3D-HST photometric catalogs (Skelton et al. 2014) reach an excellent absolute deviation from spectroscopic redshifts of just $\sigma = 1 - 2\%$ (depending on the field), this level of precision is not good enough to resolve spectral features. In the right column of Figure 4.2, emission and absorption lines are smoothed across every redshift element; the lines do not line up well in the redshift space and they are almost indistinguishable from the continuum at $z > 1.5$. This experiment demonstrates that stacking grism spectra requires the sub-percent precision in redshift achieved with the 3D-HST z_{grism} .

4.3 Methods

4.3.1 Stacking

In individual galaxies in our sample, spectral features are often too weak to be used for reliable measurements of stellar population parameters. We therefore achieve the necessary signal-to-noise ratio by stacking spectra in 3 redshift bins, and in the two populations of SFGs and QGs, as follows. We shift the spectra to rest-frame and fit the continuum in each spectrum with a third order polynomial. In this process we mask regions around known strong emission lines. We normalize the spectra by dividing them by the best-fit polynomial. We next determine the median flux of the normalized rest-frame spectra in a grid of 20\AA . Errors on the stacks are evaluated via bootstrapping: we perform 100 realizations of each sample by drawing random galaxies from the original sample (repetitions are possible) and we perform the stacking analysis on each resampling. The uncertainty in the flux measurement of each wavelength bin is given by the dispersion of the flux values in the resampled stacks.

The composite spectra are shown in Figure 4.3 (for QGs) and Figure 4.4 (for SFGs). Each individual stack is made from the sum of at least 75 galaxies. As the observations cover a constant range of observed wavelength ($11000\text{\AA} < \lambda < 16000\text{\AA}$), we probe different rest-frame wavelength regimes at different redshifts. The strongest features are the emission lines of $H\alpha$ and [OIII]($\lambda=5007\text{\AA}$) with a peak strength of 15% over the normalized continuum. The absorption lines have depths of 5% or less. The features are weak due to the limited resolution of the spectra.

4.3.2 Model fitting

We compare the stacked spectra with predictions from stellar-population synthesis models (SPS hereafter). Our goal is to test whether different SPS codes can reproduce the absorption line properties of high redshift galaxies, and to infer stellar ages for these galaxies. We use models from Bruzual & Charlot (2003, BC03), Conroy & Gunn (2010, FSPS10), and Conroy et al. (in prep, CKC14)

We use the most standard settings for each SPS code. The BC03 models are based on the Padova stellar evolution tracks and isochrones (Bertelli et al. 1994); they use the STELIB empirical stellar library (Le Borgne et al. 2003) for wavelengths between $3200\text{\AA} < \lambda < 9500\text{\AA}$ and the BaSeL library of theoretical spectra elsewhere.

The FSPS10 models are based on a more updated version of the Padova stellar evolution tracks and isochrones (Marigo et al. 2008); they use the MiLeS empirical stellar library for wavelengths between $3500\text{\AA} < \lambda < 7500\text{\AA}$ and the BaSeL library of theoretical spectra elsewhere.

We have also considered a new, high resolution theoretical spectral library (CKC14, Conroy et al. in prep). This library is based on the Kurucz suite stellar atmosphere and spectral synthesis routes (ATLAS12 and SYNTHE) and the latest set of atomic and molecular line lists. The line lists include both lab and predicted lines, the latter being particularly important for accurately modeling the broadband SED shape. The grid was computed assuming the Asplund (2009) solar abundance scale and a constant microturbulent velocity of 2 km/s.

For each observed stack, we perform a least-squares minimization using the three different models, to find the best-fit age of the stack. In order to compare the high resolution models with the low resolution stacks, we need to downgrade the models to 3D-HST resolution. The dispersion of the G141 grism is $46\text{\AA}/\text{pixel}$ ($R \sim 130$ in the raw data) with a raw pixel scale of 0.12 arcsec, sampled with 0.06 arcsec pixels; as the spectra have high spatial resolution and low spectral resolution (see Brammer et al. 2012), the line width almost exclusively reflects the size of the galaxy in the dispersion direction (Nelson et al. 2012, 2013). We simulate the expected morphological broadening by convolving the high-resolution model spectra with the object morphology in the H_{F140W} continuum image collapsed in the spatial direction. Model spectra for each galaxy in the sample are continuum-divided and stacked with the same procedure we use for observed spectra. In the fitting of models to data, we allow an additional 3rd order polynomial continuum component with free parameters.

In summary, for each sample of galaxies, we create mock 3D-HST stacks based on three stellar population models (BC03, FSPS10, CKC14) with three different star-formation histories (single stellar burst, constant star formation, and an exponentially declining model with $\tau = 1$ Gyr), with a spacing in ages of 0.1 Gyr.

Our choice of performing the stacking and the fitting analysis on continuum-divided spectra is motivated by the goal of measuring ages of galaxies without being influenced by the slope of the continuum, which is degenerate in dust and age. Aging stellar populations have redder broadband colors, however dust reddening has a similar effect. For instance, the difference in $g - r$ color corresponding to 1

Gyr of passive aging within the BC03 models, can also be caused by 0.5 mag of dust reddening following the Calzetti et al. (2000) dust law.

In this study we do not treat galaxies hosting an active galactic nucleus (AGN) separately. We test the influence of AGNs by selecting all sources falling in the IRAC color-color selection presented in Donley et al. (2012). The IRAC selected AGNs count for less than 5% of each sample of QGs/SFGs at different redshifts. The conclusions of the paper do not change when these sources are removed from the stacks.

4.4 Quiescent Galaxies

We fit the stacks of QGs with SSPs from three SPS models (BC03, FSPS10, CKC14) assuming stellar metallicity and a Chabrier IMF. In this section, we will discuss separately the quality of the fits for different SPS models, and the stellar ages determined from the best fits.

4.4.1 Quality of fits

Figure 4.5 shows for each of the models (BC03, FSPS10, CKC14) the best fits to the QG stack for the lower redshift bin ($0.5 < z < 1.0$). The grey shaded area represents the area around $H\alpha$, masked in the fitting. With BC03 (Figure 4.5, red) the best fit

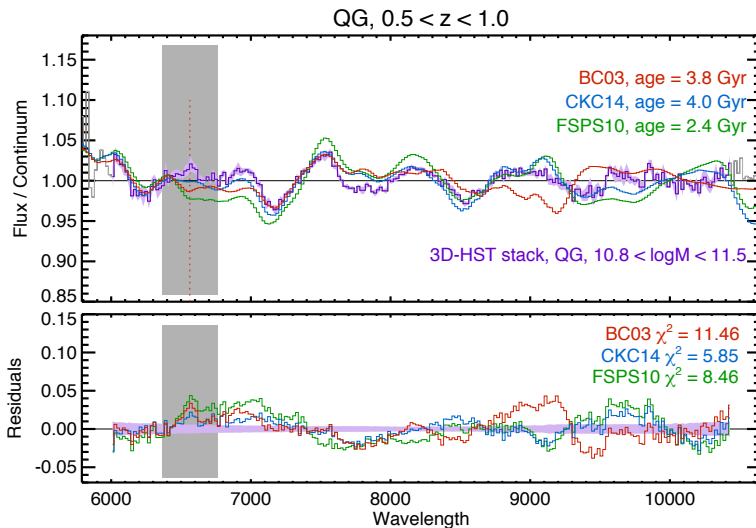


Figure 4.5: Best fits to the stack of quiescent galaxies at $0.5 < z < 1.0$, $\log(M_*/M_\odot) > 10.8$ (purple), with BC03 (red), FSPS10 (green), and CKC14 (blue) SSPs. Errors on stacks are computed through bootstrapping on the sample. The grey area represents the wavelength region around $H\alpha$ masked in the fitting process. A comparison of residuals from different models is shown in the bottom panel. The CKC14 models provide the lowest χ^2 ; its best-fit age is 4.0 Gyr.

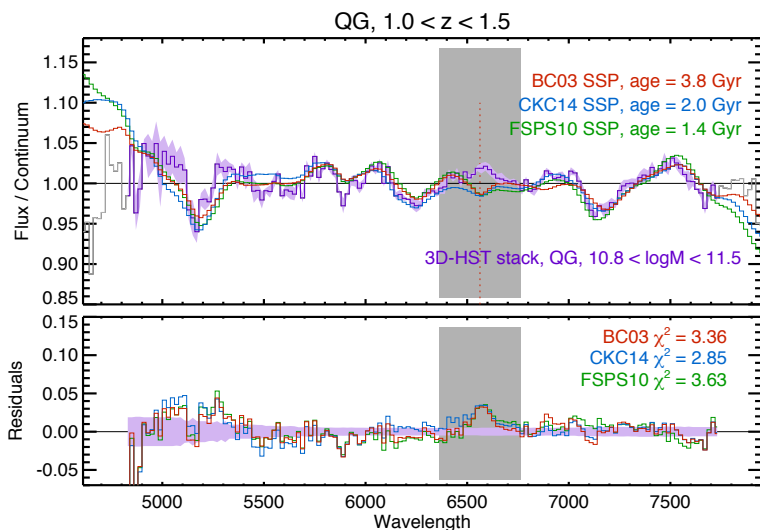


Figure 4.6: Best fits to the stack of quiescent galaxies at $1.0 < z < 1.5$, $\log(M_*/M_\odot) > 10.8$, with the same color coding as Figure 4.5. The χ^2 of different models are comparable. The age determinations span a wide range from 1.4 to 3.8 Gyr, according to the model in use.

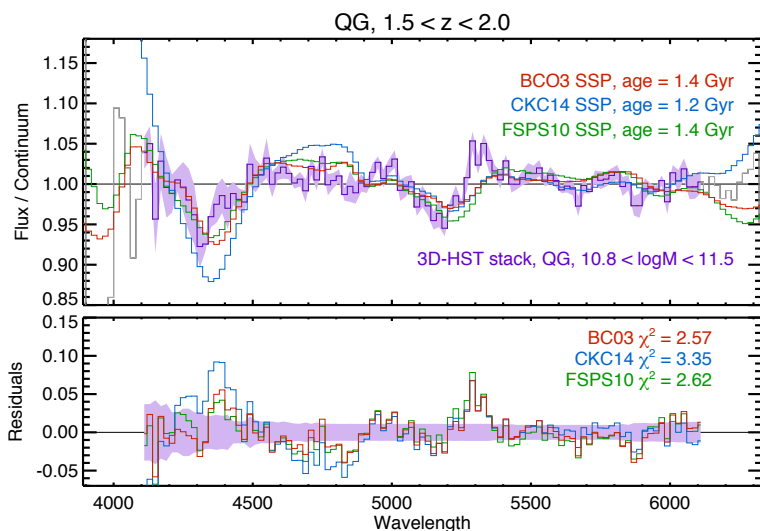


Figure 4.7: Best fits to the stack of quiescent galaxies at $1.5 < z < 2.0$, $\log(M_*/M_\odot) > 10.8$, with the same color coding as Figure 4.5. A comparison of residuals from different models is shown in the bottom panel. Residuals from different models are comparable, and the age determination converges to values of 1.2-1.4 Gyr.

is very poor at wavelengths higher than 7500 \AA , as shown by the residuals in the lower panel. Moreover, the χ^2_{red} value of the best fit is high (11.46). Using FSPS10 (green), the best fit also has significant ($> 3\%$) residuals at the reddest wavelengths ($> 8000 \text{ \AA}$) and around the $> 7000 \text{ \AA}$ regime, where the first TiO band lies. The χ^2_{red}

value of the best fit is still high (8.5). Finally, using the latest CKC14 models (Figure 4.5, bottom left) the best fit converges with a lower $\chi_{red}^2 = 5.8$, and residuals are below 2% consistently over the entire wavelength range. We compare residuals from different SPS models (data-model) in the bottom panel of Figure 4.5. All best-fits have positive residuals in the 7000Å region (up to 4% for FSPS10), underestimating the fluxes at those wavelengths. At wavelengths higher than 8000Å the BC03 models have positive residuals, while FSPS10/CKC14 have negative ones.

Moving to higher redshifts, the quality of fits with different SPS models is comparable. In the intermediate ($1.0 < z < 1.5$, Figure 4.6) and in the high redshift bin ($1.5 < z < 2.0$, Figure 4.7) we examine, all χ_{red}^2 range from 2.8 to 3.3. Residuals in these redshift bins are comparable among different models, and tend to be smaller than a few percent. We evaluate residuals corresponding to the H α line in quiescent galaxies in Section 4.6.3.

4.4.2 Determination of Ages

The stellar ages of quiescent galaxies implied by the best-fit models vary according to the used SSP. In order to evaluate the uncertainty of the age measurement we bootstrap the sample 100 times and repeat the fitting analysis on the bootstrapped realizations of the stack.

At the lowest redshift bin ($0.5 < z < 1.0$, Figure 4.5) we obtain a stellar age of 3.8 ± 0.6 Gyr with BC03, a younger age (2.4 ± 0.4 Gyr) with FSPS10 and again 4.0 ± 0.2 Gyr with CKC14 (which is the model with the lowest residuals). A similar wide range of age determinations is obtained for the intermediate redshift bin (Figure 4.6) ranging from 1.4 ± 0.1 Gyr for FSPS10, to 2.0 ± 0.3 Gyr for CKC14 to 3.8 ± 0.8 Gyr for BC03.

In the highest redshift bin ($1.5 < z < 2.0$, Figure 4.7) all the age determinations are between 1.2 and 1.4 Gyr. This value is consistent with Whitaker et al. (2013),

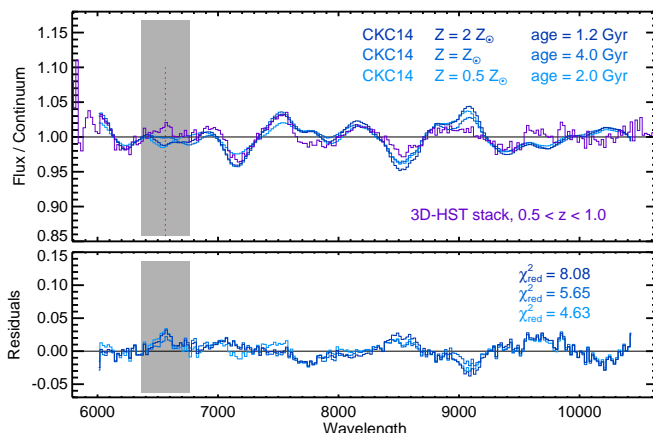


Figure 4.8: Best fits to the stack of quiescent galaxies at $0.5 < z < 1.0$, $\log(M_*/M_\odot) > 10.8$, with the CKC14 models and varying metallicity. A comparison of residuals from different models is shown in the bottom panel.

who studied a sample of galaxies at slightly different masses and redshifts ($10.3 < \log(M_*/M_\odot) < 11.5$, $1.4 < z < 2.2$) obtaining an age of 1.25 Gyr computed with the Vazdekis models. We also agree with Mendel et al. (2015), who investigate the stellar population of 25 massive galaxies with VLT-KMOS, deriving a mean age of $1.08^{+0.13}_{-0.08}$ Gyr.

Our study relies on the assumption that QGs already have a solar metallicity at high redshift. This assumption is supported by the study of Gallazzi et al. (2014), who studied 40 quiescent galaxies at $0.65 < z < 0.75$ with IMACS spectra, obtaining a mass-metallicity relation consistent with that at $z = 0$ from SDSS. We explore the effect of changing metallicity in Figure 4.8 on the stack with the highest signal-to-noise ratio. We use the stellar population model that gave the lowest χ^2 with the standard solar metallicity (CKC14), and vary the metallicity to twice solar and half solar. The best fit is not significantly improved in either case and both the stellar ages are lower than in the solar case. A more accurate determination of the metallicity with higher resolution spectra is needed to measure ages more accurately.

4.5 Star Forming Galaxies

We fit SFGs with the same set of models (BC03, FSPS10, CKC14) with two different star formation histories: a model with constant star formation (CSF), and one with an exponentially declining SFR in the form of $SFR(t) \sim \exp(-t/\tau)$, with $\tau = 1\text{Gyr}$.

4.5.1 Quality of fits

Figure 4.9 summarizes the best fits to the SFG sample at $0.5 < z < 1.0$ obtained with these combinations of models, letting the age t vary. We again mask a 400\AA wide region around $H\alpha$ in the fit. According to the χ^2 statistics, the models assuming an

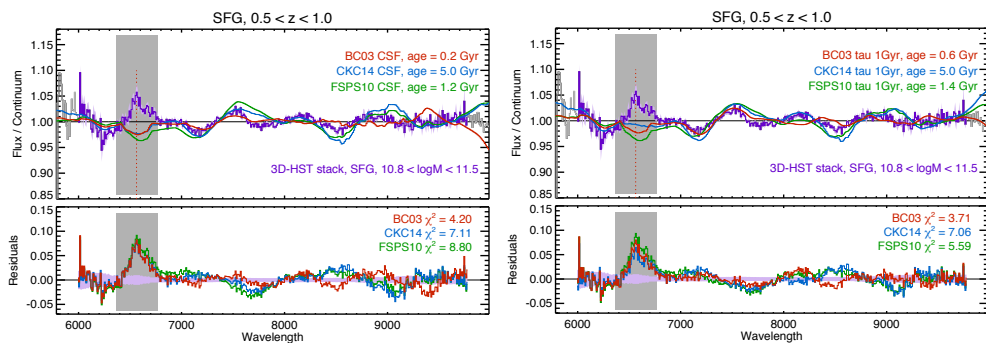


Figure 4.9: Best fits to the stack of star-forming galaxies at $0.5 < z < 1.0$, $\log(M_*/M_\odot) > 10.8$, with BC03 (red), FSPS10 (green) and CKC14 (blue) models. The grey area represents the wavelength region around $H\alpha$ masked in the fitting process. On the left models with a constant star formation rate are used; on the right, exponentially declining models with $\tau = 1\text{Gyr}$. BC03 models provide the best fits, according to a χ^2 statistic. Best-fit ages vary significantly among SPS models and assumed SFHs.

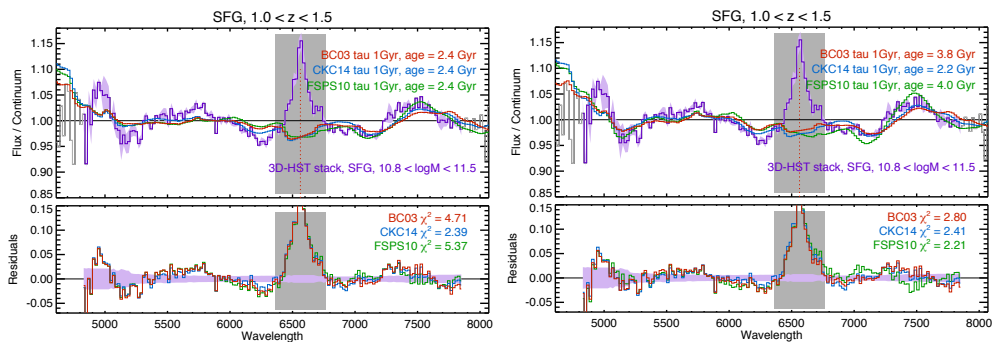


Figure 4.10: Best fits to the stack of star-forming galaxies at $1.0 < z < 1.5$, $\log(M_*/M_\odot) > 10.8$, with BC03 (red), FSPS10 (green) and CKC14 (blue) models. The grey area represents the wavelength region around [OIII] masked in the fitting process. On the left models with a constant star formation rate are used; on the right, exponentially declining models with $\tau = 1\text{Gyr}$. Best fit ages vary from 2 to 4 Gyr.

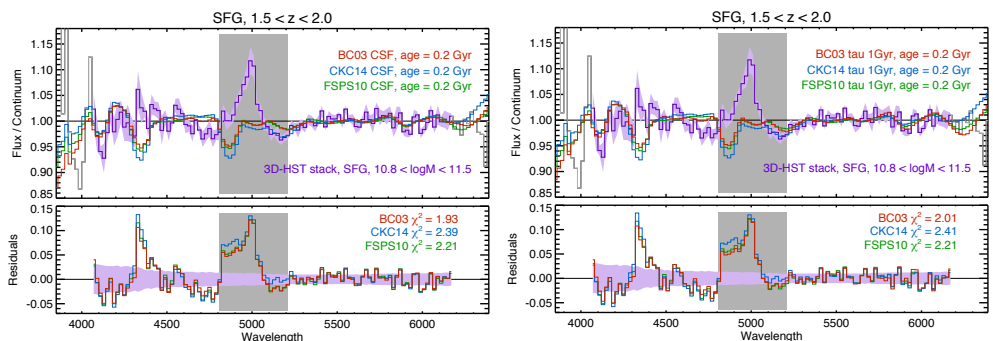


Figure 4.11: Best fits to the stack of star-forming galaxies at $1.5 < z < 2.0$, $\log(M_*/M_\odot) > 10.8$, with BC03 (red), FSPS10 (green) and CKC14 (blue) models. The grey area represents the wavelength region around [OIII] masked in the fitting process. On the left models with a constant star formation rate are used; on the right, exponentially declining models with $\tau = 1\text{Gyr}$. Different SPS models have similar residuals and converge to very young ages.

exponentially declining SFH provide marginally better fits than models assuming a CSF.

Figures 4.10 and 4.11 show the best fits to the SFG samples at $1.0 < z < 1.5$ and $1.5 < z < 2.0$ obtained with the same combination of models. We mask 400Å wide regions around the expected strongest emission lines ([OIII], H α). In the highest redshift stack, we see the biggest residual corresponding to the wavelength of the H γ line ($\lambda = 4341\text{Å}$). For these redshifts, FSPS10 and CKC14 model have a lower best-fit χ^2 than that of BC03. However the models fit almost equally well.

Star-forming galaxies of these masses are in fact known to follow declining star-formation histories at redshifts lower than 1.5 (e.g. Pacifici et al. 2012). As in the case of QGs, different models have qualitatively and quantitatively different residuals. In this case however BC03 is the model with the smallest residuals, especially at the longest wavelengths ($> 8500\text{Å}$).

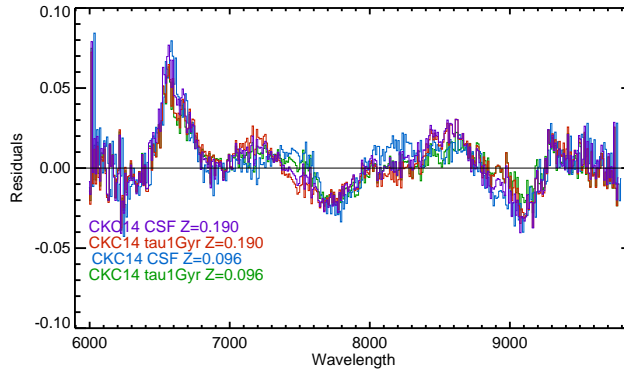


Figure 4.12: For star-forming galaxies at redshift $0.5 < z < 1.0$, we compare residuals to the best-fits obtained by varying metallicity and star formation history. The shape of residuals changes less than by changing the assumed stellar population model (compare with Figure 4.9). The maximum difference in the χ^2 statistics for best fits with varying metallicity is $\Delta\chi^2 = 0.2$, negligible in comparison to the difference obtained by varying the stellar population model ($\Delta\chi^2 = 5$).

The effect of varying metallicity is explored in Figure 4.12 and compared to that of varying stellar population models. We perform this test on SFGs at the lowest redshift bin ($0.5 < z < 1.0$), where the signal-to-noise ratio is high. Figure 4.12 shows a comparison between residuals from best-fit CKC14 models with solar metallicity models ($Z=0.190$) and models with half of the solar metallicity ($Z=0.096$), for a 1 Gyr τ model SFH, and a Constant SFR. We notice that in this case residuals do not vary significantly. We conclude that the difference between different SPS models is greater than that obtained by using the same SPS code, with different metallicities and/or SFHs.

4.5.2 Determination of Ages

For star-forming galaxies at the lowest redshift we examine ($0.5 < z < 1.0$, Figure 4.9), the overall best-fit ($\chi^2_{red} = 3.71$) is obtained with a young (0.6 Gyr of age) stellar population with the BC03 τ model. We also obtain a young age (0.2 Gyr) when assuming a constant star formation history for the same stellar population model. The age determinations from FSPS10 and CKC14 indicate instead an older age, from 1 to 5 Gyr (Figure 4.9). We notice that for star-forming galaxies we cannot exclude any particular age range, since the stellar ages inferred from different models vary greatly.

At intermediate redshift ($1.0 < z < 1.5$, Figure 4.10), we obtain ages around 2-3 Gyrs with different models (the typical error on each inferred age for star-forming galaxies is 1 Gyr). At the highest redshifts ($1.5 < z < 2.0$, Figure 4.11), all best-fits (with different stellar population models and different star formation histories) converge to the lowest age value.

For galaxies with active star formation, the intrinsic strength of features does not

vary significantly with time since the spectra are dominated by light from young stars that been constantly forming. With the current signal-to-noise, we therefore cannot draw any conclusion on the ages of SFGs at the redshift under consideration.

4.6 Discussion

4.6.1 Differences among SPSs

In order to investigate the origin of the qualitative difference in the best fits described in Section 4.4, we compare model spectra from different SPS codes. We show model SSPs from the BC03, FSPS10 and CKC14 codes in Figure 4.13, for different ages. The strengths of the absorption lines vary among models, for every age. We notice in particular that at wavelengths higher than 7500\AA different models predict different absorption bands at different wavelengths. We quantify the spread in the models at different wavelengths by computing the mean difference between every possible combination of models at the same age (Figure 4.13, bottom). This value is lower than 1% at wavelength between $\sim 4500\text{\AA}$ and 6500\AA , and is larger otherwise. In particular the region with wavelengths greater than 8000\AA has a large discrepancy between BC03 on one side, and FSPS10 and CKC14 on the other. This explains why determinations of ages from 3D-HST at higher redshifts are more stable between different models than those at lower redshift. For our lowest redshift sample ($0.5 < z < 1.0$) we observe the region of the spectrum where discrepancies among models are the largest, while at high redshift we observe rest-frame wavelengths where models are more similar to each others.

4.6.2 Evolution of Ages

We investigate the evolution of ages of quiescent galaxies in a mass limited sample. In Fig. 4.14 (left) we show the ages obtained by fitting 3D-HST stacks with different stellar population synthesis models. Even though the model dependent spread in ages is large, we observe that QGs are younger at higher redshift and that, at each redshift, QGs are not maximally old; instead their age is smaller than half of the age of the Universe at the same redshift. We compare to data in a similar mass range by Gallazzi et al. (2014) at $z \sim 0.6$ and by Whitaker et al. (2013, who also uses spectra from 3D-HST) at $1.4 < z < 2.2$, obtaining good agreement. The young ages of quiescent galaxies can be naturally explained by the addition of newly quenched galaxies to the sample. The conclusion is enforced at lower redshift by Choi et al. (2014) who find that quiescent galaxies at $0.2 < z < 0.7$ tend to be younger than half of the age of the Universe at those redshifts. The age value from the highest redshift mapped by Choi et al. (2014) is consistent with the youngest determination from our sample (the best fit from the FSPS10 models).

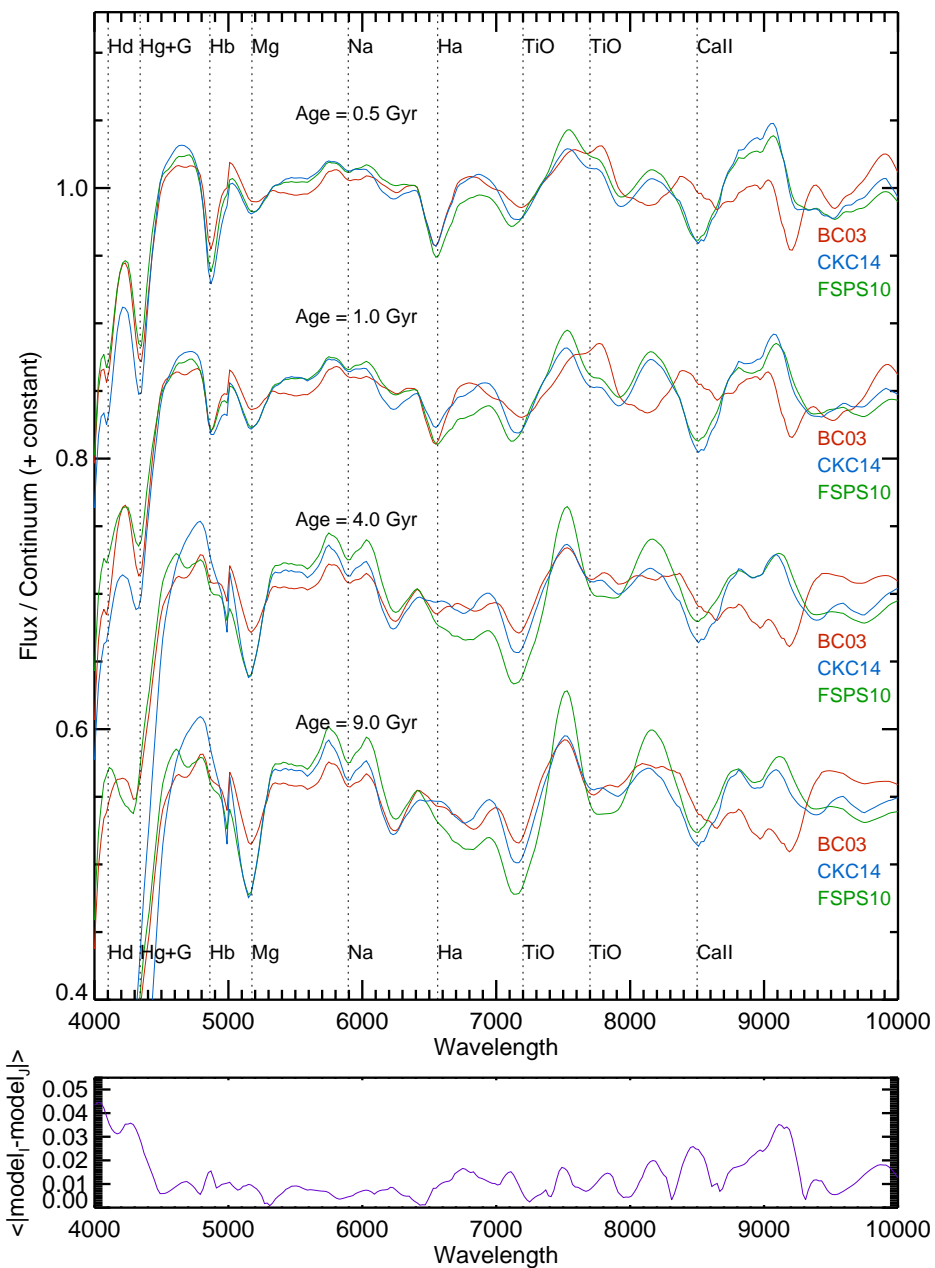


Figure 4.13: Top: SSPs with solar metallicities from BC03 (red), FSPS10 (green), CKC14 (blue). Models are convolved to 3D-HST resolution (see Section 4.3). Bottom: The purple line shows the average absolute difference between models at different wavelengths, for every combination of models of the same age: the difference among models is the biggest at the longest wavelengths and in the D4000 region.

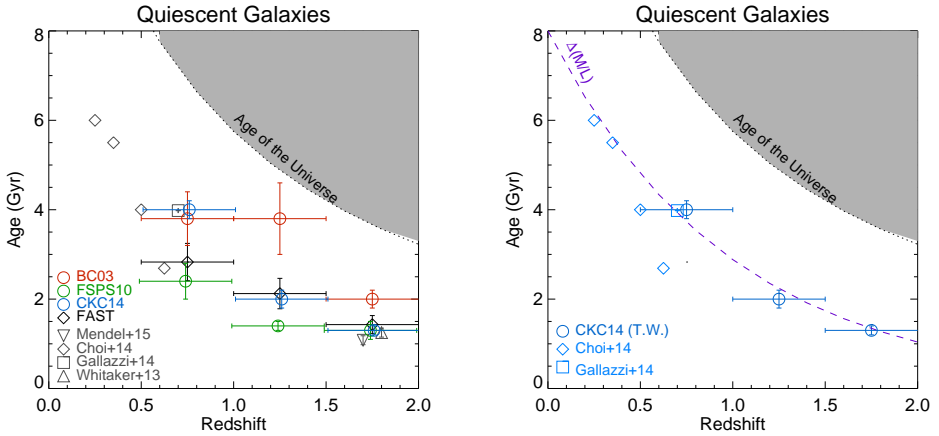


Figure 4.14: Left: Evolution of ages of massive quiescent galaxies ($\log(M_*/M_\odot) > 10.8$) with redshift. Open circles represent values measured from 3D-HST. Different colors represent different stellar population synthesis models (red: BC03, green: FSPS10, blue: CKC14) used for the determination of ages. As a comparison, values inferred from photometry (black diamonds) and from the literature selected in a similar mass range (grey symbols) are plotted. Right: Comparison between the ages determined from 3D-HST spectra and the literature (blue) to the evolution of ages predicted from the evolution of the mass-to-light ratio inferred from the fundamental plane.

Comparison with photometry

Ages of galaxies can also be inferred from photometry only. In 3D-HST stellar masses, star-formation rates, ages and dust extinction are estimated with the FAST code (Kriek et al. 2009), assuming exponentially declining star formation histories with a minimum e-folding time of $\log_{10}(\tau/\text{yr}) = 7$, a minimum age of 40 Myr, $0 < A_V < 4$ mag and the Calzetti et al. (2000) dust attenuation law (see Skelton et al. 2014). The output from the FAST code is an age defined as the time since the onset of SF, that is not necessary equivalent to a light-weighted age.

For each galaxy we therefore compute a light-weighted age (t_{lum}) following the definition:

$$t_{\text{lum}} = \frac{\sum_i \text{SFR}(t_i) \times V_{\text{SSP}}(t - t_i) \times (t - t_i) \times \Delta t}{\sum_i \text{SFR}(t_i) \times V_{\text{SSP}}(t - t_i) \times \Delta t}$$

where:

- t is the time of observation (equivalent to the age of FAST)
- $\text{SFR}(t_i)$ is the star formation rate at time t_i . In the case of the FAST fits $\text{SFR}(t_i)$ has the functional shape of a τ model $\text{SFR}(t_i) \sim \exp(-t_i/\tau)$
- $V_{\text{SSP}}(t - t_i)$ is the V-band flux of $1 M_\odot$ element formed at t_i and observed at time t .
- Δt is the time-step we divide the SFH in (we use $\Delta t = 50$ Myr).

We notice that for an SSP $t_{\text{lum}}(t) = t$.

Figure 4.15 shows the relation between the time from the onset of star-formation t and t_{lum} for a range of models: an SSP, a CSF model, and an exponentially declining model with $\tau = 1\text{Gyr}$. As expected, t_{lum} for an SSP (red line) is well approximated by t . For a CSF (blue line) t_{lum} is always smaller than t , with a increasing difference at later times. This effect is naturally explained by the fact that younger stars are brighter than older stars: V_{SSP} peaks at 10 Myr, and declines afterwards (in other words the mass-to-light ratio M/L_V increases for older stellar populations, see among others Bruzual & Charlot 2003, Fig 1 to 5). The τ model (purple line) has an intermediate behavior, being similar to the CSF for $t \rightarrow 0$, and parallel to the SSP for large t .

For each quiescent galaxy in the sample, we infer t_{lum} from the best fit to its photometry, and find the average value in the three redshift bins $0.5 < z < 1.0$, $1.0 < z < 1.5$ and $1.5 < z < 2.0$. Figure 4.14 (left) shows how the quantity compares to the ages measured from the spectra (Section 4.4) with different sets of models.

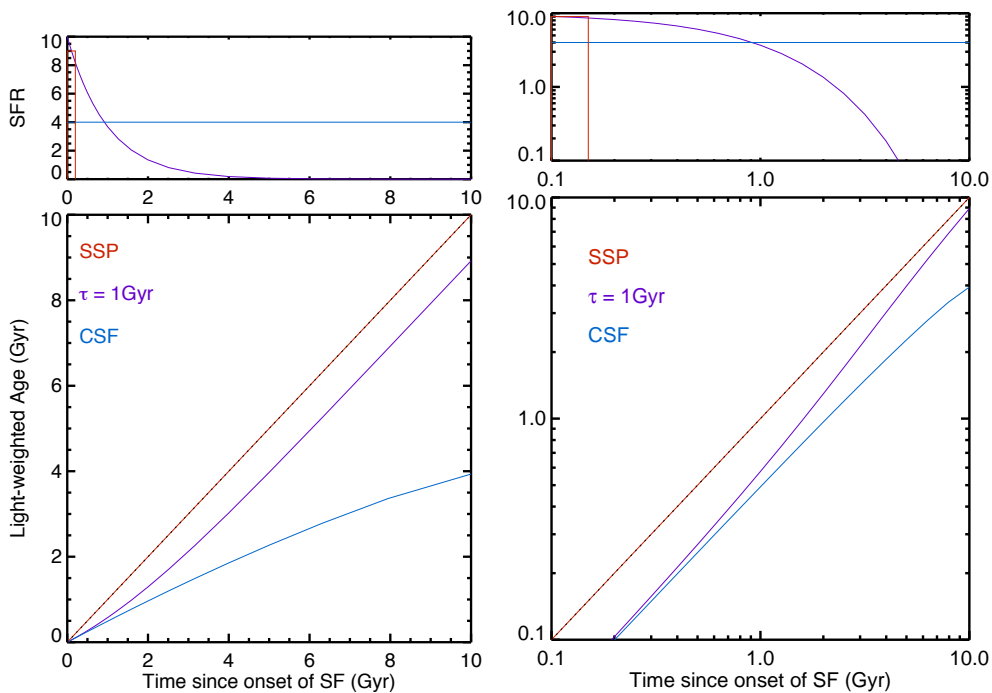


Figure 4.15: Light-weighted ages (t_{lum}) at different times from the onset of star-formation, in linear (left) and logarithmic scale (right). Three different SFH are shown: single stellar population (SSP, red), constant star formation (CSF, blue), and an exponentially declining τ -model with $\tau = 1\text{Gyr}$. For a SSP the light weighted age corresponds to the time from the burst. For a CSF t_{lum} is always lower than the time from the onset of star-formation, with approximately $t_{\text{lum}} \sim t/2$. A τ model has an intermediate behaviour, being asymptotically similar to the CSF at $t \rightarrow 0$ and to the 1-1 slope at later times.

For each redshift bin ages derived from photometry tend to be comparable to the lowest values obtained with the spectral fitting.

Comparison with fundamental plane studies

Another technique commonly used to constrain ages of high redshift quiescent galaxies is provided by the fundamental plane (Djorgovski & Davis 1987, hereafter: FP). In particular, the FP is a model-independent tool for measuring the mass to light ratio (M/L). The offset between the M/L of high redshift galaxies and that of local galaxies can therefore be used to estimate the age of their stellar populations (Franx 1993, van Dokkum & Franx 1996, van der Wel et al. 2004, Treu et al. 2005). Since the luminosity of an SSP evolves with time as $L \sim t^k$, (with the parameter k derived from stellar population models), the relation between the evolution of M/L and light-weighted ages can therefore be approximated as $\Delta \ln(M/L) \sim -k \Delta \ln(t)$. Measurements of the evolution of M/L up to $z \sim 1$ agree with values $\Delta \ln(M/L_B) \sim -1 \times z$ (van Dokkum & Stanford 2003, Wuyts et al. 2004, Holden et al. 2005). Given a value of $k = -0.98$ (from BC03 models in the B band, with a Chabrier IMF), we derive the following relation between the local light-weighted ages and those at high redshift: $t_{lum}(z) = t_{lum}(0) \times e^{-z/0.98}$. The observed evolution of the M/L predicts that the ages of quiescent galaxies at $z \sim 1$ are 2.8 times younger than those at $z = 0$, and 4 times younger at $z \sim 1.5$. Figure 4.14 shows the age evolution predicted from M/L measurements. We use 8 Gyr as the age of galaxies at $z = 0$, as measured from SDSS spectra by Gallazzi et al. (2004). The agreement between the FP prediction and measurements from 3D-HST spectra is excellent. Only the spectral measurement with the BC03 models at $z \sim 1.25$ and the one with the FSPS10 models at $z \sim 0.75$ significantly deviate from the FP prediction.

4.6.3 H α in quiescent galaxies

At redshifts lower than 1.5 we can quantify the H α emission¹ in QGs from the residuals to the best fits (Figure 4.5 and 4.6). We subtract the best-fit model with the CKC14 SPS from the stacks, and fit residuals with a Gaussian centered at the H α wavelength ($\lambda = 6563 \text{ \AA}$). Since the stacks are continuum subtracted, this is effectively a direct measurement of $EW(H\alpha + [NII])$. At the lowest redshifts ($0.5 < z < 1.0$), we do not obtain a significant detection, with $EW(H\alpha + [NII]) = 0.5 \pm 0.3 \text{ \AA}$, while at $1.0 < z < 1.5$ we robustly detect the emission line, measuring $EW(H\alpha + [NII]) = 5.5 \pm 0.8 \text{ \AA}$. In the same mass/redshift regime typical SFGs have $EW(H\alpha + [NII]) \sim 60 \text{ \AA}$ (Fumagalli et al. 2012). This shows that the H α emission in QGs is quenched by a factor of ~ 10 .

To estimate the H α fluxes, we multiply the $EW(H\alpha + [NII])$ by the median continuum flux of galaxies in the stack, and assume a 0.25 ratio for $[NII]/(H\alpha + [NII])$. We finally estimate $SFR(H\alpha)$ with the Kennicutt (1998) relation, obtaining that QGs have $SFR(H\alpha) = 0.46 \pm 0.06 M_\odot / yr$ at $1.0 < z < 1.5$ and $0.10 \pm 0.05 M_\odot / yr$ at $0.5 < z < 1.0$, assuming no dust absorption. In Fumagalli et al. (2014) we reported

¹Given the WFC3 grism resolution H α and [NII] are inevitably blended, therefore we will refer to measurements of $H\alpha + [NII]$

for QGs higher SFR inferred from mid-infrared emissions, up to $3.7 \pm 0.7 M_{\odot}/\text{yr}$ at $1.1 < z < 1.5$. Reconciling the measurements of $\text{SFR}(H\alpha)$ and $\text{SFR}(\text{IR})$ would require a significant dust extinction for the $H\alpha$ line ($A_{H\alpha} \sim 3$). Both estimates are however affected by possible contaminations of other physical processes which can contribute to the observed fluxes. A variety of studies (Fumagalli et al. 2014, Utomo et al. 2014, Hayward et al. 2014) suggests that SFR inferred from IR are overestimated because of the contribution of dust heating by old stars and/or TP-AGB stars to the MIR fluxes. SFRs measured from $H\alpha$ are instead contaminated by potential AGN or LINER emission and affected by dust extinction. Our combined multiwavelength findings agree however in indicating that SFRs of QGs are very low, they are negligible in comparison to those of SFGs at the same redshift, and they are potentially consistent with 0.

4.7 Conclusions

We select massive galaxies from the 3D-HST survey and divide them into quiescent and star-forming according to their rest-frame optical and near-infrared colors. We stack their low-resolution spectra from 3D-HST in three redshift bins, and fit them with models from three stellar population synthesis codes, in order to infer the mean stellar ages of the sample.

For quiescent galaxies, we show that the new CKC14 code provides more accurate fits to the data. Other codes do not reproduce the observed features at the reddest optical wavelengths.

For star-forming galaxies, we are not able to put significant constraints on the stellar ages of the samples.

Even though we infer different stellar ages from different models, stellar ages of quiescent galaxies appear to be overall younger than half of the age of the Universe, confirming the trends found at lower redshift by Choi et al. (2014) and Gallazzi et al. (2014). The evolution of stellar ages is moreover in accordance with the expected evolution from fundamental plane studies.

We thank Jesse van de Sande, Charlie Conroy and Adam Muzzin for the useful discussions. We acknowledge funding from ERC grant HIGHZ no. 227749. This work is based on observations taken by the 3D-HST Treasury Program (GO 12177 and 12328) with the NASA/ESA HST, which is operated by the Association of Universities for Research in Astronomy, Inc., under NASA contract NAS5-26555.

Bibliography

Bell, E. F., Zheng, X. Z., Papovich, C., et al. 2007, *ApJ*, 663, 834

Bell, E. F., van der Wel, A., Papovich, C., et al. 2012, *ApJ*, 753, 167

- Bezanson, R., van Dokkum, P., van de Sande, J., Franx, M., & Kriek, M. 2013, *ApJL*, 764, L8
- Blanton, M. R., Hogg, D. W., Bahcall, N. A., et al. 2003, *ApJ*, 594, 186
- Brammer, G. B., van Dokkum, P. G., & Coppi, P. 2008, *ApJ*, 686, 1503
- Brammer, G. B., Whitaker, K. E., van Dokkum, P. G., et al. 2011, *ApJ*, 739, 24
- Brammer, G. B., van Dokkum, P. G., Franx, M., et al. 2012, *ApJS*, 200, 13
- Bruzual, G., & Charlot, S. 2003, *MNRAS*, 344, 1000
- Bundy, K., Ellis, R. S., Conselice, C. J., et al. 2006, *ApJ*, 651, 120
- Chabrier, G. 2003, *ApJL*, 586, L133
- Choi, J., Conroy, C., Moustakas, J., et al. 2014, *ApJ*, 792, 95
- Damen, M., Labbé, I., Franx, M., et al. 2009, *ApJ*, 690, 937
- Damen, M., Labbé, I., van Dokkum, P. G., et al. 2011, *ApJ*, 727, 1
- Djorgovski, S., & Davis, M. 1987, *ApJ*, 313, 59
- Donley, J. L., Koekemoer, A. M., Brusa, M., et al. 2012, *ApJ*, 748, 142
- Erb, D. K., Shapley, A. E., Pettini, M., et al. 2006, *ApJ*, 644, 813
- Fumagalli, M., Patel, S. G., Franx, M., et al. 2012, *ApJL*, 757, L22
- Fumagalli, M., Labbé, I., Patel, S. G., et al. 2014, *ApJ*, 796, 35
- Gallazzi, A., Charlot, S., Brinchmann, J., & White, S. D. M. 2006, *MNRAS*, 370, 1106
- Gallazzi, A., Bell, E. F., Zibetti, S., Brinchmann, J., & Kelson, D. D. 2014, *ApJ*, 788, 72
- Gobat, R., Strazzullo, V., Daddi, E., et al. 2013, *ApJ*, 776, 9
- Grogin, N. A., Kocevski, D. D., Faber, S. M., et al. 2011, *ApJS*, 197, 35
- Hayward, C. C., Lanz, L., Ashby, M. L. N., et al. 2014, *MNRAS*, 445, 1598
- Ilbert, O., McCracken, H. J., Le Fèvre, O., et al. 2013, *A&A*, 556, AA55
- Karim, A., Schinnerer, E., Martínez-Sansigre, A., et al. 2011, *ApJ*, 730, 61
- Kashino, D., Silverman, J. D., Rodighiero, G., et al. 2013, *ApJL*, 777, LL8
- Kauffmann, G., Heckman, T. M., White, S. D. M., et al. 2003, *MNRAS*, 341, 33
- Kennicutt, R. C., Jr. 1998, *ARA&A*, 36, 189
- Koekemoer, A. M., Faber, S. M., Ferguson, H. C., et al. 2011, *ApJS*, 197, 36
- Kriek, M., van Dokkum, P. G., Labbé, I., et al. 2009, *ApJ*, 700, 221

- Kriek, M., Shapley, A. E., Reddy, N. A., et al. 2015, *ApJS*, 218, 15
- Mendel, J. T., Saglia, R. P., Bender, R., et al. 2015, *ApJL*, 804, L4
- Moustakas, J., Zaritsky, D., Brown, M., et al. 2011, arXiv:1112.3300
- Muzzin, A., Marchesini, D., Stefanon, M., et al. 2013, *ApJ*, 777, 18
- Nelson, E. J., van Dokkum, P. G., Brammer, G., et al. 2012, *ApJL*, 747, L28
- Nelson, E. J., van Dokkum, P. G., Momcheva, I., et al. 2013, *ApJL*, 763, L16
- Onodera, M., Renzini, A., Carollo, M., et al. 2012, *ApJ*, 755, 26
- Onodera, M., Carollo, C. M., Renzini, A., et al. 2014, arXiv:1411.5023
- Patel, S. G., Holden, B. P., Kelson, D. D., et al. 2012, *ApJL*, 748, L27
- Price, S. H., Kriek, M., Brammer, G. B., et al. 2014, *ApJ*, 788, 86
- Tremonti, C. A., Heckman, T. M., Kauffmann, G., et al. 2004, *ApJ*, 613, 898
- Treu, T., Ellis, R. S., Liao, T. X., et al. 2005, *ApJ*, 633, 174
- Utomo, D., Kriek, M., Labbé, I., Conroy, C., & Fumagalli, M. 2014, *ApJL*, 783, LL30
- van de Sande, J., Kriek, M., Franx, M., et al. 2013, *ApJ*, 771, 85
- van Dokkum, P. G., Whitaker, K. E., Brammer, G., et al. 2010, *ApJ*, 709, 1018
- van Dokkum, P. G., Brammer, G., Fumagalli, M., et al. 2011, *ApJL*, 743, LL15
- Williams, R. J., Quadri, R. F., Franx, M., van Dokkum, P., & Labbé, I. 2009, *ApJ*, 691, 1879
- Wuyts, S., Labbé, I., Franx, M., et al. 2007, *ApJ*, 655, 51

5

DECREASING $H\alpha$ FOR REDDER STAR-FORMING GALAXIES: INFLUENCE OF DUST AND STAR FORMATION RATES

We analyze a large sample of 7000 galaxies from the 3D-HST survey in the redshift range $0.7 < z < 1.5$, where $H\alpha$ falls into the wavelength coverage of the WFC3 G141 grism. We divide galaxies onto quiescent and star-forming on the basis of the widely used UVJ rest-frame color-color criterion. We demonstrate that galaxies with strong and weak $H\alpha$ are well separated in the UVJ diagram. The $H\alpha$ line is detected ($S/N > 3$) in $\sim 85\%$ of the star-forming sample, while less than 20% of UVJ selected quiescent galaxies have an $H\alpha$ detection, with an average $EW(H\alpha)$ of $< 5 \text{ \AA}$. For star-forming galaxies, we investigate how $H\alpha$ varies as a function of the rest frame colors of the galaxy and how it relates to the specific star formation rate (sSFR), measured from the UV and mid-IR emission. We find that, at a fixed mass, red star-forming galaxies have lower $EW(H\alpha)$ than blue star-forming galaxies, with a decrease of 0.5 dex in $EW(H\alpha)$ per magnitude in U-V color. We also show that the median sSFR(UV+IR) of galaxies decreases towards redder U-V colors. In addition, the median IRX ratio ($\log L_{\text{IR}} / L_{\text{UV}}$) increases towards redder colors. This result demonstrates that the redder colors of red star-forming galaxies, compared to those of similar-mass blue star-forming galaxies are due to both their higher dust content and their lower sSFR. We show that the ratio $L(H\alpha) / \text{SFR}$ varies systematically with both U-V color and stellar mass. The systematic variation is approximately 1 dex with stellar mass, with an additional variation of 0.5 dex with color after the mass dependence has been removed. We show that the overall variation of $EW(H\alpha)$ as a function of color can be explained by the combined effect of lower sSFR and higher dust absorption for galaxies with redder colors

Mattia Fumagalli; Marijn Franx; Ivo Labbé; Pieter G. van Dokkum; et al.
Submitted to the Astrophysical Journal

5.1 Introduction

In studies of galaxy evolution, populations of star-forming and quiescent objects are generally tracked through cosmic time based on their rest-frame colors (among others: Faber et al. 2007, Muzzin et al. 2013). This technique is supported by the observed bimodality in galaxy colors: in a color-luminosity (or more fundamentally color-mass) diagram, the distribution of galaxies consists of early-type objects residing on a sequence at red colors well separated from a cloud of blue late-type galaxies. This bimodality is observed in both the local Universe (e.g. Blanton et al 2003), and up to $z \sim 2.5$ -3 (e.g. Brammer et al. 2009).

A selection based on a single rest-frame color can however result in a mixed set of both passive, dead galaxies, and dust-reddened star-forming galaxies, whose optical colors can be as red as (or redder than) those of purely quiescent galaxies (Maller et al. 2009). In order to better distinguish star-forming (SFGs) and quiescent galaxies (QGs), the usage of a color-color diagram, typically rest-frame U-V versus rest-frame V-J, has emerged (UVJ diagram, Labbé et al. 2005, Williams et al. 2009). In this color-color space, the old stellar populations of QGs produce red U-V colors and relatively blue V-J colors, while the reddest SFGs are red in both U-V and V-J.¹

The selection of QGs in the UVJ diagram has been used to identify quenched objects up to $z = 4$ (Straatman et al. 2014), and corresponds up to at least $z \sim 2.0$ to a selection of dead galaxies with low mid-IR fluxes (Fumagalli et al. 2014) and an old stellar population (Whitaker et al. 2013, Fumagalli et al. 2015, Mendel et al. 2015). Moreover, it is roughly equivalent to a morphological selection of early-type galaxies, at least up to intermediate redshifts (Patel et al. 2012).

In the UVJ space, the two sequences are basically parallel and both feature a significant color spread. An identical reddening effect, parallel to the sequences, can be obtained by increasing age, dust, or metallicity. The three effects are notoriously difficult to disentangle: the difference in rest-frame U-V and V-J colors corresponding to 1 Gyr of passive evolution with the Bruzual & Charlot (2003) models is almost identical in magnitude and direction to that obtained by increasing the metallicity from $\log(Z)=0.02$ (Solar) to $\log(Z)=0.05$, or adding 0.5 mag of dust reddening following the Calzetti et al. (2000) dust law.

For QGs, the color spread is interpreted as an effect of mainly age, with blue QGs featuring a post starburst-like spectral energy distribution (SED), while redder QGs have SEDs consistent with older stellar ages (Whitaker et al. 2012). Recent works based on spectroscopy (Whitaker et al. 2013, Mendel et al. 2015) confirmed that the bluest UVJ selected QGs have strong Balmer lines and a light-weighted age of ~ 1 Gyr, while the reddest quiescent galaxies are dominated by metal lines and have a relatively older mean age.

The color spread of SFGs, spanning 2 magnitudes in both U-V and V-J, is instead generally interpreted as driven by different levels of dust absorption (Williams et al. 2009). At intermediate redshifts Patel et al. (2012) showed that the variation in [OII] luminosity of star-forming galaxies is consistent with that predicted by models of dust absorption through an inclined disk, as most of the highly inclined spirals are

¹An alternative is to correct the observed U-V colors for reddening; see Brammer et al. (2009).

identified at the reddest rest-frame colors.

In this paper we use the observed $H\alpha$ to investigate the systematic variation of SFGs as a function of their rest-frame color. We focus on galaxies in the redshift window where $H\alpha$ can be observed with the Hubble Space Telescope / Wide Field Camera 3 (HST/WFC3) grism ($0.7 < z < 1.5$), in the context of the 3D-HST survey, a large spectroscopic survey aimed at obtaining unbiased, mass-selected, samples of rest-frame spectra at high redshift.

After introducing the data in Section 5.2, we analyze the dependence of $EW(H\alpha)$ on color in Section 5.3. In Section 5.4 and 5.5 we investigate its origin by analyzing color trends for sSFR and dust absorption. We further confirm in Section 5.5 that emission lines are more absorbed than the underlying continuum.

In the entire paper, we assume a Chabrier (2003) IMF and refer measurements to a Λ CDM cosmology with $\Omega_M = 0.3$, $\Omega_\Lambda = 0.7$, and $H_0 = 70$ km/(s Mpc). All magnitudes are given in the AB system.

5.2 Data and Sample Selection

5.2.1 The 3D-HST survey

The 3D-HST program (van Dokkum et al. 2011; Brammer et al. 2012) is a 600 arcmin² wide survey using WFC3 grism onboard Hubble Space Telescope (HST) to obtain low-resolution near-IR spectra for a complete, unbiased sample of thousands of galaxies (Cycles 18 and 19, PI: van Dokkum). It has an integration time of 248 orbits and it observes four fields with a wealth of publicly available imaging data from the U band to 24 μ m (AEGIS, COSMOS, GOODS-S and UDS), and it incorporates similar, publicly-available data, in the GOODS-N field (GO:11600; PI:Weiner). Extensive photometric data in these fields have been described in Skelton et al. (2014).

The WFC3 grism spectra have been extracted with the pipeline described in Momcheva et al. (2015, in prep). Redshifts have been measured via the combined photometric and spectroscopic information using a modified version of the EAZY code (Brammer et al. 2008). The precision of redshifts is shown to be $\sigma(\frac{dz}{1+z}) = 0.3\%$ (Brammer et al. 2012, Momcheva et al. 2015 in prep.). In grism spectroscopy the width of spectral features reflects almost exclusively the size of the galaxy in the dispersion direction (see Nelson et al. 2012, 2013). Emission lines are therefore fit using a line shape determined by the object profile (Brammer et al. 2012, Momcheva et al. 2015 in prep.). Given the low spectral resolution of 3D-HST, the $H\alpha$ and $[N_{II}]$ lines are unavoidably blended together. For the ease of reading we refer to $EW(H\alpha+[N_{II}])$ simply as $EW(H\alpha)$ through the entire paper.

Stellar masses have been determined using the FAST code by Kriek et al. (2009), using Bruzual & Charlot (2003) models, and assuming exponentially declining SFHs, solar metallicity, a Chabrier (2003) IMF, and a Calzetti (2000) dust law.

SFR measurements are described in Whitaker et al. (2014). In brief, SFRs are determined by adding the rest-frame UV light from young stars to the IR luminosity (Gordon et al. 2000). Total IR luminosities ($L(IR) = L(8 - 1000\mu\text{m})$) are estimated from the observed Spitzer/MIPS 24 μ m fluxes, using a conversion based on a single

template which is the average of Dale & Helou (2002) templates with $1 < \alpha < 2.5$, following Wuyts et al. (2008), Franx et al. (2008), and Muzzin et al. (2010). The rest-frame UV luminosity is estimated by using the 2800\AA rest-frame luminosity multiplied by 1.5 to account for the UV spectral shape of a 100 Myr old population with constant SFR (as in Bell et al. 2005): $L(\text{UV})=1.5 \nu L_\nu(2800\text{\AA})$. In the 3D-HST data, rest frame luminosities such as $\nu L_\nu(2800\text{\AA})$ are estimated from the observed photometry by interpolating over the best fit templates (Brammer et al. 2011).

Assuming a Chabrier (2003) IMF, SFRs are then evaluated as

$$\text{SFR}[M_\odot/\text{yr}] = 1.09 \times 10^{-10} (L(\text{IR}) + 2.2L(\text{UV})) [L_\odot] \quad (5.1)$$

where $L(\text{IR})$ is the bolometric IR luminosity, $L(\text{UV}) = 1.5 \nu L_\nu(2800\text{\AA})$ the $1216 - 3000\text{\AA}$ luminosity, and the factor of 2.2 accounts for the unobscured starlight of young stars emitted redward of 1216\AA and blueward of 3000\AA (Bell et al. 2005).

5.2.2 Sample selection and the UVJ diagram

The 3D-HST G141 grism spectroscopy covers the $\text{H}\alpha$ rest-frame wavelength at $0.7 < z < 1.5$. We therefore select all galaxies in this redshift range with grism coverage (which amounts to 75% of F160W-selected galaxies in the CANDELS sample).

The 3D-HST team has done a visual inspection of all the objects in the catalogs (see Momcheva et al. 2015). Each object has been seen by two classifiers. Each one independently marked objects with *bad* spectra, such as ones with a non-subtracted star contaminating the object, a fake emission line caused by the contamination subtraction, or numerical effects causing blank blobs in the 2D spectrum; an *uncertain* category was also available for objects with no clear classification. We exclude objects classified by at least one person as *bad* or flagged by both as *uncertain*.

After this selection we are left with 7100 objects in the redshift range $0.7 < z < 1.5$ (80% of the original sample). We test possible biases between the original sample and the final one with a Kolmogorov-Smirnov test on their distribution in mass, redshifts, F140W magnitudes and U-V color. We find that the two samples are drawn from the same distribution with respect to the mass (at the 97% level), redshift (at the 95% level), magnitude (at the 99% level), and color (at the 95% level).

We divide galaxies into star-forming (SFGs) and quiescent (QGs) using a color-color technique (Labbé et al. 2005), specifically rest-frame U-V versus rest-frame V-J (hereafter: UVJ diagram). This method has been shown to be effective in selecting star-forming galaxies, including the red dust-reddened ones, from galaxies that are red because their light is dominated by an old stellar population (Williams et al. 2009). Effectively, SFGs are identified with the criteria $(U - V) > 0.8 \times (V - J) + 0.7$, $U - V > 1.3$ and $V - J < 1.5$ (as in Whitaker et al. 2014).

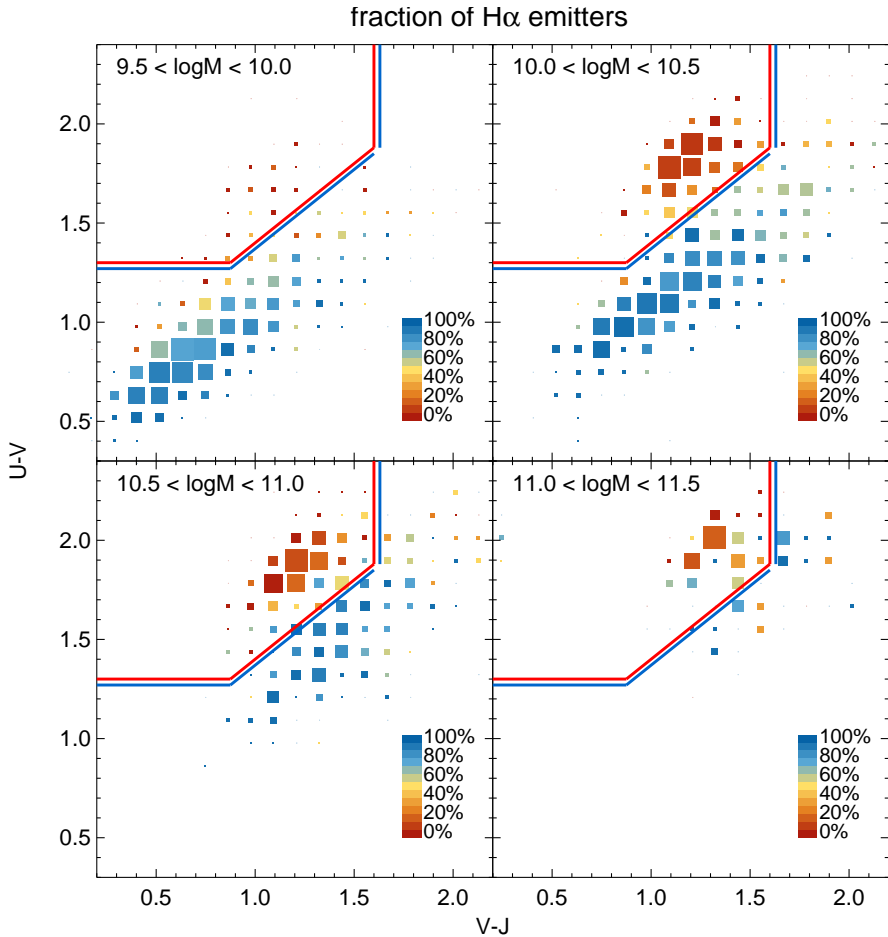


Figure 5.1: UVJ diagram for 3D-HST galaxies at $0.7 < z < 1.5$ in different mass bins. The selection box divides quiescent and star-forming galaxies. Each 0.1×0.1 mag bin has an area proportional to the number of galaxies in the region, and it is color-coded by its percentage of $H\alpha$ detections ($S/N > 3$). Star-forming galaxies have generally a high fraction ($>80\%$) of $H\alpha$ emitters, while less than 20% quiescent galaxies have an $H\alpha$ detections. The fraction of $H\alpha$ detections in star-forming galaxies decreases towards the reddest colors.

5.3 $EW(H\alpha)$: trend with color

5.3.1 Separating star-forming and quiescent galaxies with the UVJ selection

We investigate first how the $H\alpha$ emission varies as a function of the spectral energy distribution shape of galaxies, as tracked by a galaxy's position in the UVJ diagram. In Figure 5.1 we show, for different mass bins, the UVJ diagram divided into color-color bins of size 0.1 mag, where each bin is color-coded by the fraction of galaxies with an $H\alpha$ detection (defined by signal-to-noise > 3). For QGs the fraction of $H\alpha$ emitters is generally low ($< 20\%$), while for SFGs it is, for most color-color bins,

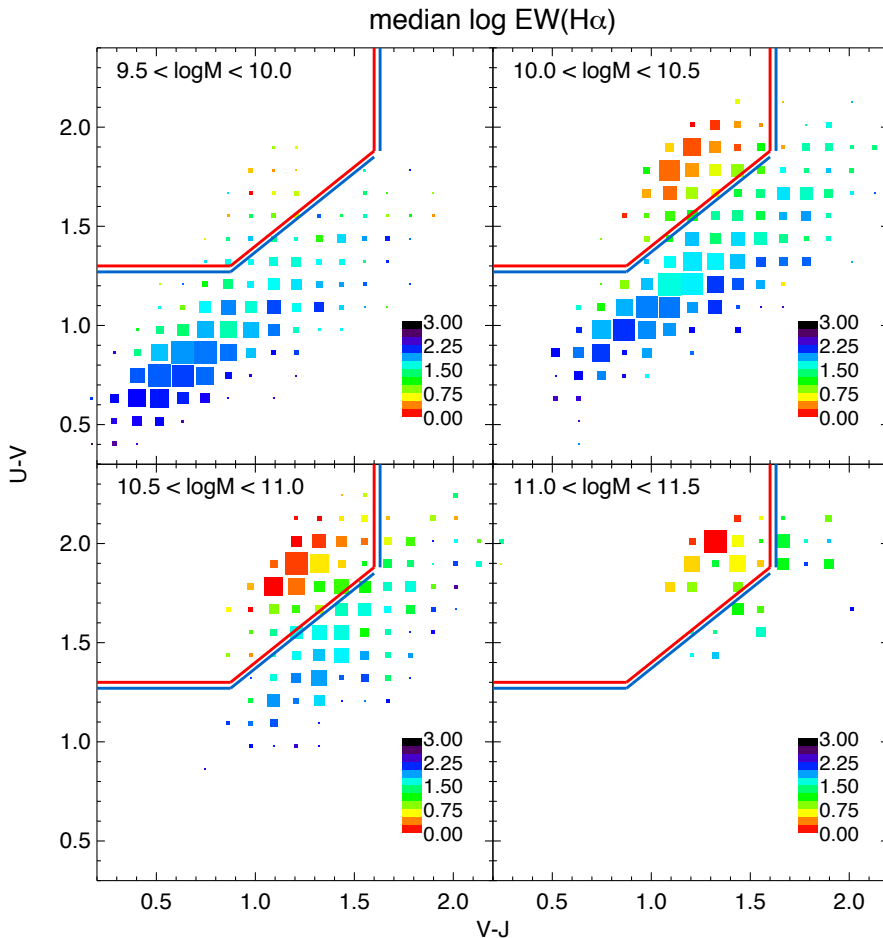


Figure 5.2: Dependence of $\text{EW}(\text{H}\alpha)$ on $U-V$ and $V-J$ colors. Each 0.1×0.1 mag bin is color-coded by median $\log \text{EW}(\text{H}\alpha)$, for different mass bins. The selection box is used to divide quiescent and star-forming galaxies. Quiescent galaxies have $\text{EW}(\text{H}\alpha)$ of a few \AA ; star-forming galaxies span a range in $\text{EW}(\text{H}\alpha)$ from 10 to a few hundreds. At the same mass red star-forming galaxies tend to have lower $\text{EW}(\text{H}\alpha)$ than that of blue star-forming galaxies.

higher than 80%. We notice that the fraction of SFGs that are $\text{H}\alpha$ emitters decreases towards the reddest colors (to about 60%), in both $U-V$ and $V-J$. This decrease could be explained by galaxies with $\text{H}\alpha$ emission below the detection limit in the reddest part of the sample.

This is also seen in the color dependence of $\text{EW}(\text{H}\alpha)$: in Figure 5.2 we populate the UVJ diagram with the median $\log \text{EW}(\text{H}\alpha)$ in each 0.1×0.1 mag color-color bin, for different mass bins. The $\text{EW}(\text{H}\alpha)$ of SFGs spans a range from ~ 20 to ~ 200 (in agreement with Fumagalli et al. 2012). In each mass range, the $\text{EW}(\text{H}\alpha)$ of SFGs depends on the colors: galaxies with bluer colors (in both $U-V$ and $V-J$) have a higher $\text{EW}(\text{H}\alpha)$ than that of red objects. In the mass ranges with the largest color spread, the difference in $\text{EW}(\text{H}\alpha)$ from the bluest to the reddest galaxies amounts to

a factor of 10. In contrast, the median $EW(H\alpha)$ of QGs is low, generally lower than a few Angstroms, in accordance with Fumagalli et al. (2015), who stacked massive ($\log M^*/M_\odot > 10.8$) QGs, subtracted the best fit stellar continuum and evaluated the residual $H\alpha$ emission.

5.3.2 Color dependence of $EW(H\alpha)$ for star-forming galaxies

We next investigate how the $EW(H\alpha)$ varies as a function of color, for star-forming galaxies. Figure 5.3 shows, for SFGs only, the U-V color dependence of $EW(H\alpha)$, in two redshift bins and four mass bins. Blue SFGs have on average higher $EW(H\alpha)$ than red SFGs. We quantify the relation between $EW(H\alpha)$ and U-V from a linear least squares fitting to the data shown in Fig. 5.3:

$$\log EW(H\alpha) = (2.56 \pm 0.06) - (0.47 \pm 0.05) \times (U - V) \quad (5.2)$$

We see no significant dependence in the fit by dividing the sample in two redshift bins (Figure 5.3). At $0.7 < z < 1.0$, the best fit values of the $EW(H\alpha) = a + b \times (U - V)$ equation are $a = 2.47 \pm 0.09$ and $b = -0.49 \pm 0.08$, while at $1.0 < z < 1.5$ they are $a = 2.49 \pm 0.07$ and $b = -0.43 \pm 0.07$. We find that the biweight scatter at fixed color is approximately constant (0.25 dex).

Galaxies with a higher mass tend to have lower $EW(H\alpha)$ than that of lower mass galaxies (see also Figure 5.2), in agreement with Fumagalli et al. (2012). We therefore evaluate if the trend with color might be only a consequence of the mass trend by examining narrow mass bins, in Figure 5.3 (right). We observe the same trend between color and $EW(H\alpha)$ in 0.5 dex wide mass bins. The median trends in narrow mass bins fall perfectly on top of the one observed for the entire sample and described in Equation 5.2. In other words, galaxies with different masses but the same color have on average the same $EW(H\alpha)$.

The observed trend with $EW(H\alpha)$ can be explained by either changes in the SFH or differences in the extinction. In the following Sections we investigate if the variation in the $EW(H\alpha)$ can be due to differences in the sSFR (Section 5.4) or to differences in the dust extinction (Section 5.5).

The sequence of star-forming galaxies in the UVJ diagram has been generally linked to mainly variations in the dust absorption (Williams et al. 2009, Patel et al. 2012, Kriek et al. 2015). This study will test this hypothesis by analyzing differences between red and blue SFGs with independent $H\alpha$ data, and investigating the link between variations in the $EW(H\alpha)$ and those in sSFR and dust extinction.

5.4 Specific Star Formation Rates of star-forming galaxies: trend with color

Since $EW(H\alpha)$ is defined as the ratio of the $H\alpha$ flux to that of the underlying stellar continuum, it represents a measure of the the current to past average star formation.

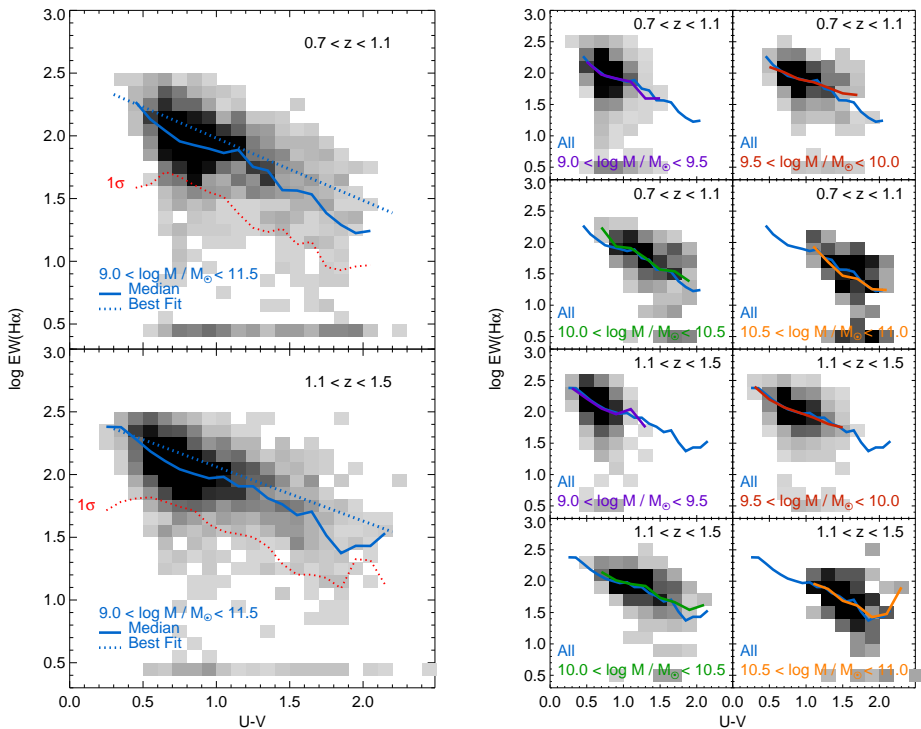


Figure 5.3: Rest Frame $EW(H\alpha)$ vs $U-V$ for star-forming galaxies. Left: data are divided in two redshift bins (top and bottom rows). Red star-forming galaxies have lower $EW(H\alpha)$ than that of blue galaxies. Blue solid lines represent the median values through the samples, while blue dotted lines show the best fit from a linear least-squares minimization. Red dotted lines represent the median 1σ errors through the samples. Right: star-forming galaxies are divided into 0.5 dex wide mass bins, showing that the $EW(H\alpha)$ -color trend holds also in narrow mass bins. Solid (purple, red, green, orange) lines represent the median values through the samples, and always lie on top of the median for all galaxies in the same redshift bin (blue). Star-forming galaxies with different mass but same color have on average the same $EW(H\alpha)$.

It is related to the sSFR, assuming no extra dust absorption towards HII regions:

$$EW(H\alpha) = \frac{L(H\alpha)}{L_\lambda(6563\text{\AA})} \sim \frac{K^{-1} \times SFR}{M \times \frac{L(R)}{M}} = sSFR \times \frac{M}{L(R)} \times K^{-1} \quad (5.3)$$

where K is the Kennicutt (1998) conversion factor from $H\alpha$ luminosity to SFR and $\frac{M}{L(R)}$ is the mass-to-light ratio in the R-band.

In Figure 5.4 (left) we show the dependence of sSFR on the $U-V$ color of SFGs. We notice again that blue galaxies have on average higher star formation rates than redder galaxies. We evaluate the decline of sSFR with color as a factor of 4 (0.6 dex) per magnitude of $U-V$ color. The scatter in sSFR is large (0.45 dex). After we subtract the trend with color, it is reduced to 0.3 dex. At fixed color, the scatter in sSFR increases towards redder colors: from $\sigma = 0.2$ dex at $U-V \sim 0.5$ to $\sigma = 0.4$ dex at $U-V \sim 1.5$.

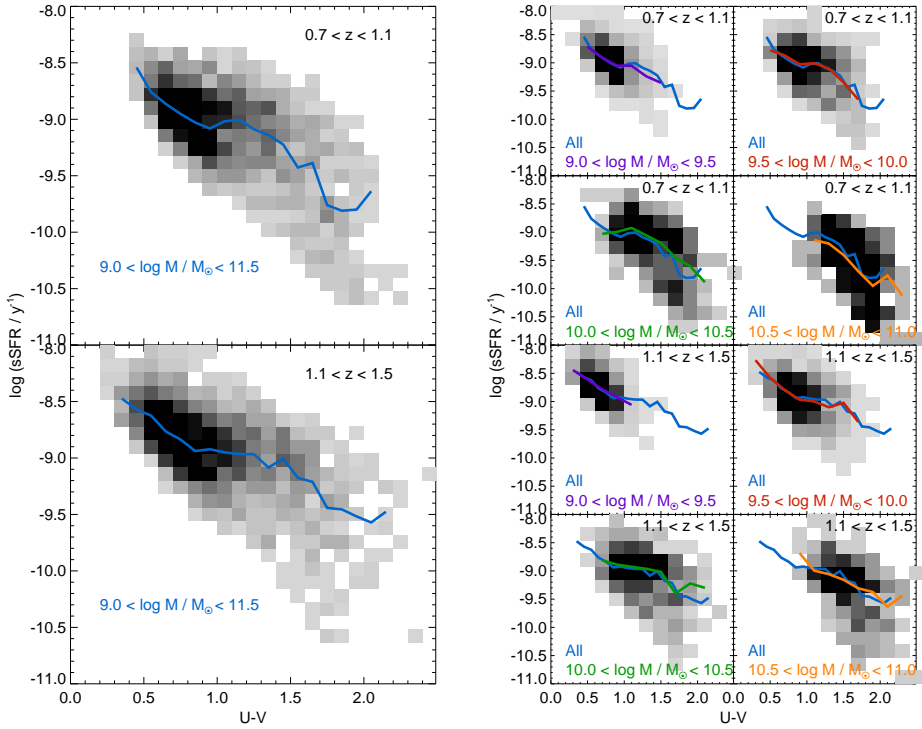


Figure 5.4: Rest Frame sSFR (UV+IR) vs U-V for star-forming galaxies in the 3D-HST catalog. Left: data are divided in two redshift bins (top and bottom rows). Solid blue lines represent median values through the samples in each redshift bin. Red star-forming galaxies have lower sSFR than that of blue star-forming objects. Right: star-forming galaxies are divided into 0.5 dex wide mass bins, showing that the relation holds true also in narrower mass bins. Solid (purple, red, green, orange) lines represent the median values through the samples, and always lie on top of the median for all galaxies in the same redshift bin (blue). Star-forming galaxies with different mass but same color have on average the same sSFR.

We notice that recent studies (Utomo et al. 2014, Hayward et al. 2014, Fumagalli et al. 2014) have indicated that $SFR(UV+IR)$ systematically overestimates the SFR for low sSFRs, as cirrus dust heated by evolved stellar populations significantly contributes to the mid-IR emission. Utomo et al. (2014) evaluates that $sSFR(IR+UV)$ is a reliable measure of sSFR only for $sSFR > 10^{-10} \text{ yr}^{-1}$, and it overestimates sSFR by a factor of 0.5 at $sSFR \sim 10^{-10.5} \text{ yr}^{-1}$. All but a fraction of the reddest galaxies ($U-V > 1.7$) in our sample have $sSFR > 10^{-10} \text{ yr}^{-1}$. If the sSFRs of some of the reddest objects are overestimated, the decline of sSFR with color is possibly even steeper than 0.6 dex per magnitude of U-V color.

It is moreover known that masses and SFRs are correlated, with most authors finding a non-linear relation for the ‘star-forming main sequence’ $SFR \sim M^\alpha$ with α ranging from 0.6 to 0.9 (e.g. Whitaker et al. 2010, Karim et al. 2012), resulting in a negative correlation between M and sSFR. In Figure 5.4 (right) we show, for 0.5 dex wide mass bins, the relation between color and sSFR: we find that also in narrow

mass bins redder galaxies have on average lower sSFR than bluer galaxies, and that the scatter in the relations increases at the reddest colors. At a fixed color, SFGs of different masses have on average the same sSFR.

The relation between sSFR and $EW(H\alpha)$ depends on the assumed SFH of the galaxy, as shown by the dependence of Equation 5.3 on the mass-to-light ratio, which is different for different SFHs.

We evaluate the relation between sSFR and $EW(H\alpha)$ from the models as follows: for a set of SFHs (constant SFR, and exponentially declining models with $\tau = 0.3, 1.0,$ and 3.0 Gyr), $L(H\alpha)$ is derived from the Kennicutt (1998) law, while BC03 models are used to calculate the stellar continuum, assuming solar metallicity and no dust. As the sSFR in the models decreases, $EW(H\alpha)$ gets smaller, with a different steepness in the $EW(H\alpha)$ -sSFR relation according to the model in use. For a CSF, a variation of $\Delta sSFR = 1$ dex corresponds to a factor of 2 (0.3 dex) in $\Delta EW(H\alpha)$. For an exponentially declining model with a short $\tau=300$ Myr, a variation of $\Delta sSFR = 1$ dex corresponds to a factor of 5 (0.7 dex) in $\Delta EW(H\alpha)$.

We measure the observed variation in sSFR as $\Delta sSFR = 0.67$ dex per magnitude of U-V color (Figure 5.4). Based on variations in sSFR alone, we predict the $EW(H\alpha)$ to vary of a factor of ~ 1.4 -2.4 (0.15-0.38 dex), respectively under the assumption of a CSF or a $\tau=300$ Myr model.

The observed decline of $EW(H\alpha)$ with color amounts to a factor of 3 per magnitude of U-V color (0.5 dex, Figure 5.2 and Equation 5.2). We therefore conclude that the variation in sSFR alone is unable to explain the full variation of $EW(H\alpha)$.

5.5 Dust absorption of star-forming galaxies along the UVJ diagram

5.5.1 Absorption in $H\alpha$

We quantify the dust absorption in $H\alpha$ by comparing the $H\alpha$ luminosity² to the SFR (inferred from UV+IR, Section 2). In the absence of dust, we expect the two quantities to follow the Kennicutt (1998) relation:

$$SFR[M_{\odot}/yr] = 7.9 \times 10^{-42} \times L(H\alpha)[erg/s] \times 10^{-0.2} \quad (5.4)$$

where the $10^{-0.2}$ factor accounts for a conversion to the Chabrier IMF, from a Salpeter IMF (as in Marchesini et al. 2009).

In Figure 5.5 we plot the ratio of $L(H\alpha)$ to SFR against the masses of galaxies. At each mass, the ratio is lower than the expectation from the Kennicutt law (shown in green). The ratio decreases towards higher masses, with a decrease of ~ 0.4 dex per each dex in mass, as quantified by a least-square fit to the data:

$$\eta = \log \frac{L(H\alpha)}{SFR} = (45.1 \pm 0.2) - (0.41 \pm 0.02) \times \log(M_*/M_{\odot}) \quad (5.5)$$

²We assume that $[N_{II}]$ contributes to 15% of the measured $H\alpha$ emission line flux, as in Wuyts et al. 2013, such that the $[N_{II}]/(H\beta + [N_{II}])$ ratio equals 0.15.

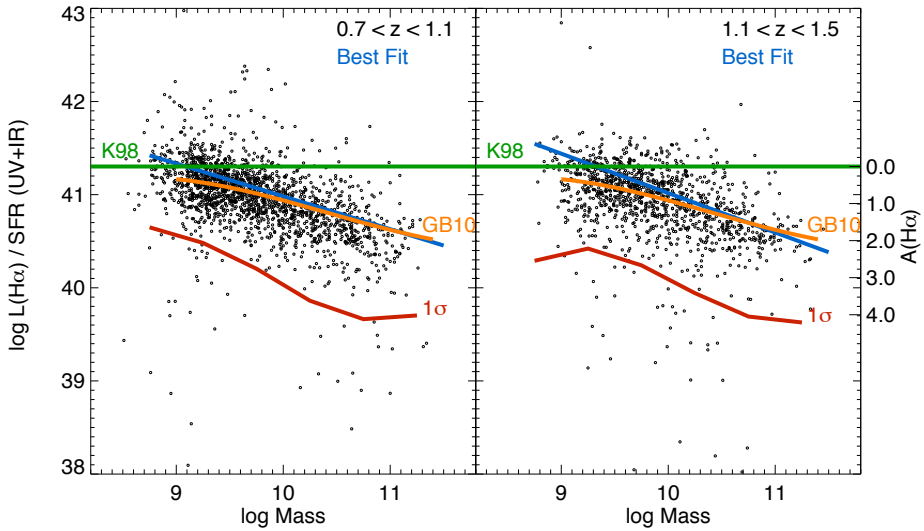


Figure 5.5: Ratio of $H\alpha$ luminosities to SFR as a function of mass for star-forming galaxies, in two different redshifts. Galaxies with higher mass have lower $L(H\alpha)/SFR$ than that of low mass objects, indicating a higher absorption in the $H\alpha$ line. The expected value from the Kennicutt (1998) law is shown in green. The right axis shows the effect of different magnitudes of absorption in $H\alpha$. The Garn & Best relation between mass and dust obscuration at $z=0$ is shown in orange, while the best fit to the 3D-HST data is shown in blue.

indicating that SFGs with a higher mass have higher dust obscuration towards $H\alpha$ than that of lower mass objects. We do not see any significant redshift dependence in the relation: after we split the sample in two redshift bins (Figure 5.5) and fit them with a linear model, we find slopes and y-intercept values compatible at the 1σ level with those in Equation 5.5.

This trend is consistent with previous studies finding that $A(H\alpha)$ increases towards higher stellar masses, both in the local Universe (Garn & Best 2010) and at higher redshift (Sobral et al. 2012, Kashino et al. 2013, Price et al. 2014), with no significant redshift dependence in the $A(H\alpha)$ -mass relation. We show the effect of the Garn & Best (2010) relation for galaxies at $z \sim 0.1$ onto our measurements of $L(H\alpha)/SFR$ at $0.7 < z < 1.5$ in Figure 5.5 (orange lines), demonstrating a good agreement with our data.

We further investigate the dependence of $L(H\alpha) / SFR$ on color. In Figure 5.6 we show how the quantity varies in the UVJ diagram, in different mass bins. In each mass bin, red SFGs have lower η than blue SFGs, indicating that $H\alpha$ is more absorbed in those systems.

In Figure 5.7 we show how η relates to the U-V color of the galaxy. We find that on average galaxies with red (U-V=1.5) color have $\eta \approx 40.5$, while for blue objects (U-V = 0.7) $\eta \approx 41$. In Figure 5.7 (right) we divide the sample in narrow mass-bins, showing that the color- η trend persists also at fixed mass. We notice that galaxies of the same color have, on average, the same $L(H\alpha)/SFR$ ratio despite differences in

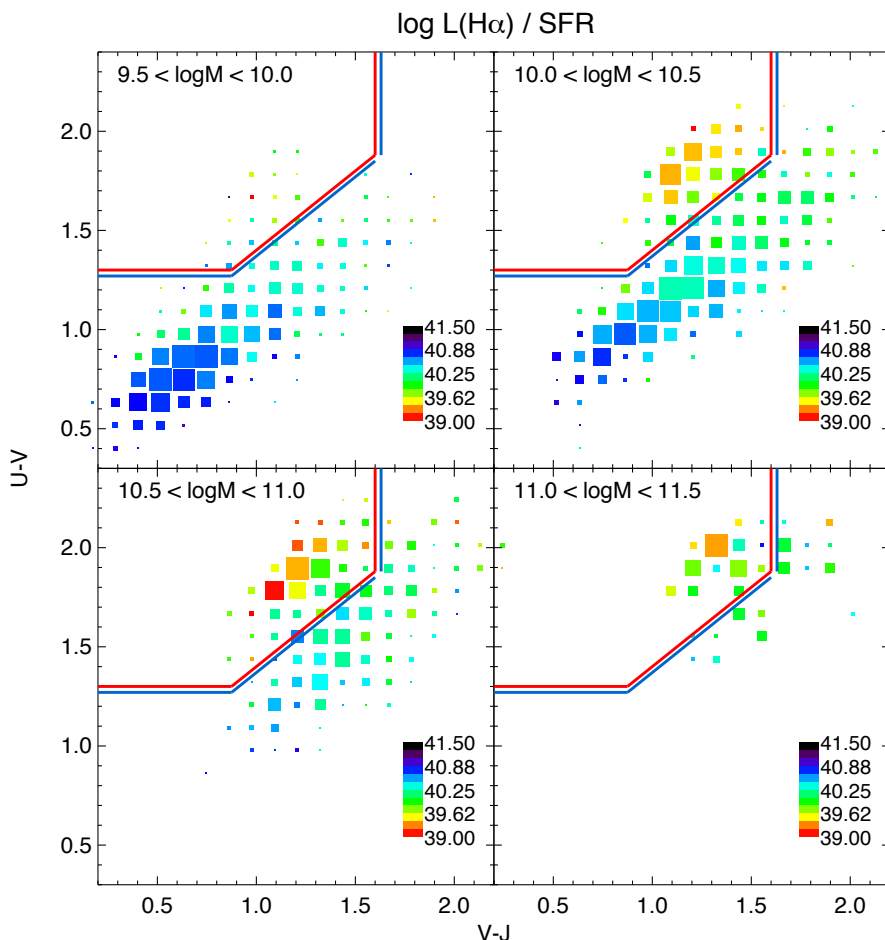


Figure 5.6: UVJ diagram for 3D-HST galaxies at $0.7 < z < 1.5$ in different mass bins, color-coded by median ratio of $H\alpha$ to SFR. The selection box divides quiescent and star-forming galaxies. Red SFGs have lower $L(H\alpha)/SFR$ ratios, indicating a higher dust extinction in $H\alpha$.

mass.

Since redder galaxies tend to be more massive than blue galaxies, we investigate if the trend with color can be explained by the mass dependence only. We subtract the trend of Equation 5.5 from the observed $L(H\alpha) / SFR$, and look at the residual trend with color in Figure 5.8. We still observe a decrease of ≈ 0.5 dex in $L(H\alpha) / SFR$ per each dex in U-V color.

The influence of dust on $EW(H\alpha)$ depends however on the relative absorption between the stellar continuum and the nebular emission (Calzetti et al. 2000), which is a matter of debate at high-redshift (Erb et al. 2006, Forster-Schreiber et al. 2010, Reddy et al. 2010, Kashino et al. 2013, Price et al. 2014, Reddy et al. 2015). We therefore need to also evaluate the attenuation in the stellar continuum.

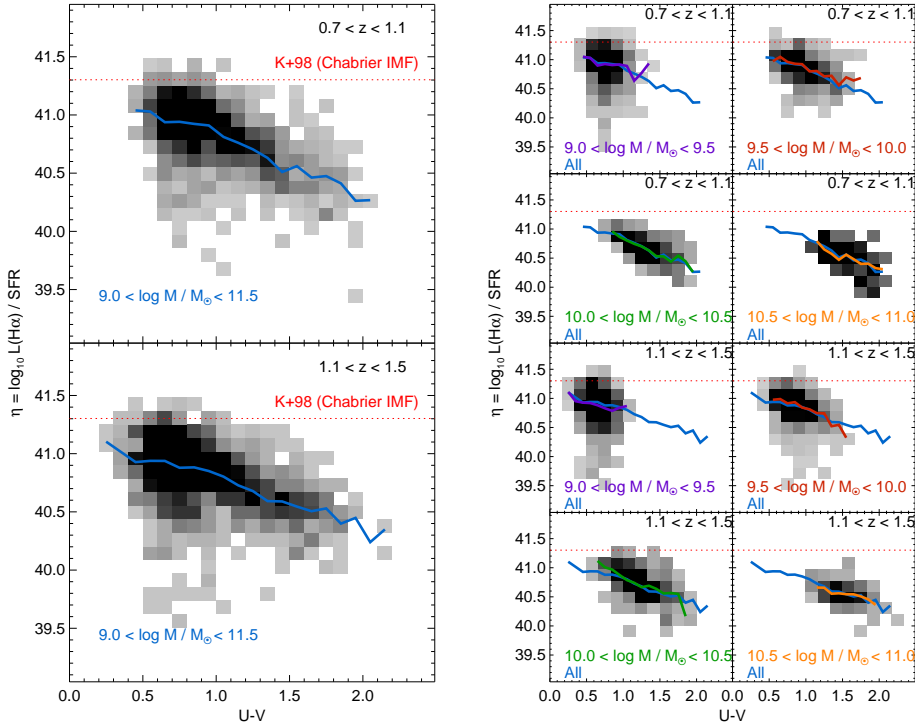


Figure 5.7: Rest Frame $U-V$ vs $\log L(H\alpha)/SFR$ for star-forming galaxies. Left: data are divided in two redshift bins (top and bottom rows). Solid blue lines represent median values through the samples in each redshift bin. Red star-forming galaxies have lower $L(H\alpha)/SFR$ than that of blue star-forming objects, indicating more dust absorption. Right: star-forming galaxies are divided into 0.5 dex wide mass bins, showing that the relation holds true also in narrower mass bins. Solid (purple, red, green, orange) lines represent the median values through the samples, and always lie on top of the median for all galaxies in the same redshift bin (blue). Star-forming galaxies with different mass but same color have on average the same $L(H\alpha)/SFR$

5.5.2 Absorption of the continuum

The dust obscuration of the continuum can be estimated from the ratio of infrared emission to ultraviolet emission, defined as $IRX = \log L(IR) / L(UV)$. In Figure 5.9, we show how IRX varies in the $U-V$ and $V-J$ color-color space: the UVJ diagram is divided in 0.1×0.1 bins and color-coded by median IRX of the galaxies in each color-color bin. For QGs, IRX is relatively low. SFGs span instead a wide range of IRX values, from ~ 0.3 to ~ 2.5 . Redder galaxies have on average higher IRX than bluer galaxies (in accordance to Whitaker et al. 2012), which implies that they have higher dust absorption in the continuum. Comparing different mass bins with each other, we notice that IRX values of galaxies in the same region of the UVJ diagram have similar IRX values in spite of the different masses.

The IRX essentially measures the attenuation in the UV. By assuming a stellar

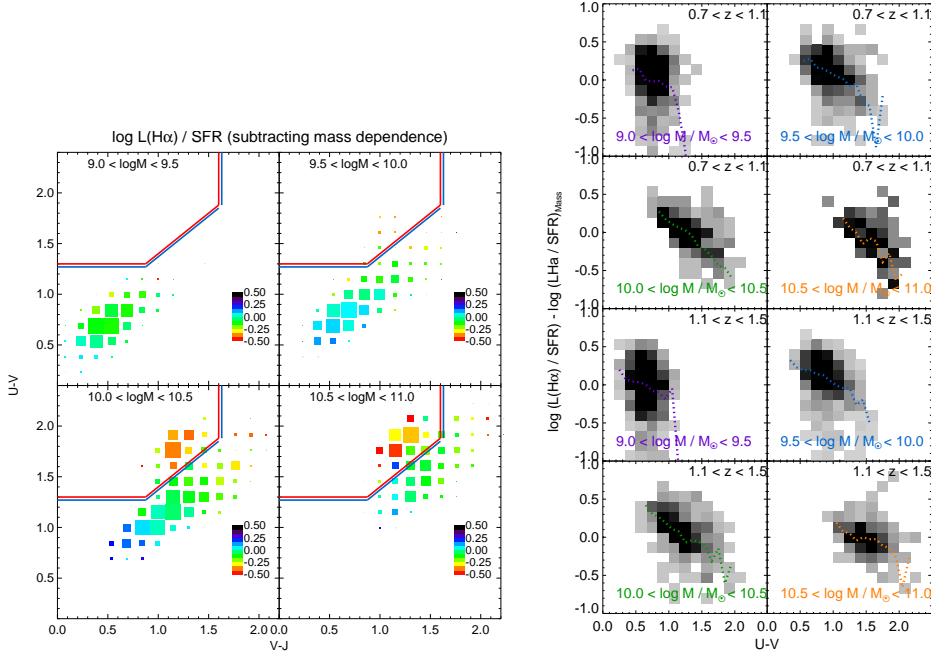


Figure 5.8: Ratio of $L(H\alpha)$ to SFR, after its mass dependence (Figure 5.5 and Equation 5.5) has been removed. Left: UVJ diagram color coded by the residual trend in $L(H\alpha)/SFR - (L(H\alpha)/SFR)_{\text{Mass}}$. Right: U-V color versus $L(H\alpha)/SFR - (L(H\alpha)/SFR)_{\text{Mass}}$. At the same mass, redder sources have a lower ratio of $H\alpha$ to SFR than bluer galaxies.

population model and an attenuation curve, we can estimate the implied attenuation of the stellar continuum around $H\alpha$. We assume a 100 Myr old stellar population from the BC03 stellar population models, with constant SFR and a Chabrier (2003) IMF, and we redden its spectrum assuming a Calzetti (2000) dust law, and varying $A(V)$ from 0 to 6, with a 0.1 step. For each value of dust reddening, we compute the flux absorbed from 0 to $1 \mu\text{m}$ and assume it is reemitted in the infrared (as in Charlot & Fall 2000)³. This provides an estimate of L_{IR} . We measure in the models the luminosity at 2800 \AA and convert it to $L(\text{UV})$ as in Bell et al. (2005): $L(\text{UV}) = 1.5 * L(2800)$. We finally compute the expected $\text{IRX} = \log L(\text{IR})/L(\text{UV})$ for each value of $A(6563)$.

For each galaxy in the sample we estimate the absorption in the continuum at 6563 \AA (A_{6563}) from its IRX value, and compare it to its absorption towards the $H\alpha$ line, evaluated in the previous Section via the $L(H\alpha)/SFR$ ratio (Figure 5.10). We observe that the $H\alpha$ emission line is more absorbed than its underlying continuum. We find $A_{H\alpha} = (1.63 \pm 0.14) * A_{6563}$, in agreement with Price et al. (2014), who evaluated the absorption around star-forming regions of 3D-HST galaxies at $z \sim 1.4$ via the Balmer decrement and the continuum A_V via SED fitting, and reported a value of 1.86 ± 0.40 . This evaluation depends on the assumption that dust obscuration of

³As the model galaxy is young, the absorbed light is dominated by that of young, blue, stars.

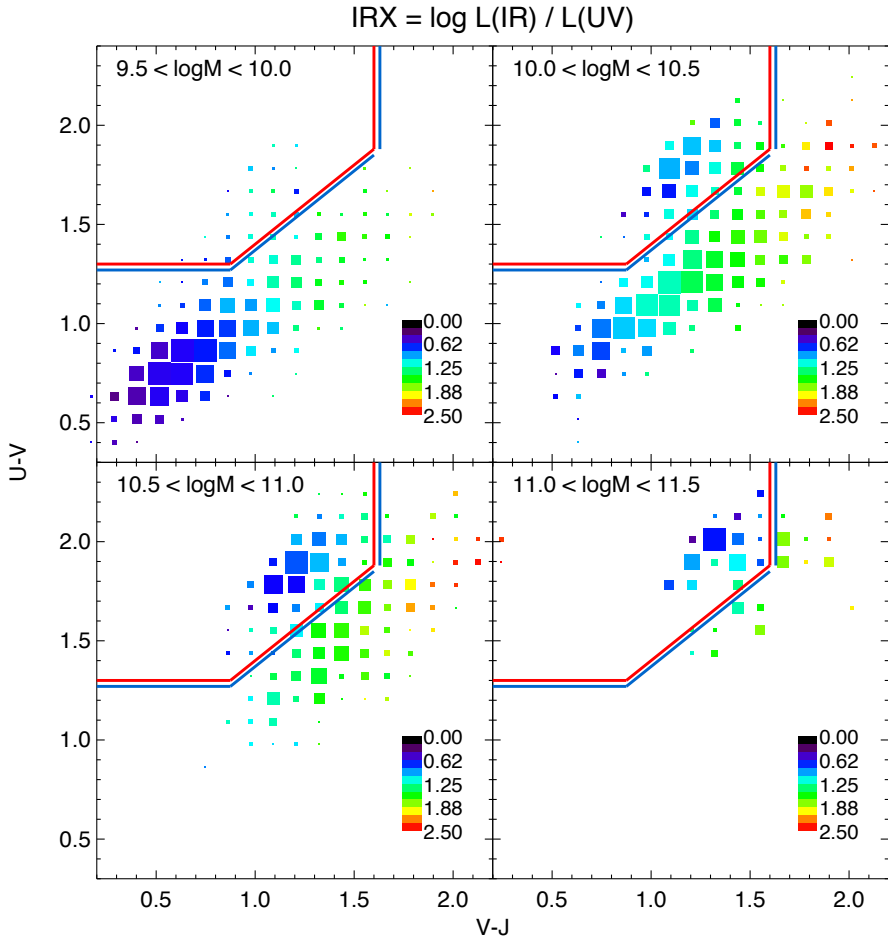


Figure 5.9: UVJ diagram for 3D-HST galaxies at $0.7 < z < 1.5$ in different mass bins, color-coded by median IRX ($\log L_{IR}/L_{UV}$). The selection box divides quiescent and star-forming galaxies. Red SFGs have a higher dust attenuation than blue SFGs. The areas of squares are proportional to the number of galaxies in that 0.1×0.1 mag color-color bin.

high-redshift galaxies follows a Calzetti law, which is currently matter of debate (see Kriek & Conroy 2013, Reddy et al. 2015).

The relation between the stellar continuum and nebular attenuation has consequences on $EW(H\alpha)$. If continuum and emission lines were extinguished by the same amount of light (as in Reddy et al. 2010 or Erb et al. 2006) $EW(H\alpha)$ would be fundamentally a dust-free measurement. However, the present study (in agreement with Kashino et al. 2013, Price et al. 2014) shows that $EW(H\alpha)$ retains a mild dependence on dust, with 1 mag of extinction in the continuum originating 0.6 mag of extinction for $EW(H\alpha)$.

Given the estimates of dust absorption in the continuum and in the $H\alpha$ line, we can finally evaluate the effect of dust onto the $EW(H\alpha)$. We estimate that, per each magnitude in U-V color, $H\alpha$ gets on average 2.5 times more absorbed (0.4 dex, Figure

5.7). Using the differential extinction between emission lines and continuum computed in this Section, $\Delta L(H\alpha) = 0.4$ dex translates into a variation of $\Delta EW(H\alpha) = 0.15$ dex per magnitude in U-V color; this is the variation of $EW(H\alpha)$ as a consequence of dust absorption only.

We check whether the full range of $EW(H\alpha)$, which amounts to a decline of 0.47 dex per each magnitude in U-V (Section 5.3), can be explained by the contributions of different dust absorption and different sSFRs (0.15-0.38 dex per magnitude in U-V as computed in Section 5.4). The impact of $\Delta sSFR$ onto $\Delta EW(H\alpha)$, even though model dependent, tends to be higher than that of different dust attenuations.

We find that the observed $\Delta EW(H\alpha)$ can be reproduced by summing the effect of dust (0.15 dex) to that of sSFR at the highest end of its determination (~ 0.35 dex), i.e. by assuming exponentially declining SFHs with short τ (~ 300 Myr). This is justified since, from best fits to the photometry (Section 2), we obtain τ values with a median value of 400 Myr^4 , with no significant trend with mass.

In summary, we show that the variation of $EW(H\alpha)$ with color can be explained by the combined effect of different dust extinctions and different sSFRs, under the assumption that SFGs have SFHs with short τ .

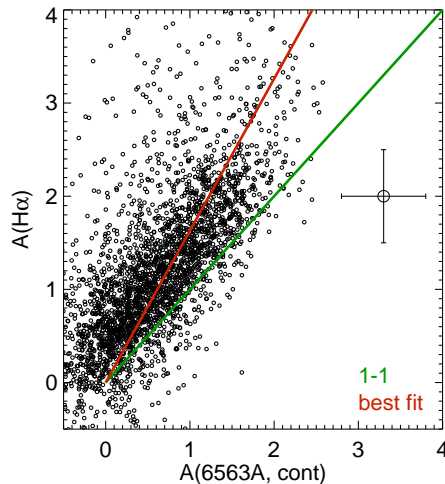


Figure 5.10: For each star-forming galaxy in the sample, relation between absorption in the continuum at 6563 \AA (as computed in Section 5.5) and that for the $H\alpha$ emission line. The $H\alpha$ emission line is more absorbed than the light in the underlying continuum. The red line represents the best fit to the data computed with a least-square minimization, corresponding to a slope of 1.63.

⁴The mean value for τ is 1 Gyr. The mean and median values for $\log(\tau/\text{yr})$ are respectively 8.6 and 8.3.

5.6 Conclusions

We have analyzed a large sample of 7000 galaxies at redshift $0.7 < z < 1.5$ from the 3D-HST survey, divided in star-forming and quiescent on the basis of the widely used UVJ rest-frame color-color criterion. We investigate how the $H\alpha$ emission varies as a function of the rest-frame colors of galaxies, and investigate the origin of its variation. The main conclusions of the study are the following:

- We confirm the effectiveness of the UVJ selection technique by demonstrating that galaxies with strong and weak $H\alpha$ are well separated in the UVJ diagram: $H\alpha$ is detected ($S/N > 3$) in $\sim 85\%$ of the UVJ-selected star-forming galaxies, while less than 20% of the UVJ-selected quiescent galaxies have an $H\alpha$ detection. While the $EW(H\alpha)$ of star-forming galaxies spans a range from ~ 20 to ~ 200 , the median $EW(H\alpha)$ of quiescent galaxies is lower than 5 \AA .
- For star-forming galaxies, $EW(H\alpha)$ has a tight relation with the U-V color of the galaxy. The average $EW(H\alpha)$ of red star-forming galaxies is 0.7 dex lower than that of blue star-forming galaxies, at a fixed mass. The trend persists in narrow mass bins, and galaxies of different masses but the same U-V color have on average the same $EW(H\alpha)$.
- At a fixed mass, the median IRX ratio ($\log L_{\text{IR}}/L_{\text{UV}}$) increases towards redder U-V colors (in accordance with Whitaker et al. 2012), while the median sSFR (UV+IR) of star-forming galaxies decreases towards redder colors.
- The ratio $L(H\alpha) / \text{SFR}$ of star-forming galaxies varies as a function of both U-V color and stellar mass, indicating higher $A(H\alpha)$ attenuation for the most massive and for the reddest galaxies. The systematic variation is approximately 1 dex with stellar mass, with an additional variation of 0.5 dex with color after the mass dependence has been removed.
- The trend of $EW(H\alpha)$ with U-V color is explained by a combination of both a lower specific star-formation rate and a higher dust absorption in red star-forming galaxies, compared to those of blue star-forming galaxies.
- By determining the extinction in $H\alpha$ and that in the continuum (under the assumption of a Calzetti dust law) we confirm previous studies indicating that the $H\alpha$ emission line is more absorbed than its underlying continuum.

We acknowledge funding from ERC grant HIGHZ no. 227749. This work is based on observations taken by the 3D-HST Treasury Program (GO 12177 and 12328) with the NASA/ESA HST, which is operated by the Association of Universities for Research in Astronomy, Inc., under NASA contract NAS5-26555.

Bibliography

- Bell, E. F., Papovich, C., Wolf, C., et al. 2005, *ApJ*, 625, 23
- Bell, E. F., van der Wel, A., Papovich, C., et al. 2012, *ApJ*, 753, 167
- Brammer, G. B., van Dokkum, P. G., & Coppi, P. 2008, *ApJ*, 686, 1503
- Brammer, G. B., Whitaker, K. E., van Dokkum, P. G., et al. 2009, *ApJL*, 706, L173
- Brammer, G. B., Whitaker, K. E., van Dokkum, P. G., et al. 2011, *ApJ*, 739, 24
- Brammer, G. B., van Dokkum, P. G., Franx, M., et al. 2012, *ApJS*, 200, 13
- Brinchmann, J., Charlot, S., White, S. D. M., et al. 2004, *MNRAS*, 351, 1151
- Bruzual, G., & Charlot, S. 2003, *MNRAS*, 344, 1000
- Calzetti, D., Armus, L., Bohlin, R. C., et al. 2000, *ApJ*, 533, 682
- Chabrier, G. 2003, *ApJL*, 586, L133
- Charlot, S., & Fall, S. M. 2000, *ApJ*, 539, 718
- Daddi, E., Cimatti, A., Renzini, A., et al. 2004, *ApJ*, 617, 746
- Damen, M., Förster Schreiber, N. M., Franx, M., et al. 2009, *ApJ*, 705, 617
- Erb, D. K., Shapley, A. E., Pettini, M., et al. 2006, *ApJ*, 644, 813
- Faber, S. M., Willmer, C. N. A., Wolf, C., et al. 2007, *ApJ*, 665, 265
- Franx, M., van Dokkum, P. G., Schreiber, N. M. F., et al. 2008, *ApJ*, 688, 770
- Fumagalli, M., Patel, S. G., Franx, M., et al. 2012, *ApJL*, 757, L22
- Fumagalli, M., Labbé, I., Patel, S. G., et al. 2014, *ApJ*, 796, 35
- Garn, T., & Best, P. N. 2010, *MNRAS*, 409, 421
- Geach, J. E., Smail, I., Best, P. N., et al. 2008, *MNRAS*, 388, 1473
- Gobat, R., Strazzullo, V., Daddi, E., et al. 2013, arXiv:1305.3576
- Gordon, K. D., Clayton, G. C., Witt, A. N., & Misselt, K. A. 2000, *ApJ*, 533, 236
- Hayward, C. C., Lanz, L., Ashby, M. L. N., et al. 2014, *MNRAS*, 445, 1598
- Karim, A., Schinnerer, E., Martínez-Sansigre, A., et al. 2011, *ApJ*, 730, 61
- Kashino, D., Silverman, J. D., Rodighiero, G., et al. 2013, *ApJL*, 777, LL8
- Kennicutt, R. C., Jr. 1998, *ARA&A*, 36, 189
- Kriek, M., van Dokkum, P. G., Labbé, I., et al. 2009, *ApJ*, 700, 221

- Kriek, M., & Conroy, C. 2013, *ApJL*, 775, L16
- Kriek, M., Shapley, A. E., Reddy, N. A., et al. 2015, *ApJS*, 218, 15
- Labbé, I., Huang, J., Franx, M., et al. 2005, *ApJL*, 624, L81
- Marchesini, D., van Dokkum, P. G., Förster Schreiber, N. M., et al. 2009, *ApJ*, 701, 1765
- Maller, A. H., Berlind, A. A., Blanton, M. R., & Hogg, D. W. 2009, *ApJ*, 691, 394
- Mendel, J. T., Saglia, R. P., Bender, R., et al. 2015, *ApJL*, 804, L4
- Muzzin, A., van Dokkum, P., Kriek, M., et al. 2010, *ApJ*, 725, 742
- Muzzin, A., Marchesini, D., Stefanon, M., et al. 2013, *ApJ*, 777, 18
- Nelson, E. J., van Dokkum, P. G., Brammer, G., et al. 2012, *ApJL*, 747, L28
- Nelson, E. J., van Dokkum, P. G., Momcheva, I., et al. 2013, *ApJL*, 763, L16
- Noeske, K. G., Weiner, B. J., Faber, S. M., et al. 2007, *ApJL*, 660, L43
- Patel, S. G., Holden, B. P., Kelson, D. D., et al. 2012, *ApJL*, 748, L27
- Price, S. H., Kriek, M., Brammer, G. B., et al. 2014, *ApJ*, 788, 86
- Reddy, N. A., Erb, D. K., Pettini, M., Steidel, C. C., & Shapley, A. E. 2010, *ApJ*, 712, 1070
- Reddy, N. A., Kriek, M., Shapley, A. E., et al. 2015, arXiv:1504.02782
- Shim, H., Chary, R.-R., Dickinson, M., et al. 2011, *ApJ*, 738, 69
- Smit, R., Bouwens, R. J., Franx, M., et al. 2012, *ApJ*, 756, 14
- Sobral, D., Best, P. N., Geach, J. E., et al. 2010, *MNRAS*, 404, 1551
- Speagle, J. S., Steinhardt, C. L., Capak, P. L., & Silverman, J. D. 2014, *ApJS*, 214, 15
- Stark, D. P., Schenker, M. A., Ellis, R., et al. 2013, *ApJ*, 763, 129
- Straatman, C. M. S., Labbé, I., Spitler, L. R., et al. 2014, *ApJL*, 783, L14
- Utomo, D., Kriek, M., Labbé, I., Conroy, C., & Fumagalli, M. 2014, *ApJL*, 783, L30
- van Dokkum, P. G., Brammer, G., Fumagalli, M., et al. 2011, *ApJL*, 743, L15
- Whitaker, K. E., van Dokkum, P. G., Brammer, G., & Franx, M. 2012, *ApJL*, 754, L29
- Whitaker, K. E., van Dokkum, P. G., Brammer, G., et al. 2013, *ApJL*, 770, L39
- Whitaker, K. E., Franx, M., Leja, J., et al. 2014, *ApJ*, 795, 104
- Williams, R. J., Quadri, R. F., Franx, M., van Dokkum, P., & Labbé, I. 2009, *ApJ*, 691, 1879
- Wuyts, S., Labbé, I., Schreiber, N. M. F., et al. 2008, *ApJ*, 682, 985
- Wuyts, S., Labbé, I., Franx, M., et al. 2007, *ApJ*, 655, 51

SAMENVATTING

Aan het begin van de negentiende eeuw, was het nog onduidelijk of de Melkweg, de zwakke streep van sterren die zichtbaar is aan de hemel op een donkere, heldere nacht, het enige sterrenstelsel in het heelal is. Op 26 april 1920, bediscussieerden twee invloedrijke astronomen van de tijd, Harlow Shapley en Heber Curtis, hun tegengestelde standpunten voor een publiek in het 'Smithsonian Museum of Natural History' in Washington DC. Shapley betoogde dat de Melkweg het gehele heelal is en dat spiraalnevels deel uit maken van ons eigen melkwegstelsel. Aan de andere kant dacht Curtis dat Andromeda en de andere nevels afzonderlijke sterrenstelsels waren oftewel eiland universums (zoals Immanuel Kant ze genoemd heeft honderd jaar eerder).

De standpunten van beide geleerden werden gesteund door verschillende waarnemingen die destijds beschikbaar waren. Echter, de belangrijkste observationele ondersteuning van Shapley's theorie bleek al snel onjuist te zijn. Tegelijkertijd bleek uit nieuwe waarnemingen van Edwin Hubble dat het Andromeda sterrenstelsel een apart eiland universum was, ver buiten de Melkweg. Een paar jaar later in 1927, was het weer Hubble die een ruwe evenredigheid vond tussen de afstand tot sterrenstelsels en hun terugwijkende snelheid: hierna begonnen astronomen te beseffen dat het heelal uitdijt. De waarnemingen van Edwin Hubble markeerden het begin van de moderne observationele kosmologie; het is niet bij toeval geweest dat de meest ambitieuze ruimtetelescoop, die in een baan om de aarde zit, vernoemd is naar hem.

De opmerkelijke diversiteit van sterrenstelsels

Sinds de vroegste waarnemingen is er een grote diversiteit in de morfologie van sterrenstelsels geconstateerd. Het meest gebruikte indelingssysteem vandaag de dag, is voorgesteld door (wederom) Edwin Hubble. Hubble merkte op dat sterrenstelsels ruwweg kunnen worden ingedeeld in twee klassen: elliptische stelsels bestaande uit een ronde of elliptische verdeling van licht, en spiraalstelsels die bestaan uit een platte schijf met spiraalvormige structuur en in het centrum een concentratie van licht (beter bekend als de bulge).

Daaropvolgende studies hebben aangetoond dat de morfologie van huidige stelsels nauw gecorreleerd is met andere eigenschappen, zoals de massa, de kleur en de omgeving van de sterrenstelsels. In het algemeen hebben elliptische sterrenstelsels rodere kleuren dan spiraal stelsels, omdat hun licht wordt gedomineerd door rode oude sterren. Aan de andere kant worden in spiraal stelsels actief nieuwe, jonge sterren gevormd, en daarom lijken ze blauw. Zeer weinig sterrenstelsels liggen tussen die twee categorieën.

Een soortgelijke bimodaliteit in kleur, stervormingssnelheid, en morfologie van sterrenstelsels is ook waargenomen als men terug kijkt in de tijd naar het vroege heelal (m.a.w. bij hoge roodverschuiving).

Voor sterrenstelsels met veel stervorming, zijn de massa en de stervormingssnelheid (d.w.z. het aantal nieuwe sterren gevormd in een jaar) strak gecorreleerd. Meer massieve sterrenstelsels vormen meer sterren per jaar. Als we terug kijken in de tijd, zien we dezelfde relatie voor sterrenstelsels op hoge roodverschuiving. De absolute stervormingssnelheid neemt toe met roodverschuiving: d.w.z. sterrenstelsels van dezelfde massa hadden in het verleden een hogere stervormingssnelheid.

Problemen bij waarnemingen op hoge roodverschuiving

Ondanks de onvoorstelbare technologische vooruitgang van telescopen en instrumenten in de laatste twintig jaar, zijn metingen van sterrenstelsels op hoge roodverschuiving nog steeds erg uitdagend. Onze kennis van deze stelsels komt niet in de buurt van onze kennis van de lokale melkwegstelsels. Ten eerste komt dit doordat het licht van sterrenstelsels zwakker wordt naar mate de afstand tot het stelsel toeneemt. Om de fysische parameters van sterrenstelsels nauwkeuriger te meten, verdelen astronomen het licht in meerdere frequenties met een spectrograaf. Een spectrograaf kun je vergelijken met een prisma dat wit licht splitst in verschillende kleuren. Met uitzondering van de helderste bronnen, is spectroscopie van verre, zwakke, sterrenstelsels een buitengewoon tijdrovend proces. Het meest fundamentele probleem als de spectroscopische methode niet toegepast kan worden, is dat afstandsbepalingen erg onzeker worden.

Een tweede fundamentele probleem voor waarnemingen op hoge roodverschuiving is dat het licht sterk roodverschoven is door de uitdijning van het heelal. Dit fenomeen is verwant aan de frequentie van geluid dat naar een lagere toonhoogte gaat als de bron van ons af beweegt. Licht van oude sterren (die het merendeel van de totale massa beslaan in de meeste sterrenstelsels) wordt verplaatst naar het infrarood voor sterrenstelsels die op een afstand staan van meer dan een paar miljard lichtjaar. Op die golflengtes is de atmosfeer niet transparant. Waarnemingen met telescopen vanaf de grond (in plaats van telescopen op satellieten) zijn alleen mogelijk in bepaalde bereiken van golflengtes.

Onze kennis van leeftijden, stervormingssnelheden en metaalgehaltes van sterrenstelsels is vaak gebaseerd op spectrale indicatoren uit optische golflengtes. Het is uitdagend en tijdrovend om deze te meten op hoge roodverschuiving wanneer ze verschoven zijn naar het infrarood. Bijvoorbeeld, een goed gekalibreerde standaard indicator van de stervormingssnelheid is de waterstof emissie lijn: alleen jonge sterren hebben licht met genoeg energie om een belangrijke bijdrage leveren aan de ionisatie van het waterstof in hun directe omgeving: waterstof lijnen bieden een bijna directe meting van de stervormingssnelheid. Als gevolg van de verschuiving van het licht naar het (nabije) infrarood voor stelsels die ouder zijn dan 8 miljard jaar, maken studies van de evolutie van stervormingssnelheden met een breed roodverschuivingsbereik gebruik van een reeks van indicatoren voor de stervormingssnelheid die gebaseerd zijn op een verschillende veronderstellingen en inter-kalibraties. Voor elke indicator, een flux die overeenkomt met een stervormingssnelheid van

10-20 zonsmassa's per jaar is een uitdaging, zo niet onmogelijk voor afzonderlijke bronnen.

De identificatie van collecties van sterrenstelsels met lage stervormingssnelheden op hoge roodverschuiving is daarom in het algemeen uitsluitend gebaseerd op de kleuren van het stelsel. Dit wordt gedaan door het selecteren van sterrenstelsels waarvan het optische en nabij-infrarode licht wordt gedomineerd door een oude sterren.

Een extra complicatie voor spectroscopie van de grond is dat spectroscopische collecties geoptimaliseerd zijn voor waarnemingen in specifieke bandbreedtes. Over het algemeen bestaan ze daarom slechts uit blauwe objecten die veel stervorming bevatten. Aan de andere kant kunnen waarnemingen die niet gebaseerd zijn op emissie lijnen, maar op het continuüm van het licht, slechts toegepast worden op kleine collecties van heldere objecten. Deze biases beperken ons kennis van de fysische eigenschappen van sterrenstelsels zoals leeftijd en metaalgehalte. Bovendien beperken ze ons begrip van de vormingsgeschiedenis en de evolutie van sterrenstelsels.

Dit proefschrift

Dit proefschrift richt zich op een aantal van de eerder beschreven problemen. In het bijzonder maken wij gebruik van een nieuwe reeks waarnemingen met de Wide Field Camera 3 (WFC3) grism (tralie prisma) aan boord van de Hubble Space Telescope (HST), in het kader van het 3D-HST onderzoek. Dit onderzoek richt zich op de evolutie van de stervormingssnelheden, de sterke van emissie lijnen en eigenschappen van groepen sterren van zowel stervormings- als passieve sterrenstelsels, in collecties van sterrenstelsels tot 10 miljard jaar geleden, toen de stervormingssnelheid van het heelal op zijn piek was en de structurele regelmaat die we vandaag de dag zien in sterrenstelsels ontstaan moet zijn. Omdat de WFC3 grism gelijktijdig alle objecten in een veld waarneemt, zijn de waarnemingen niet beïnvloed door de biases voor spectroscopie vanaf de grond, en bieden ze een mogelijkheid om afstanden te meten voor zowel stervormingsgebieden als passieve sterrenstelsels.

In hoofdstuk 2, combineren we de eerste gegevens van het 3D-HST onderzoek met die van waarnemingen vanaf de grond op lagere roodverschuiving, om de evolutie van de helderste waterstof lijn ($H\alpha$) te bestuderen. In het bijzonder meten we de equivalente breedte van de $H\alpha$ -lijn ($EW(H\alpha)$). Dat is de verhouding van de helderheid van $H\alpha$ en de onderliggende stellaire helderheid. De equivalente breedte is een maat voor de verhouding tussen de huidige stervormingssnelheid en die in het verleden. We vinden dat op elk cosmisch tijdstip $EW(H\alpha)$ afneemt met de massa van het sterrenstelsel, en dat bij constante massa $EW(H\alpha)$ toeneemt met roodverschuiving (m.a.w. verder terug in de tijd). Deze evolutie is onafhankelijk van de massa in sterren, en het hangt sterker af van roodverschuiving dat tot nu toe aangenomen werd en voorspeld werd door theoretische modellen van de evolutie van sterrenstelsels. Daarnaast voorspellen we de evolutie van $EW(H\alpha)$ op

hoge roodverschuiving; bijdrage van emissie lijnen voor sterrenstelsels op roodverschuivingen van $z = 4 - 8$ blijft toenemen. Dit heeft belangrijke consequenties voor spectroscopie en fotometrie van bronnen die waargenomen zullen worden met de James Webb Space Telescope.

In hoofdstuk 3, onderzoeken we de stervormingssnelheden van passieve sterrenstelsels die geselecteerd zijn op basis van hun optische en nabij infrarode spectrale energie verdeling, die wijzen op een oude stellaire populatie. Voorgaande metingen van de spectrale energie verdeling voor optisch geselecteerde passieve stelsels, wijzen op nog lagere stervormingssnelheden dan verwacht op basis van het hergebruiken van gas (onder de aanname dat sterren gevormd worden uit massa verloren door geëvolueerde sterren). Echter, deze meting mist stervorming als deze verborgen wordt door extinctie door stof. Hierdoor wordt de optische straling niet waargenomen, maar verschuift de straling naar het mid-infrarood. In hoofdstuk 3, selecteren we daarom spectroscopisch bevestigde passieve sterrenstelsels in het 3D-HST onderzoek, en meten hun extinctie door stof stervormingssnelheid door gestapelde mid-infrarode fluxes van *Spitzer-24* μm voor verschillende cosmische tijdstippen. We tonen aan dat, voor elk kosmisch tijdstip, de stervormingssnelheid van passieve sterrenstelsels 20-40 keer lager ligt dan voor sterrenstelsels die nog actief sterren vormen op dezelfde roodverschuiving. Dit geeft aan dat het uitdoven van stervorming erg efficiënt is, zelfs in het jonge heelal waar de typische stervormingssnelheden honderden zonsmassa's per jaar bereiken, in vergelijking met 1-4 zonsmassa per jaar voor de Melkweg. De daadwerkelijke stervormingssnelheid van passieve sterrenstelsels kan zelfs nog lager zijn, omdat we laten zien dat de mid-infrarode flux ook van andere processen dan stervorming kan afkomen, zoals bv. circumstellair stof and opwarming van stof door oude stellaire populaties.

Hoofdstuk 4 richt zich op de spectra van passieve en actieve sterrenstelsels op roodverschuivingen van $z = 0.5$ tot $z = 2$ met als doel de stellaire leeftijden te bepalen. We stapelen spectra van stervormings- and passieve stelsels, die geselecteerd zijn op basis van een kleur-kleur techniek, en vergelijken ze met veelgebruikte modellen van synthetische stellaire populaties. We vinden dat stellaire populatie modellen goed passen bij waarnemingen op golflengtes lager dan 6500\AA , terwijl ze systematische afwijkingen op rodere golflengtes. Wij bevestigen dat passieve sterrenstelsels zwakke emissie lijnen hebben. Dit is in overeenstemming met metingen van de stervormingssnelheden in het mid-infrarood. De leeftijden van passieve sterrenstelsels hangen af van het gebruikte model, maar in het algemeen zijn passieve sterrenstelsels jong, m.a.w. jonger dan de helft van de leeftijd van het heelal op elk kosmisch tijdstip. Voor stervormings-stelsels hangt de gemeten leeftijd sterk af van het gebruikte stellaire populatie model en de evolutie van de stervorming.

In hoofdstuk 5 maken we gebruik van de volledige 3D-HST data om te analyseren hoe waterstof emissie afhangt van de eigenschappen van sterrenstelsels, in het bijzonder de optische en nabij infrarode spectrale energie verdeling van het licht, in het bereik van roodverschuiving waar $\text{H}\alpha$ kan worden waargenomen met de HST

en WFC3 grism ($0.7 < z < 1.5$). We laten zien dat sterrenstelsels met sterke en zwakke $H\alpha$ goed van elkaar te scheiden zijn in een kleur-kleur diagram. Voor sterrenstelsels met actieve stervorming, onderzoeken we hoe $H\alpha$ afhangt van de kleuren van het sterrenstelsel en de specifieke stervormingssnelheid (stervormingssnelheid per totale stellaire massa), gemeten in het ultraviolet en mid-infrarood. Bij constante massa van het sterrenstelsel, hebben rode stervormings stelsels een lagere $EW(H\alpha)$ dan blauwe stervormings stelsels. We tonen ook aan dat bij constante massa, de mediaan van de specifieke stervormingssnelheid afneemt als de U-V kleuren roder worden, en dat absorptie door stof toeneemt voor rodere kleuren. We laten zien dat in het algemeen de kleur-afhankelijkheid van $EW(H\alpha)$ verklaard kan worden door zowel een lagere specifieke stervormingssnelheid als een hogere mate van absorptie door stof in sterrenstelsels met rodere kleuren.

PUBLICATIONS

1. *H α Equivalent Widths from the 3D-HST Survey: Evolution with Redshift and Dependence on Stellar Mass*
Fumagalli, Mattia; Patel, Shannon G.; Franx, Marijn; Brammer, Gabriel; van Dokkum, Pieter; da Cunha, Elisabete; Kriek, Mariska; Lundgren, Britt; Momcheva, Ivelina; Rix, Hans-Walter; Schmidt, Kasper B.; Skelton, Rosalind E.; Whitaker, Katherine E.; Labbe, Ivo; Nelson, Erica
The Astrophysical Journal Letters, Volume 757, Issue 2, article id. L22, 6 pp. (2012)
2. *How dead are dead Galaxies? Mid-Infrared fluxes of quiescent galaxies at $0.3 < z < 2.5$: implications for star formation rates and dust heating*
Fumagalli, Mattia; Labbe, Ivo; Patel, Shannon G.; Franx, Marijn; Van Dokkum, Pieter, Brammer, Gabriel; da Cunha, Elisabete; Kriek, Mariska; Lundgren, Britt; Momcheva, Ivelina; Rix, Hans-Walter; Schmidt, Kasper B.; Skelton, Rosalind E.; Whitaker, Katherine E.; Nelson, Erica June, Ryan F. Quadri
The Astrophysical Journal, Volume 796, Issue 1, article id. 35, pp. (2014).
3. *Ages of massive galaxies at $0.5 < z < 2.0$ from 3D-HST rest-frame optical spectroscopy*
Fumagalli, Mattia; Franx, Marijn; van Dokkum, Pieter; Whitaker, Katherine E.; Skelton, Rosalind E.; Brammer, Gabriel; Nelson, Erica; Maseda, Micheal; Momcheva, Ivelina; Labbé, Ivo; Lundgren, Brit; Rix, Hans-Walter
Submitted to The Astrophysical Journal
4. *Decreasing H α for redder star-forming galaxies: influence of dust and star formation rates*
Fumagalli, Mattia; Franx, Marijn; Labbé, Ivo; van Dokkum, Pieter; Kriek, Mariska; Skelton, Rosalind E.; Whitaker, Katherine E.; Brammer, Gabriel; Momcheva, Momcheva
Submitted to The Astrophysical Journal
5. *The structural evolution of Milky Way like star forming galaxies since $z \sim 1.3$*
Patel, Shannon G.; **Fumagalli, Mattia**; Franx, Marijn; van Dokkum, Pieter G.; van der Wel, Arjen; Leja, Joel; Labbé, Ivo; Brammer, Gabriel; Skelton, Rosalind E.; Momcheva, Ivelina; Whitaker, Katherine E.; Lundgren, Britt; Muzzin, Adam; Quadri, Ryan F.; Nelson, Erica June; Wake, David A.; Rix, Hans-Walter
The Astrophysical Journal Volume 778 Number 2 ApJ 778 115
6. *First Results from the 3D-HST Survey: The Striking Diversity of Massive Galaxies at $z > 1$*
van Dokkum, Pieter G.; Brammer, Gabriel; **Fumagalli, Mattia**; Nelson, Erica; Franx, Marijn; Rix, Hans-Walter; Kriek, Mariska; Skelton, Rosalind E.; Patel, Shannon; Schmidt, Kasper B.; Bezanson, Rachel; Bian, Fuyan; da Cunha, Elisabete; Erb, Dawn K.; Fan, Xiaohui; Förster Schreiber, Natascha; Illingworth,

- Garth D.; Labbé, Ivo; Lundgren, Britt; Magee, Dan; Marchesini, Danilo; McCarthy, Patrick; Muzzin, Adam; Quadri, Ryan; Steidel, Charles C.; Tal, Tomer; Wake, David; Whitaker, Katherine E.; Williams, Anna
The Astrophysical Journal Letters, Volume 743, Issue 1, article id. L15, 6 pp. (2011).
7. *Spatially Resolved H α Maps and Sizes of 57 Strongly Star-forming Galaxies at $z = 1$ from 3D-HST: Evidence for Rapid Inside-out Assembly of Disk Galaxies*
Nelson, Erica June; van Dokkum, Pieter G.; Brammer, Gabriel; Förster Schreiber, Natascha; Franx, Marijn; **Fumagalli, Mattia**; Patel, Shannon; Rix, Hans-Walter; Skelton, Rosalind E.; Bezanson, Rachel; Da Cunha, Elisabete; Kriek, Mariska; Labbe, Ivo; Lundgren, Britt; Quadri, Ryan; Schmidt, Kasper B.
The Astrophysical Journal Letters, Volume 747, Issue 2, article id. L28, 6 pp. (2012).
8. *3D-HST: A Wide-field Grism Spectroscopic Survey with the Hubble Space Telescope*
Brammer, Gabriel B.; van Dokkum, Pieter G.; Franx, Marijn; **Fumagalli, Mattia**; Patel, Shannon; Rix, Hans-Walter; Skelton, Rosalind E.; Kriek, Mariska; Nelson, Erica; Schmidt, Kasper B.; Bezanson, Rachel; da Cunha, Elisabete; Erb, Dawn K.; Fan, Xiaohui; Förster Schreiber, Natascha; Illingworth, Garth D.; Labbé, Ivo; Leja, Joel; Lundgren, Britt; Magee, Dan; Marchesini, Danilo; McCarthy, Patrick; Momcheva, Ivelina; Muzzin, Adam; Quadri, Ryan; Steidel, Charles C.; Tal, Tomer; Wake, David; Whitaker, Katherine E.; Williams, Anna
The Astrophysical Journal Supplement, Volume 200, Issue 2, article id. 13, 19 pp. (2012).
9. *3D-HST Grism Spectroscopy of a Gravitationally Lensed, Low-metallicity Starburst Galaxy at $z = 1.847$*
Brammer, Gabriel B.; Sanchez-Janssen, Rubén; Labbé, Ivo; da Cunha, Elisabete; Erb, Dawn K.; Franx, Marijn; **Fumagalli, Mattia**; Lundgren, Britt; Marchesini, Danilo; Momcheva, Ivelina; Nelson, Erica; Patel, Shannon; Quadri, Ryan; Rix, Hans-Walter; Skelton, Rosalind E.; Schmidt, Kasper B.; van der Wel, Arjen; van Dokkum, Pieter G.; Wake, David A.; Whitaker, Katherine E.
The Astrophysical Journal Letters, Volume 758, Issue 1, article id. L17, 7 pp. (2012).
10. *Large-scale Star-formation-driven Outflows at $1 < z < 2$ in the 3D-HST Survey*
Lundgren, Britt F.; Brammer, Gabriel; van Dokkum, Pieter; Bezanson, Rachel; Franx, Marijn; **Fumagalli, Mattia**; Momcheva, Ivelina; Nelson, Erica; Skelton, Rosalind E.; Wake, David; Whitaker, Katherine; da Cunha, Elizabeth; Erb, Dawn K.; Fan, Xiaohui; Kriek, Mariska; Labbé, Ivo; Marchesini, Danilo; Patel, Shannon; Rix, Hans Walter; Schmidt, Kasper; van der Wel, Arjen
The Astrophysical Journal, Volume 760, Issue 1, article id. 49, 13 pp. (2012).
11. *The Radial Distribution of Star Formation in Galaxies at $z = 1$ from the 3D-HST Survey*
Nelson, Erica June; van Dokkum, Pieter G.; Momcheva, Ivelina; Brammer,

- Gabriel; Lundgren, Britt; Skelton, Rosalind E.; Whitaker, Katherine E.; Da Cunha, Elisabete; Förster Schreiber, Natascha; Franx, Marijn; **Fumagalli, Mattia**; Kriek, Mariska; Labbe, Ivo; Leja, Joel; Patel, Shannon; Rix, Hans-Walter; Schmidt, Kasper B.; van der Wel, Arjen; Wuyts, Stijn
The Astrophysical Journal Letters, Volume 763, Issue 1, article id. L16, 6 pp. (2013).
12. *Quiescent Galaxies in the 3D-HST Survey: Spectroscopic Confirmation of a Large Number of Galaxies with Relatively Old Stellar Populations at $z \sim 2$*
Whitaker, Katherine E.; van Dokkum, Pieter G.; Brammer, Gabriel; Momcheva, Ivelina G.; Skelton, Rosalind; Franx, Marijn; Kriek, Mariska; Labbé, Ivo; **Fumagalli, Mattia**; Lundgren, Britt F.; Nelson, Erica J.; Patel, Shannon G.; Rix, Hans-Walter
The Astrophysical Journal Letters, Volume 770, Issue 2, article id. L39, 6 pp. (2013).
13. *The spatial extent and distribution of star formation in 3D-HST mergers at $z \sim 1.5$*
Schmidt, Kasper B.; Rix, Hans-Walter; da Cunha, Elisabete; Brammer, Gabriel B.; Cox, Thomas J.; van Dokkum, Pieter; Förster Schreiber, Natascha M.; Franx, Marijn; **Fumagalli, Mattia**; Jonsson, Patrik; Lundgren, Britt; Maseda, Michael V.; Momcheva, Ivelina; Nelson, Erica J.; Skelton, Rosalind E.; van der Wel, Arjen; Whitaker, Katherine E.
Monthly Notices of the Royal Astronomical Society, Volume 432, Issue 1, p.285-300
14. *The Assembly of Milky-Way-like Galaxies Since $z \sim 2.5$*
van Dokkum, Pieter G.; Leja, Joel; Nelson, Erica June; Patel, Shannon; Skelton, Rosalind E.; Momcheva, Ivelina; Brammer, Gabriel; Whitaker, Katherine E.; Lundgren, Britt; **Fumagalli, Mattia**; Conroy, Charlie; Förster Schreiber, Natascha; Franx, Marijn; Kriek, Mariska; Labbé, Ivo; Marchesini, Danilo; Rix, Hans-Walter; van der Wel, Arjen; Wuyts, Stijn
The Astrophysical Journal Letters, Volume 771, Issue 2, article id. L35, 7 pp. (2013).
15. *Confirmation of Small Dynamical and Stellar Masses for Extreme Emission Line Galaxies at $z \sim 2$*
Maseda, Michael V.; van der Wel, Arjen; da Cunha, Elisabete; Rix, Hans-Walter; Pacifici, Camilla; Momcheva, Ivelina; Brammer, Gabriel B.; Franx, Marijn; van Dokkum, Pieter; Bell, Eric F.; **Fumagalli, Mattia**; Grogan, Norman A.; Kocevski, Dale D.; Koekemoer, Anton M.; Lundgren, Britt F.; Marchesini, Danilo; Nelson, Erica J.; Patel, Shannon G.; Skelton, Rosalind E.; Straughn, Amber N.; Trump, Jonathan R.; Weiner, Benjamin J.; Whitaker, Katherine E.; Wuyts, Stijn
The Astrophysical Journal Letters, Volume 778, Issue 1, article id. L22, 5 pp. (2013).
16. *A CANDELS-3D-HST synergy: Resolved Star Formation Patterns at $0.7 < z < 1.5$*
Wuyts, Stijn; Förster Schreiber, Natascha M.; Nelson, Erica J.; van Dokkum,

- Pieter G.; Brammer, Gabe; Chang, Yu-Yen; Faber, Sandra M.; Ferguson, Henry C.; Franx, Marijn; **Fumagalli, Mattia**; Genzel, Reinhard; Grogin, Norman A.; Kocevski, Dale D.; Koekemoer, Anton M.; Lundgren, Britt; Lutz, Dieter; McGrath, Elizabeth J.; Momcheva, Ivelina; Rosario, David; Skelton, Rosalind E.; Tacconi, Linda J.; van der Wel, Arjen; Whitaker, Katherine E.
The Astrophysical Journal, Volume 779, Issue 2, article id. 135, 16 pp. (2013).
17. *Simultaneous Modeling of the Stellar and Dust Emission in Distant Galaxies: Implications for Star Formation Rate Measurements*
Utomo, Dyas; Kriek, Mariska; Labbé, Ivo; Conroy, Charlie; **Fumagalli, Mattia**
The Astrophysical Journal Letters, Volume 783, Issue 2, article id. L30, 6 pp. (2014).
18. *3D-HST+CANDELS: The Evolution of the Galaxy Size-Mass Distribution since $z = 3$*
van der Wel, A.; Franx, M.; van Dokkum, P. G.; Skelton, R. E.; Momcheva, I. G.; Whitaker, K. E.; Brammer, G. B.; Bell, E. F.; Rix, H.-W.; Wuyts, S.; Ferguson, H. C.; Holden, B. P.; Barro, G.; Koekemoer, A. M.; Chang, Yu-Yen; McGrath, E. J.; Haussler, B.; Dekel, A.; Behroozi, P.; Fumagalli, M.; Leja, J.; Lundgren, B. F.; Maseda, M. V.; Nelson, E. J.; Wake, D. A.; Patel, S. G.; Labbé, I.; Faber, S. M.; Grogin, N. A.; Kocevski, D. D.
The Astrophysical Journal, Volume 788, Issue 1, article id. 28, 19 pp. (2014).
19. *Direct Measurements of Dust Attenuation in $z \sim 1.5$ Star-forming Galaxies from 3D-HST: Implications for Dust Geometry and Star Formation Rates*
Price, Sedona H.; Kriek, Mariska; Brammer, Gabriel B.; Conroy, Charlie; Förster Schreiber, Natascha M.; Franx, Marijn; **Fumagalli, Mattia**; Lundgren, Britt; Momcheva, Ivelina; Nelson, Erica J.; Skelton, Rosalind E.; van Dokkum, Pieter G.; Whitaker, Katherine E.; Wuyts, Stijn
The Astrophysical Journal, Volume 788, Issue 1, article id. 86, 13 pp. (2014).
20. *The Nature of Extreme Emission Line Galaxies at $z = 1-2$: Kinematics and Metallicities from Near-infrared Spectroscopy*
Maseda, Michael V.; van der Wel, Arjen; Rix, Hans-Walter; da Cunha, Elisabete; Pacifici, Camilla; Momcheva, Ivelina; Brammer, Gabriel B.; Meidt, Sharon E.; Franx, Marijn; van Dokkum, Pieter; **Fumagalli, Mattia**; Bell, Eric F.; Ferguson, Henry C.; Förster-Schreiber, Natascha M.; Koekemoer, Anton M.; Koo, David C.; Lundgren, Britt F.; Marchesini, Danilo; Nelson, Erica J.; Patel, Shannon G.; Skelton, Rosalind E.; Straughn, Amber N.; Trump, Jonathan R.; Whitaker, Katherine E.
The Astrophysical Journal, Volume 791, Issue 1, article id. 17, 17 pp. (2014).
21. *Dense Cores in Galaxies Out to $z = 2.5$ in SDSS, UltraVISTA, and the Five 3D-HST/CANDELS Fields*
van Dokkum, Pieter G.; Bezanson, Rachel; van der Wel, Arjen; Nelson, Erica June; Momcheva, Ivelina; Skelton, Rosalind E.; Whitaker, Katherine E.; Brammer, Gabriel; Conroy, Charlie; Förster Schreiber, Natascha M.; **Fumagalli, Mattia**; Kriek, Mariska; Labbé, Ivo; Leja, Joel; Marchesini, Danilo; Muzzin, Adam;

- Oesch, Pascal; Wuyts, Stijn
The Astrophysical Journal, Volume 791, Issue 1, article id. 45, 18 pp. (2014).
22. *3D-HST WFC3-selected Photometric Catalogs in the Five CANDELS/3D-HST Fields: Photometry, Photometric Redshifts, and Stellar Masses*
Skelton, Rosalind E.; Whitaker, Katherine E.; Momcheva, Ivelina G.; Brammer, Gabriel B.; van Dokkum, Pieter G.; Labbé, Ivo; Franx, Marijn; van der Wel, Arjen; Bezanson, Rachel; Da Cunha, Elisabete; **Fumagalli, Mattia**; Förster Schreiber, Natascha; Kriek, Mariska; Leja, Joel; Lundgren, Britt F.; Magee, Daniel; Marchesini, Danilo; Maseda, Michael V.; Nelson, Erica J.; Oesch, Pascal; Pacifici, Camilla; Patel, Shannon G.; Price, Sedona; Rix, Hans-Walter; Tal, Tomer; Wake, David A.; Wuyts, Stijn
The Astrophysical Journal Supplement, Volume 214, Issue 2, article id. 24, 49 pp. (2014).
23. *Constraining the Low-mass Slope of the Star Formation Sequence at $0.5 < z < 2.5$*
Whitaker, Katherine E.; Franx, Marijn; Leja, Joel; van Dokkum, Pieter G.; Henry, Alaina; Skelton, Rosalind E.; **Fumagalli, Mattia**; Momcheva, Ivelina G.; Brammer, Gabriel B.; Labbé, Ivo; Nelson, Erica J.; Rigby, Jane R.
The Astrophysical Journal, Volume 795, Issue 2, article id. 104, 20 pp. (2014).
24. *On the importance of using appropriate spectral models to derive physical properties of galaxies at $0.7 < z < 2.8$*
Pacifici, Camilla; da Cunha, Elisabete; Charlot, Stéphane; Rix, Hans-Walter; **Fumagalli, Mattia**; Wel, Arjen van der; Franx, Marijn; Maseda, Michael V.; van Dokkum, Pieter G.; Brammer, Gabriel B.; Momcheva, Ivelina; Skelton, Rosalind E.; Whitaker, Katherine; Leja, Joel; Lundgren, Britt; Kassin, Susan A.; Yi, Sukyoung K.
Monthly Notices of the Royal Astronomical Society, Volume 447, Issue 1, p.786-805

CURRICULUM VITAE

I was born on June the 12th, 1986, in Lecco, on the shores of Lake Como in Northern Italy. I grew up in the small town of Morbegno, in the Valtellina valley on the Alps, where I attended elementary, middle, and high school, all within 500m from my house. In high school, at the Scientific Lyceum “Pierluigi Nervi”, I became fond of natural and physical sciences.

In the fall of 2005, I moved to Milan to pursue a Bachelor Degree in Physics at the University of Milano-Bicocca. I graduated from my Bachelor’s with a research project on the calibration of the CMS-ECAL detector at the Large Hadron Collider, partially completed during a Summer School at CERN, Geneva, under the guidance of Prof. Marco Paganoni and Dr. Pietro Govoni. Despite the fact that I later changed my field of research, it was during that summer that I became passionate about the academic research environment and decided I wanted to continue with a research based education. In October 2008 I enrolled in the Master’s in Astrophysics and Space Physics at the University of Milano-Bicocca. During that time I was lucky enough to join observing trips at the 150cm telescope of Loiano (Italy) and to the 2.1m of San Pedro Martir (Mexico), which made me passionate about observational Astronomy. I graduated with a research project on the environmental effects on galaxies in the local Universe, with Prof. Giuseppe Gavazzi as my supervisor.

In 2010 I was offered a PhD position at Leiden Observatory working with Prof. Marijn Franx and Prof. Pieter van Dokkum (Yale University) to study high-redshift galaxies with the novel spectroscopic data from the Wide Field Grism onboard Hubble Space Telescope. During my PhD I enjoyed numerous visits to Yale University, New Haven (Connecticut, US), and as a member of the 3D-HST collaboration I attended meetings of the consortium in New Haven, Leiden, Heidelberg, and Puerto Rico; I presented my work at conferences in Aix-en-Provence (France), Turku (Finland), Beijing (China) and Ameland (the Netherlands), and gave talks / colloquia at the Carnegie Observatories in Los Angeles, University of California at Santa Barbara, University of California at Irvine, Space Telescope Institute in Baltimore, and Goddard Space Flight Center in Greenbelt (Maryland). In 2012 I attended the Jerusalem Cosmology Winter School in Israel.

Besides my research work, during the years at the Sterrewacht I served as a teaching assistant to the Stellar Dynamics MSc Course taught by Prof. Vincent Icke, and I have participated in UNawe (Universe Awareness), an outreach program funded by UNESCO and the International Astronomy Union, as a coordinator for its Student Ambassador Program.

In January-March 2015 I took a hiatus from my research to join The Data Incubator, a highly selective training program in data science based in New York City, in preparation for a transition from academia to the data science world.

ACKNOWLEDGMENTS

It's a sign of mediocrity when you demonstrate gratitude with moderation.
(Roberto Benigni)

Writing a thesis is on one hand a solitary process, but such a long effort would not be possible without family, friends and colleagues, that more or less directly teach us lessons that contribute to the positive outcome of a PhD.

I was very lucky in going through this process at Leiden Observatory, which provided great support in every daily matter. Thanks to the administrative staff and the computer guys I could think 100% only about my research, without worrying about anything else. Thanks to Jeanne, Alexandra, Evelijn, Els, Debbie, Anita, Liesbeth, Eric, David, and Aart. A special word for Xander: without your support in the last year this work would have been completed in an even longer timescale - thanks for listening and advising, your help has been invaluable.

I feel privileged for having worked in a research group full of smart, inquisitive, and fun people. Shannon and Adam, I learned so much from you guys I don't even know where to start. You taught me about galaxies, life in academia and life in general. You listened when I needed scientific and personal help. Thanks guys, and keep the wolfpack alive! Jesse, you have been a great friend, and we shared laughs, frustrations, and adventures from China to Finland. Daniel, you inspired me a lot with your precision for details and with your career path. Moein, I immensely admired your calmness and your artistic skills. Allison, I am glad you brought back a necessary female touch to the group; thanks for all the laughs and for the more serious moments. I could have not chosen a better "academic little sister" - and I wish you the very best for the next years to come! Joanna and Simone, I wish we shared more time at the Sterrewacht, but I don't forget your voices, wise and sweet at the same time.

My thesis would have not been possible without the 3D-HST collaboration, and I owe scientifically a lot to many members, particularly Ivo, Iva, Gabe, Kate, and Ros.

Visits to New Haven, and 3D-HST meetings around the world, added to my PhD opportunities for discussing insightful science and developing friendships. Iva, you are a great inspiration for your enthusiasm in everything you do, and I am thankful to you and James for having always been incredibly welcoming in New Haven. Joel, conferences and 3D-HST meetings would have not been the same without you - I love recalling our roamings around Puerto Rico (credits to Micheal too), Israel and Jordan (+Renske and Monica), and China (+Rachel and Jesse). Rachel and Erica, it was always a great pleasure to see you in the Netherlands and in the US, and I hope there will be more chances in the future. Micheal, you are definitely one

of the coolest astronomers I know and I really enjoyed the time spent together in Heidelberg and in your soon-to-be new home Leiden. During my visits in New Haven I always found a warm room and a nice breakfast at David and Bob's - thanks to you guys for making me always feel at home.

At the Sterrewacht I was lucky to share an office with a bunch of incredible individuals that gave a pleasant atmosphere to my day-to-day life even in the hardest moments. First and foremost: Benjamin Darwin Oppenheimer, mostly known as benopp - Ben, thanks for making office 441 a very light place to be, for your friendship and the hilarity you can get out of every situation. Berenice, I am glad we spent all this journey together from the first to the last moment. Silvia, thanks for always being calm and available, and for your wisdom - thanks for translating my Samenvatting as well! Gabriela, thanks for your friendship, for all the laughs together, and for fostering my interest in Peruvian music.

During these years I shared lunches, coffee breaks, and borrels with many people that always provided topics for interesting and stimulating conversations: Renske, Rob, Nicola, Alessandra, Silvia, Gilles, Mason, Cameron, Aayush, Eva, Nico, Cristobal, Alex South, Alex North, Marijke, Sebastiaan, Steven, Caroline, Bram, Emanuele, Lorrie, Sylvia, Thanja, Marcello, Massimo and David. Thanks everybody!

In my early days at the Observatory I also felt very welcomed by the "old guard", Rafa, Sergio, Olivera, Jeanette, Stefania, Edith, Elisabetta, Ernst, Bernadetta, and Olmo. Thanks to all of you for providing an example for the years to come.

With some colleagues I found friendship that will last forever, even though we are increasingly more and more scattered around the world. Matteo and Irene, I remember like yesterday the day we celebrated our moving in together, and I could have not had better housemates to start this adventure here. Thanks for having bravely endured me as a housemate, and also for keeping the good time running afterwards. Marco, life at the Sterrewacht would have been very different without you. Thanks for the bike rides, the coffees, the chats about life and work, and for forcing me to go to the gym. Bernard, despite our fierce football rivalry we never argued a single time. You are such a cool guy I still cannot believe you support that team. Monica, thanks for your camaraderie, we shared a lot of our thoughts in these years and I always felt my feelings were in good hands when communicated to you. Andra, I wish you didn't travel that much during these years so we could spend more time together, but the memories of the time together are all great. Marissa, when I got here I didn't know you but you treated me like I knew you since forever. Thanks for being the center of so many activities, and for your sincere enthusiasm for everything around us. Tiff, I am so glad you are one of the first people I met here and we maintained our friendship through the years. You have been a great source of support, and your help with the graduation and visa processes has been invaluable.

I am thankful I could share artistic and athletic enterprises with some Sterrewacht people. With Andra (voice), Francisco (guitar), Simon (accordion) and Matteo (drums), I played the bass in The Redshift District, a rock-polka-punk band that deserved more gigs than the ones it had - thanks guys for that short but incredibly fun experience! A mention is deserved to the football crew that in the last 3 years

managed to achieve a decent success at the Sterrewacht tournament: Sebastiaan, Marco, Rob, Aayush, Clement, Allison, Francisco, Pedro, Bram, and Eric.

My friends outside the Sterrewacht also made Leiden such a special place to be. Thanks Hester, Simon, Lucia, for making Dutch class so fun. Thanks to Raphaela, Nick, Anna, Bart, Niels, Sonja, Mart, Mark, Ugo, Ursula, Kristin, Sandro, and Gleb for the dinners and festivities around town. Thanks Fabrizio for being my football buddy, and thanks Agnese for being so patient with this small religion of ours. Sara, even though we attended the same University in Italy we only met here and I am really glad we did, because your joy is contagious and your accent reminds me of home like nobody else. Tom and Alex West, our knowledge started as “boyfriend of”, but I am happy I got to know you better through the years.

During these years away from home, I didn’t lose touch with the best friends from my university years, sharing our post-university adventures, and providing always good (g)chats. Franz, thanks for being at the same time so inspirational and so much fun. Vedo, thanks for keeping me in the loop with your always interesting projects, and thanks for the consulting on the design of the cover. Dani, you have been my long-standing housemate, thanks for being one of my best contacts in our valley. Giulio, the synthesis of our friendship stands in the 7621 km we travelled together through Asia without killing each other, and instead integrating our strengths for the best possible outcome.

Thanks to my parents, Vera and Maurizio, for their unconditional support during these years. Having a single child that moves abroad is not easy for anybody, but you have been always encouraging and understanding of my choices.

The greatest “thank you” has to go to my better half, my partner in crime, my voice of reason, my biggest source of joy, my greatest support through these years. Annie, you participated in this journey more than anybody else. I cannot state how immensely thankful I am for all the times you calmed me down, listened to me, and cheered me up. This thesis is yours too. I always felt that the Alps and the Rockies forged us akin, and after we met in the flattest place on Earth we have walked so much side by side that I just cannot wait for our next step in life together.